Properties and Characterisation of Sputtered ZnO

by

Leo P Schuler
ME

A Thesis
presented for the degree of
Doctor of Philosophy
in
Electrical and Computer Engineering
at the
University of Canterbury
Christchurch, New Zealand

Christchurch, New Zealand

Abstract

The aim of this work was the study of sputtered zinc oxide (ZnO) film deposition, the optimisation and characterisation of film properties and applications as a sensing material.

In recent years there has been increased interest in ZnO in terms of its potential applications as piezoelectric films (or coatings) for surface acoustic wave devices (SAW) [1], for IR and visible light emitting devices and UV sensing. The electrical, optoelectronic and photochemical properties of undoped ZnO have resulted in its use for solar cells [2], transparent electrodes and blue/UV light emitting devices [3]. ZnO is a unique material that exhibits both semiconducting and piezoelectric properties. In the past decade, numerous studies have been made on both production and application of one-dimensional ZnO. Compared with other semiconductor materials, ZnO has a higher exciton binding energy of 60 meV, which gives it a high potential for room temperature light emission, is more resistant to radiation, and is multifunctional as it has piezoelectric, ferroelectric, and ferromagnetic properties [4]. ZnO-based semiconductor and nanowire devices are also promising for the integration on a single chip. So far, the various applications of ZnO nanomaterials such as biosensors [5], UV detectors [6] and field emission displays are being developed.

In this work, ZnO was sputtered using both DC and RF magnetron sputtering. Reactive DC sputtering was performed with a Zn target and oxygen plasma, while RF sputtering was performed with a ZnO target. Comparisons between films deposited under different conditions on different substrates were employed to assess film properties. Several experiments were performed on as-grown films as a control for subsequence treatments, other samples were post-annealed in N_2 at temperatures up to 1200 ºC, the highest reported annealing temperature and the quality of the deposited films was determined using PL, RBS, XRD, SEM and AFM. The piezoelectric properties (d_{33}) of selected films were determined using single beam interferometry, double beam interferometry, and for the first time, using piezoelectric force microscopy (PFM).

It was found that DC sputtered films yielded better quality films as evident by PL and XRD analysis and higher piezoelectric response than RF sputtered films.

Films deposited using DC sputtering on Si substrates and followed by post-annealing in N_2 atmosphere at 1100 ºC showed the highest recorded PL response, while films deposited on sapphire showed good PL response without any need for post-annealing.

The d_{33} of selected films were determined first using single beam interferometry and inflated results were reported, caused by sample bending/buckling. Double beam interferometry results confirmed d_{33} values in the range of 3.3 to 4.3 pm/V. Piezoelectric force microscopy (PFM) which is based on AFM, was employed to investigate the local electromechanical (piezoelectric) properties of the ZnO films.

UV sensing was demonstrated using Schottky contacts and SAW devices on ZnO deposited on Si and post-annealed. In the first instance, Schottky contacts were fabricated on the films and the I-V characteristics determined under exposure of various light sources. The current increased up to one order of magnitude during exposure with a halogen light bulb, which is known to emit energy in the UV band. Another experiment was performed using surface acoustic wave (SAW) devices which were fabricated on the films and interrogated using a network analyser. These SAW devices contain an interdigitated transducer and two reflectors each. The signals sent back from the two reflectors were analysed under various light conditions and gave lower readings during exposure to UV light.

In order to enable device fabrication of UV sensors a novel "super coating", achieving both optimised PL and d_{33} properties, was designed, fabricated and tested. The structure is based on optically transparent Quartz substrate. During this experiment the first DC sputtered coat was optimised to have high PL response by post-annealing at 900 ºC. Afterwards, the second coat was left as-sputtered in order to have highly piezoelectric properties. Preliminary analysis using XRD showed two peaks corresponding to the annealed and not annealed coat, which suggest the super coating combines the properties of the two individual films. This configuration has the potential to be used as UV sensing material and as piezoelectric substrate for SAW devices.

Hall of Fame

This chapter is about you -

You, who helped me in some major way or another through the course of this work:

Maan Alkaisi, who was my mentor and supervisor

Richard Blaikie, my second mentor and guide

and Steve Durbin, who helped me along the way.

Helen Devereux and Gary Turner to keep me on track in the lab,

Pieter Kikstra, Philipp Hof and crowd who helped to keep the computers running.

Across the University, Stephen Brown for XRD, Neil Andrews and Mike Flaws for SEM's, Rob McGregor for glass work and Peter Harland for listening to my troubles. And of course all of you co-students who supported my quest in some way. It was a pleasure to join forces with ZnO investigators across New Zealand: Paul Miller, Roger Reeves, Martin Allen at University of Canterbury, as well as Andreas Markwitz, and John Kennedy, to name a few.

And all of you keen tourists who asked me to fly out, to explore this beautiful country – a break from the studies was much appreciated!

You, from overseas, without your help and input I would still be completely lost. You all helped me to gain important thoughts and to perform important experiments.
At EPFL, Lausanne, Paul Muralt, Fabrice Martin and Nava Setter gave me insight into the perfect sputtering of ZnO and helped to measure the magic "d_{33}".
At Macquarie University, Sydney, Ian Guy, who gave up his retirement temporarily and Scott Butcher helped measure piezoelectric properties of ZnO.
Yicheng Lu at Rutgers University, who showed me around and for more tricks in ZnO.
Len Brillson at Ohio State University for more on ZnO and of course the networking.
Nagarayan Valanoor, at UNSW who helped to measure the elusive d_{33}.

- Thank you!

I have been a small part of the MacDiarmid Institute since its inception in 2002 and thanks to its financial support I am here now. In my opinion, the Institute enables to focus on research and collaboration between Universities and Institutes, with the aim of collaboration rather than competition. This brought along tremendous improvements in regards to much needed resources.

Finally, I am eternally grateful for the unerring support from my beautiful wife Helen and the distractions from my two kids, Sarah and Chris. For encouragement, patience, inspiration, motivation, and above all for the laughter, I cannot thank you enough.

"Nothing great ever happened in this world without exaggerated hope."
(Jules Verne)

Table of Contents

List of figures

List of tables

Acronyms and abbreviations

AFM	Atomic force microscope
ARPES	Angle-resolved photoelectron spectroscopy
ASA	Atomic sphere approximation
CMOS	Complementary metal–oxide–semiconductor
C-V	Capacitance-voltage characteristics. The capacitance of a junction at varied input voltage is determined.
CW	Continuous wave
d_{33}	Principal performance-determining parameter for piezoelectric materials. Indicates charge per unit force in the polarisation direction of the sample; the electric field and the strain are both along the polarisation axis.
d_{31}	Indicates charge per unit force in the polarisation direction of the sample, but the deflection of interest is that orthogonal to the polarisation axis; the electric field and the strain are orthogonal to each other.
DC	Direct current
Dektak	Surface profilometer
DFT	Discrete Fourier transformation
DOS	Density of states
EBE	Electron beam evaporation
EBL	Electron beam lithography
Electrostriction	Property of all electrical non-conductors, or dielectrics that manifests itself as a relatively slight change of shape, or mechanical deformation, under the application of an electric field.
FSG	Fused silica glass, also clear fused quartz (SiO_2)
FWHM	Full width at half maximum
HMW	High-molecular-weight

IC	Integrated Circuit
IDT	Interdigital transducer
IPA	Isopropyl alcohol
IR	Infrared
I-V	Current-voltage characteristics. A known voltage is applied at the probe to be measured and the resulting current is recorded.
LMS	Least-Mean-Square
LMTO	Linear-muffin-tin-orbital method
MIBK	Methyl isobutyl ketone
NOM	Near-field optical microscope
OPC	Optical proximity correction
PDF	Powder diffraction file analysis (in conjunction with XRD analysis)
PES	Photoelectron spectroscopy
PFM	Piezoelectric force microscopy
PGMEA	Propylene glycol monomethyl ether acetate
Piezoelectric effect	An observed phenomenon (the generation of surface charges in response to applied stress) in some crystals.
Piezoelectrics	Materials showing a piezoelectric effect (= piezoelectricity).
PL	Photoluminescence
PML	Perfectly matched layer
PMMA	Poly(methyl methacrylate)
RBS	Rutherford backscattering
RCA	The RCA clean is the industry standard for removing contaminants from wafers. Developed at the RCA (Radio Corporation of America) - hence the name.
RF	Radio-frequency
RIE	Reactive ion etch (dry etch)

rms	Root-mean-square
RT	Room temperature
SAW	Surface acoustic wave
SE	Secondary electron
SEM	Scanning electron microscope
SP	Surface plasmon
TCO	Transparent and conductive oxide layer
UV	Ultra-violet
VOC	Volatile organic compound
XRD	X-ray diffraction
ZnO	Zinc Oxide
∅	Diameter
≈	Approximate

Chapter 1
Introduction

The last 60 years or so have been shaped by the silicon age. The expression “information age” is a misnomer really, as it would not have materialised without silicon and other semiconducting materials.

The first transistor device, or crystal triode, was invented in the Bell labs in 1947 by John Bardeen, Walter Brattain and William Shockley. Unbeknown to many, it was built using Germanium, a semiconductor.

The semiconductor industry is still a main driver of today’s innovations. A life without semiconductors is unimaginable today: no information highway, no cell phones, no airbags in cars and no personal computers, to name a few. Besides silicon, which has been THE semiconductor for the last 60 years, scientists have turned their efforts towards other materials to fulfil the needs of various niche applications.

It is a little known fact that the semiconducting properties of Zinc Oxide (ZnO) were already discovered in the 1920’s. Then, ZnO crystals were used as diodes to rectify AM radio signals.

Varistors (voltage dependent resistors) are commonly made by sintering of ZnO powder with added trace materials. This method was first reported in the 1950ies [7, 8].

In recent years there has been increased interest in ZnO in terms of potential applications as piezoelectric films (or coatings) for surface acoustic wave devices (SAW) [1], for IR and visible light emitting devices and UV sensing [9], which was reported in 1986. The electrical, optoelectronic and photochemical properties of undoped ZnO have resulted in its use for solar cells [2], transparent electrodes and blue/UV light emitting devices [3]. ZnO is a unique material that exhibits both semiconducting and piezoelectric properties. In the past decade, numerous studies have been made on both production and application of one-dimensional ZnO.

ZnO nanomaterials are promising candidates for nanoelectronic and photonics. Compared with other semiconductor materials, ZnO has a high exciton binding energy of 60 meV, which gives it a high potential for room temperature light emission. It is more resistant to radiation and is multifunctional as it has piezoelectric, ferroelectric and ferromagnetic

properties [4]. ZnO-based semiconductor and nanowire devices are also promising for integration on a single chip. So far, the various applications of ZnO nanomaterials such as biosensors [5], UV detectors [6] and field emission displays are being developed.

ZnO can be deposited on a substrate using various methods, such as sputtering, pulsed laser deposition (PLD), molecular beam epitaxy (MBE), chemical vapour deposition (CVD), metal organic CVD (MOCVD) and sol-gel. During these studies, we have been producing ZnO films using sputtering, as this technique offers relatively fast deposition rates at reasonable cost.

The exploitation of ZnO-related materials in electronic and photonic applications is impeded by the difficulty of p-type doping [10]. N-type conductivity is easily established via excess Zn or with Al, Ga, or In doping. However, ZnO displays significant resistance to p-type doping. Difficulty in achieving bipolar (n- and p-type) doping in a wide bandgap material is not unusual. ZnSe and GaN can be easily doped n-type, while p-type doping is difficult. During my time at University of Canterbury working on my ME Thesis we recognised the need to fabricate piezoelectric coats on irregular samples. Piezoelectric wafers (for example quartz or lithium niobate) can be obtained off the shelf. However, there was no way of attaching a coat of piezoelectric material on irregularly shaped samples. This hurdle lead to the idea of sputtering ZnO on these samples. The first samples were sputter-coated overseas and limited trials were performed. Just before I submitted my ME Thesis, our department received a brand-new sputtering system, capable of DC and RF sputtering. Preliminary sputtering experiments were performed. More questions than answers remained. How can d_{33} be maximised? How can PL be maximised? How do the two properties interact? How can these properties be optimised; individually and in combination? - In short, enough work to start on another Thesis!

The remainder of this Thesis is structured as follows:

In Chapter 2 the history and background of research in the ZnO area is given as well as information about the crystal structure, lattice parameters, the electronic band structure and piezoelectricity. Chapter 3 gives an introduction of the important experimental techniques used during this research, while Chapter 4 lists the characterisation methods. The next two chapters document in detail the ZnO film deposition, in Chapter 5 and the outcome of post-sputtering treatments in Chapter 6, respectively. In Chapter 6 we report

for the first time the outcome of annealing and dry etching of ZnO sputtered on various base substrates in the temperature range of up to 1200 ºC. The determination of piezoelectric properties in these films is documented in Chapter 7. In this chapter we describe for the first time the determination of the d_{33} distribution down to the nanometer scale, which is made possible by Piezoelectric Force Microscopy (PFM). Finally Chapter 8 is about the fabrication of device structures, where we report the fabrication of a novel super coating and Chapter 9 details the conclusions and suggestions for further work.

Publications in refereed journals

Schuler, L. P., Valanoor, N., Miller, P., Guy, I., Reeves, R. J., & Alkaisi, M. M. (2007). The Effect of Substrate Material and Postannealing on the Photoluminescence and Piezo Properties of DC-Sputtered ZnO. Journal of Electronic Materials (2007), 36(4): p. 507-518.

Schuler, L. P., Alkaisi, M. M., Miller, P., & Reeves, R. J. (2006). UV sensing using surface acoustic wave device on DC sputtered ZnO monolayer. Microelectronic Engineering, 83(4-9), 1403-1406.

Schuler, L. P., Alkaisi, M. M., Miller, P., Reeves, R. J., & Markwitz, A. (2005). Comparison of DC and RF sputtered zinc oxide films with post-annealing and dry etching and effect on crystal composition. Japanese Journal of Applied Physics, Part 1: Regular Papers and Short Notes and Review Papers, 44(10), 7555-7560.

Chapter 2
History/Background

Zinc Oxide was known for a long time, since it was a by-product of copper smelting. The copper age commenced around 4500 B.C. In that process the zinc proportion of copper ores was reduced to zinc vapour which oxidised and deposited in the furnace flues as an impure powder known as "cadmina". Through experiments our ancestors developed a process for successfully smelting it with copper and thus made the first copper-zinc alloy: brass. Later, zinc ore replaced zinc oxide for this purpose, but the cementation continued as the only method of making brass until the seventeenth century.

To make zinc oxide suitable for medical and other purposes, a special process was devised and a furnace designed for purifying cadmina. Eventually, the oxide would adhere to the walls and roof, increasing in size, until it appeared like skeins of wool. It was called "philosopher's wool" and used as ointment. Marco Polo also reported many years later that the Persians used a similar process.

Our ancestors were unaware of the true components of ZnO. Zn was only recognised as an element by Paracelsus in 1520 and O_2 was only formally discovered in 1774 by Priestley. The Chinese however used ZnO commercially for several centuries before that. The modern history of ZnO started around the middle of the 18^{th} century. Cramer, a German scientist, discovered that it could be made by burning metallic Zn in air. The manufacture of ZnO started in France about 1840. In 1871 ZnO was used in the paint trade due to its whiteness, fine texture and opacity. ZnO in sufficient quantities helped to hasten the development of rubber and ceramic goods as well as the paint industry.

Soon after the first radio broadcasting stations started transmitting in the 1920's, ZnO crystals came into popular demand for their semiconductor properties. Using an antenna and a fine copper whisker (cat's whisker) the RF signal was rectified at the junction of the wire and the crystal.

Unknown to many, ZnO has been intensively studied since 1935 and the theory of semiconductors got a firm start. Wagner, Schottky and co-workers in Germany proposed that the semiconductor properties of ZnO were dependent upon imperfections in the crystal structure. They validated their theoretical speculations with conclusive experimental data. A detailed list of publications (many in German) is contained in [11].

With suitable heat treatment the electrical conductivity could be increased by orders of magnitude. Heating ZnO in air for two hours at 900 °C produced moderate improved conductivity, but heating for a few minutes in a reducing atmosphere led to a marked increase in conductivity. Wagner proposed that heat treatment and reducing atmospheres introduced semiconductor properties by formation of interstitial zinc atoms. Research in ZnO intensified in the 1950's and peaked in the 1970's, then faded. It was not possible to p-type dope ZnO, so the interest moved to other structures in the III-V system, such as GaN and GaAs.

However, the advent of modern analysis tools such as atomic force microscopy (AFM) and laser interferometric analysis enabled more in-depth analysis of ZnO. Combined with the possibility to grow epitaxial layers, quantum wells and nano-rods, this led to a renewed interest in the 1990's. The ultimate goal for now is still p-type doping, which has not been fully achieved and remains controversial.

In summary, much of our current industries and daily life is critically reliant upon this compound.

2.1 Crystal structure and lattice parameters

Most of the group II-VI binary compound semiconductors crystallise in either cubic zinc-blende or hexagonal wurtzite structure. Each anion is surrounded by four cations at the corners of a tetrahedron and vice versa. This tetrahedral coordination is typical of sp^3 covalent bonding, additionally these materials also have a substantial ionic character.

ZnO, consisting of the anion (O^{2-}) and cation (Zn^{2+}) is a II-VI compound semiconductor whose ionicity resides at the borderline between covalent and ionic semiconductor. The crystal structures shared by ZnO are wurtzite (B4), zinc blende (B3) and rocksalt (B1), as schematically shown in Figure 1. At ambient conditions, the thermodynamically stable phase is wurtzite. The zinc-blende ZnO structure can be stabilised only by growth on cubic substrates and the rocksalt (NaCl) structure may be obtained at relatively high pressures.

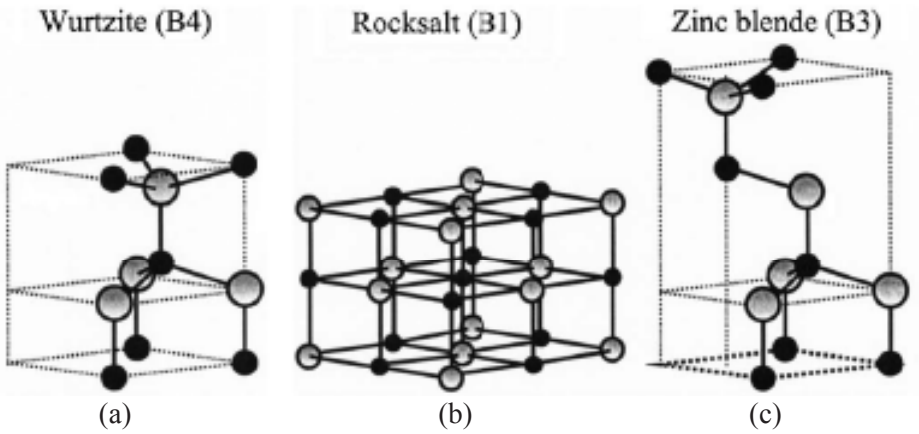

Figure 1: Stick and ball representation of ZnO crystal structures. (a) hexagonal wurtzite (B4), (b) cubic rocksalt (B1) and (c) cubic zinc blende (B3).

In the wurtzite orientation, the tetrahedral coordination enables polar symmetry along the hexagonal axis. This polarity is responsible for a number of the properties of ZnO, including piezoelectricity and spontaneous polarisation and is a key factor in crystal growth, etching, doping and defect generation. The four most common surface terminations of wurtzite ZnO are the Zn-polar face (0001) and O-polar $(000\bar{1})$ face (c-axis oriented), as well as the non-polar $(11\bar{2}0)$ (a-axis) and $(10\bar{1}0)$ (m-plane) faces which both contain an equal number of Zn and O atoms. The polar faces possess different chemical and physical properties and the O-polar face possesses a slightly different electronic structure to the other three faces [12]. Also, the polar surfaces and the (1010) surface are stable, whereas the $(11\bar{2}0)$ face is less stable and generally has higher surface roughness than its counterparts. The (0001) plane is also basal. Recent research in our laboratory has been performed to determine the polarity effects of bulk ZnO. Results have been reported in [13, 14].

The lattice parameters of the hexagonal unit cell determined by various methods [15] range from 0.32475 … 032501 nm for the *a* parameter and from 0.52042 … 0.52075 nm for the *c* parameter (at room temperature). Commonly accepted "constants" are a=0.32495 nm and c=0.52069 nm. The density is 5.605 g cm^{-3}.

The ideal wurtzite structure has a hexagonal unit cell with two lattice parameters, *a* and *c*, in the ratio of $\frac{c}{a} = \sqrt{\frac{8}{3}} \approx 1.633$ and belongs to the space group of C_{6v}^4 or $P6_3mc$. A schematic representation of the wurtzitic ZnO structure is shown in Figure 2. The structure

is composed of two interpenetrating hexagonal-close-packed sub lattices, each of which consists of one type of atom displaced with respect to each other along the threefold *c*-axis by the amount of $\frac{3}{8}$ in fractional coordinates. Each sub lattice includes four atoms per unit cell and every atom of one kind (group-II atom) is surrounded by four atoms of the other kind (group VI), or vice versa, which are coordinated at the edges of a tetrahedron.

In a real ZnO crystal the wurtzite structure deviates from the ideal arrangement by changing the $\frac{c}{a}$ ratio, also called "*u*" value.

The *u* parameter is defined as the length of the bond parallel to the *c* axis, in units of *c*.

However, a strong correlation exists between the $\frac{c}{a}$ ratio and the *u* parameter: When the $\frac{c}{a}$ ratio decreases, the *u* parameter increases in such a way that those four tetrahedral distances remain nearly constant through a distortion of tetrahedral angles due to long-range polar interactions.

Experimentally, for wurtzite ZnO, the real values of *u* and $\frac{c}{a}$ were determined in the range *u*= 0.3817 … 0.3856 and $\frac{c}{a}$ = 1.593 … 1.6035 [15].

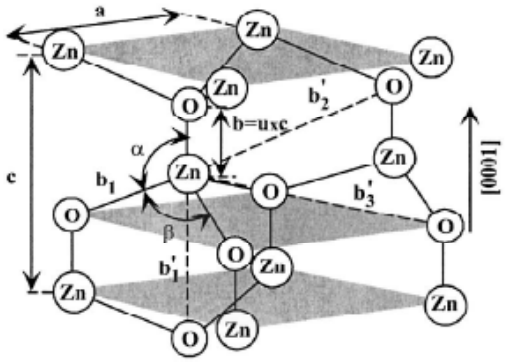

Figure 2: Wurtzitic ZnO structure with lattice constants a in basal plane and c in the basal direction. u parameter is expressed as the bond length or the nearest-neighbour distance b divided by c (0.375 in ideal crystal) and α and β (109.47° in ideal crystal) are the bond angles.

2.1.1 Electronic band structure

It is crucial to gain an accurate knowledge of the band structure of ZnO as this is the key for its potential utility in device applications. Several theoretical approaches with varying complexity have been employed to calculate the band structure and a number of experimental results of data on the band structure of the electronic states of wurtzite ZnO have been published. X-ray- or UV reflection/absorption or emission techniques have conventionally been used to measure the electronic core levels in solids. These methods measure the energy difference by inducing transitions between electronic levels or by exciting collective modes. Another important method for the investigation of the energy region is based on the photoelectric effect extended to the x-ray region, namely photoelectron spectroscopy (PES). The peaks in emission spectrum correspond to electron emission from a core level without inelastic scattering, which is usually accompanied by a much less intense tail region in the spectrum.

More recently the angle-resolved photoelectron spectroscopy (ARPES) technique has been introduced. This technique together with synchrotron radiation excitation has been recognised as a powerful tool that enables experimental bulk and surface electronic band-structure determinations under the assumptions of k conservation and single nearly-free-electron-like final band.

The band-structure of ZnO was first theoretically determined in 1969 using Green's function [16]. Several experimental works performed on wurtzite ZnO followed, using x-ray-induced photoemission spectroscopy [17] and UV photoemission measurements [18, 19]. However, the various results did not correspond well.

The advent of computers helped to improve numerical predictions. The effect of the Zn 3*d* levels was taken in account in the calculations as valence-band states. This allows an estimation of the position of the Zn *3d* states and also takes into account their non-negligible influence on the *s*- and *p*- derived valence bands [20].

In one of the latest and most elaborate works [21] the band structure was calculated using the linear-muffin-tin-orbital method (LMTO) in the atomic sphere approximation (ASA). The basis sets of s, p and d orbitals were used for both the cation and the anion for all components. Empty spheres were introduced in all cases in order to keep the overlap of atomic spheres within 16%.

The band structure is shown along high symmetry lines in the hexagonal Brillouin zone. The valence band maxima and the lowest conduction band minima occur both at the Γ point k=0 which indicates that ZnO is a direct band gap semiconductor. In Figure 3 (a) the electronic structure of ZnO in the wurtzite structure is shown. From calculations a direct band gap value of (0.067 Ryd) 0.91 eV [at 0 K] was determined. The equilibrium lattice parameter values were determined as a=0.3227 nm and c=0.5189 nm which is in good agreement with other reported values. Figure 3 (b) shows the corresponding density of states. Most electrons are located close to the valence band edge. The results suggest that the major portions of valence and conduction bands are essentially formed out of sp^3d^5 of Zinc and p^3 of oxygen, providing a rational basis for constructing a realistic tight binding (TB) model. Atomic orbital contributions to the overall electronic structure can also be understood by analysing surface density of states (DOS), which is again shown in Figure 3 (b). The upper panel of DOS contributions comes from Zinc s, p and d orbitals, while the lower panel shows those from oxygen s and p orbitals. However, these states have a substantial admixture from the Zn p and d states.

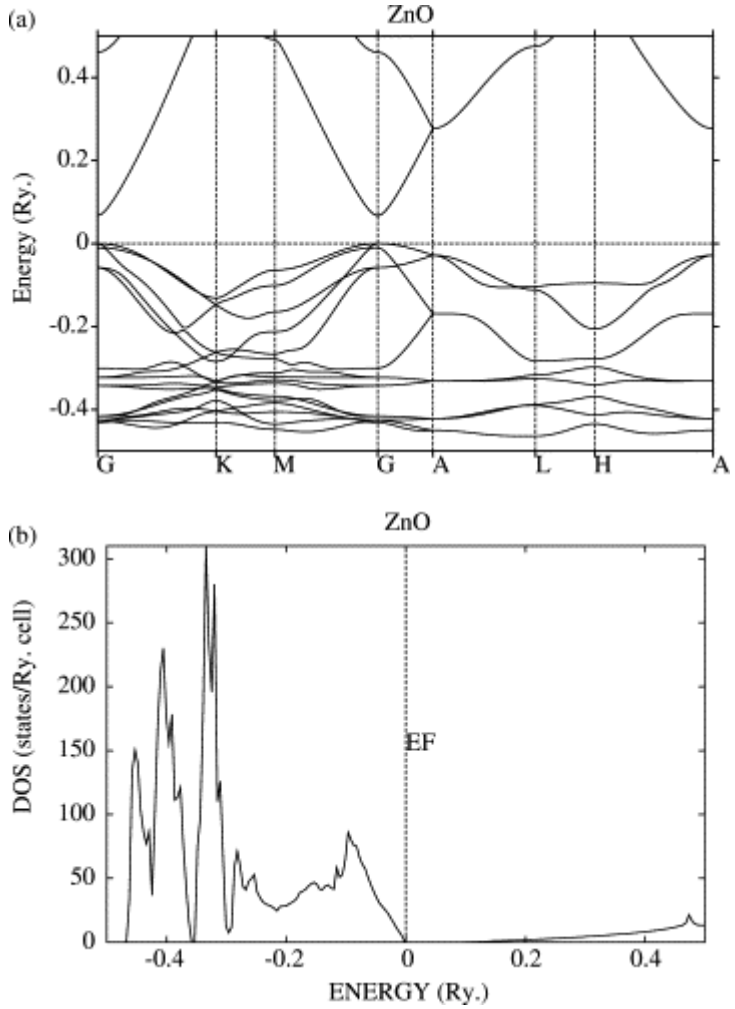

Figure 3: (a) Electronic band structure of ZnO in wurtzite structure. (b) Density of states of ZnO in wurtzite structure (from [21]).

2.1.2 Piezoelectricity and ferroelectricity

All materials undergo a change in dimension when they are exposed to an electric field. This phenomenon is called electrostriction, the induced strain is proportional to the square of the electric field. While generally considered to be an exclusive property of crystalline dielectrics, the phenomenon is also observed in amorphous solids and liquids. However, the reverse effect does not occur in all materials, i.e. most do not develop an electric polarisation when they are strained by an external stress. The materials that do not exhibit the reverse effect belong to the 11 crystal classes that possess a centre of symmetry. The materials belonging to the remaining 21 point groups have a non centro-symmetric structure and exhibit the reverse effect, except the materials from the cubic class (432) which possesses symmetry characteristics which combine to give no reverse effect. The materials that show the reverse effect are piezoelectric. To a first approximation the

polarisation is proportional to the stress and the effect is direct. Piezoelectric materials also show the so-called converse effect, as the development of a strain is proportional to the applied field. The converse effect is superimposed to the electrostrictive effect.

Among the 20 piezoelectric crystal classes, a subdivision can be made between the 10 classes which contain a unique polar axis in the unstrained conditions and the 10 classes that have no such polar axis. Quartz is an example of a piezoelectric material without a polar axis in the unstrained state. In that case the dipolar arrangement occurs in several compensating directions so that there is no net crystal dipole. When stress is applied, the symmetry is disturbed and a direction is favoured, giving rise to a net polarisation and to the piezoelectric effect. The piezoelectric materials which possess a polar axis in the unstrained conditions are called pyroelectric. When pyroelectric materials are heated, they expand and the magnitude of the net dipole changes with the temperature, so that compensating charges appear on the two opposite faces of the crystal. ZnO is a pyroelectric material. Pyroelectric materials can be subdivided again in two classes. The ferroelectric materials are defined as those pyroelectric materials for which the polar axis can be realigned in another direction by an external electric field.

ZnO clearly has piezoelectric properties and is subject to electrostriction. It appears that electrostriction in ZnO has not been investigated in detail as a literature search showed no related publications. Figure 4 shows the stimulus-strain relationship of piezoelectric materials.

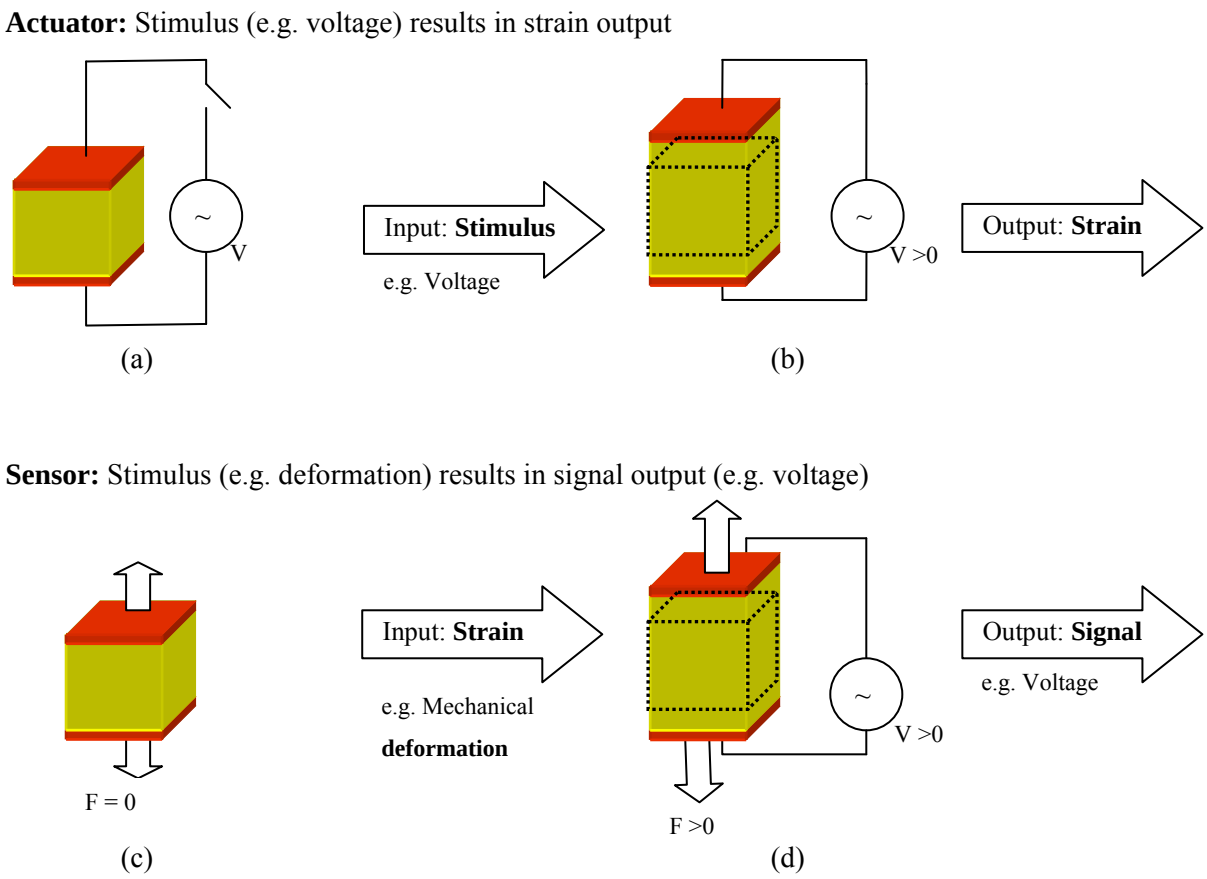

Figure 4: Stimulus-strain relationship for piezoelectric substrate.

Figure 4 illustrates the relationship between stimulus and strain. It is valid for both stationary and slowly changing events (i.e. piezoelectric actuator or sensor) and dynamic events (i.e. SAW device excited by an RF signal). A piezoelectric element working as actuator in its unexcited state is shown in (a). Applying a voltage will lead to a deformation as shown in (b). The same piezoelectric element working as a sensor in its unexcited state is shown in (c). Applying a strain will lead to a deformation and a voltage to be generated as shown in (d).

2.1.3 Further reading

- Zinc oxide rediscovered, 1957 [22]
- Surface barriers on zinc oxide, 1970 [23]
- The calculated defect structure of ZnO, 1980 [24]
- Ultraviolet detectors in thin sputtered ZnO films [9]

- Preferred orientation and piezoelectricity in sputtered ZnO films, 1998 [25]
- Recent advances in processing of ZnO, 2004 [1]
- Bound exciton and donor-acceptor pair recombinations in ZnO, 2004 [26]
- ZnO rediscovered -- once again!? Superlattices and Microstructures, 2005 [27]
- Recent progress in processing and properties of ZnO, 2005 [10]
- Zinc oxide bulk, thin films and nanostructures, 2006 [28]

Chapter 3
Experimental techniques

3.1 Substrate preparation

For this work various substrates were used, dependent on the anticipated use of the films. Low-cost microscope slips and monitor-grade Si wafers were used for general trial runs. Mainly Si wafers of various crystal orientation and resistivity grades were used as base substrate for good quality films. To investigate the influence on the crystal quality of the sputtered ZnO films quartz, fused silica glass (FSG) and sapphire wafers were used as base substrate as well.

Depending on the purity/cleanliness of the substrates, minimal cleansing or a full cleaning regime had to be employed to prepare them for sputtering. Table 1 shows details of the substrates used for this research and their preparation.

	Microscope cover slips (Borosilicate glass)	Si wafers	Quartz (SiO_2)	FSG (SiO_2)	Sapphire (Al_2O_3)
Size	22 x 22 mm 24 x 60 mm	∅ 75 mm, 100 mm	10 x 10 mm individually wrapped	∅ 50 mm individually wrapped	∅ 75 mm
Cleaning	Solvent cleaning	RCA /Solvent cleaning	Not necessary	Not necessary	Solvent cleaning

Table 1: Overview of substrates / preparation.

Throughout all processing steps great care was taken to ensure the cleanliness of sample surfaces, as dirt and dust on the substrate prevent the deposited material from sufficiently bonding to the surface. Or if dust is present during lithographic steps, it can alter the design, as it can lead to shorting out of contacts or the interruption of conductors.

The biggest cause of dirt and dust were dirty substrates and contamination through the environment. Common procedures for cleaning silicon wafers include an RCA clean, H_2O_2-NH_4OH-H_2O for removing organic residue and solvent cleaning with acetone, methanol and IPA to remove remaining contaminates. RCA was occasionally used for unclean wafers. The RCA cleaning procedure is listed in Appendix B.

Generally solvent cleaning was used in conjunction with an ultra-sonic bath to provide the basis for cleaning. Sometimes the substrates would not become completely free of contamination, so cotton swabs were used to remove the final elements of unwanted dirt. Obviously it was easiest to use prime wafers as they were mostly in a very clean state.

Finally, the samples were closely inspected for any residues and the process repeated if any contamination remained.

Depending on further use, the substrates were cleaved after the deposition. For PL analysis small samples sizes (2 x 3 mm) were required.

3.2 Sputtering: Theory and setup

Sputtering is a well established process [29-31] and can be easily scaled up. The thickness of the coatings can range from nanometres to micrometers and the area is scalable up to sample size of metres (i.e. for coating of architectural glass).

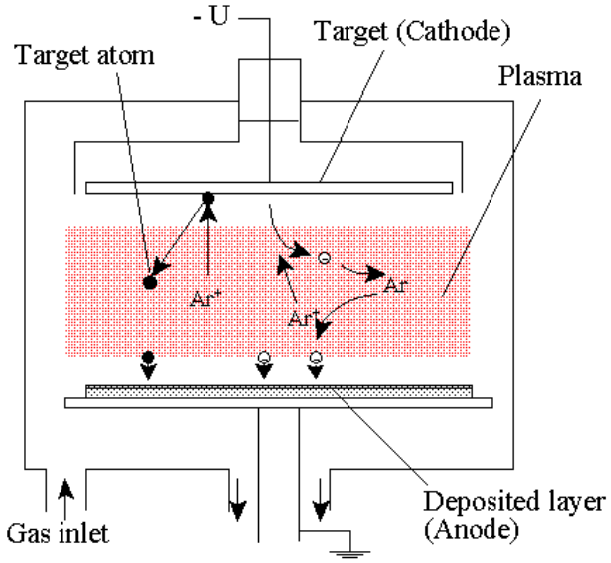

Figure 5: Schematic diagram of the sputtering chamber.

As shown in Figure 5 the sputter target of the material to be sputtered is the cathode of the system and the substrate/substrate holder the anode, which is grounded.

Once the vacuum chamber is evacuated to the desired level, a sputtering gas (usually Argon) is introduced. The background pressure is normally in the Pa range. Reactive

sputtering is achieved by adding O_2 to form oxides, H_2 to form hydrogenated material, or N_2 to form nitrides. The stoichiometry of the sputtered film can be set by varying the ratio of the introduced gases. A large negative potential between target and ground initiates the process and electrons will be emitted from the target surface. Typical voltage ranges from 100 Volts to 1 kV. The ejected electrons are accelerated through the potential and get a very high kinetic energy. They collide with the gas molecules and ionise them. The positive ions are accelerated towards the cathode. On hitting the target surface, part of the energy is transformed into heat and part is transferred to other particles. These particles can eventually get enough energy to leave the target surface. Various particles are eventually emitted: neutral atoms which will eventually reach the substrate and build the film, negative ions, photons and secondary electrons. The secondary electrons will again be accelerated from the target and ionise more gas atoms that will sputter the target and so on. The secondary electron yield needs to be high enough in order to maintain the plasma.

When the substrate is immersed into the plasma (shutter removed), the electrons cover the surface much faster than the ions. A negative potential develops which attracts the ions and repels the electrons. Around the substrate an electron depleted sheet forms up to a steady state when the ionic current equals to the electron current. The target has always the strongest negative potential.

The bombardment is a key parameter in the sputtering deposition. It has at least three major effects. Firstly, it heats the substrate. The temperature of a substrate immersed in plasma will rise up to 150 ºC [32, 33]. This thermal energy enhances the surface mobility of the atoms and has an influence on the growth of the film. Secondly, the energy of a bombarding particle can be directly transferred to an atom of the surface through momentum transfer in a collision. It will also increase its mobility, which can lead to resputtering of the atom from the surface [34]. Thirdly, if the energy of the bombarding particle is too high, it can damage the film by the creation of defects during its implantation in the film. The bombardment is also influenced by the nature and pressure of the sputtering gas, the sputtering distance and the sputtering angle.

Today most commercial sputtering systems use planar magnetron targets. This technology uses powerful magnets to confine the “glow discharge” plasma to the region closest to the target plate. That vastly improves the deposition rate by maintaining a higher density of ions, which makes the electron/gas molecule collision process much more efficient. Our

system, as described below, is optimised for research rather than throughput and achieves a sputtering rate of only around 10 nm per minute for insulating ZnO.

For more information about sputtering please refer to [29-31, 35, 36].

3.2.1 Sputtering set-up

The BOC Edwards Auto 500 is a versatile, front-loading thin film system for research & development or pre-production. The box chamber allows it to perform a combination of evaporation, electron beam and sputtering applications on large-diameter substrates, without breaking the vacuum. For this research mainly DC sputtering was used; for comparisons a selected number of sputtering runs were performed using RF sputtering. Both sputtering targets have a diameter of 75 mm. The targets have a typical thickness of 3 or 6 mm.

In Figure 6 an overview of the sputtering system is shown in (a) and a view of the components in the vacuum chamber in (b).

The system contains:

① Electron beam evaporation source with four selectable crucibles and shutter
② DC sputtering target and shutter
③ RF sputtering target and shutter
④ Mass flow control panel for two gases
⑤ Substrate heater
⑥ Rotary work holder
⑦ Crystal thickness monitor

(a) (b)

Figure 6: Overview of BOC Edwards Auto 500 sputtering system.

3.3 Annealing furnace

The furnace used for this research boasts three individual quartz tubes that can be used simultaneously for different tasks. The tubes can be heated up to 1200 °C. Additionally the atmosphere inside can be altered as desired; in our case N_2 was introduced. To achieve good temperature uniformity within the centre zone and over a wide temperature range, each tube has three separate heating zones along its length, with independent PID controllers. The two end zones compensate for end heat losses. No temperature ramping can be programmed. Figure 7 shows the access lid on one furnace tube. A boat, consisting of a section of quartz tubing attached to sliders, was used to carry the substrates for the annealing experiments.

In the case of high annealing temperatures care has to be taken to insert and remove the samples slowly as thermal shock can lead to cracking of the films. Selected samples were left in the furnace to cool down overnight after it had been switched off.

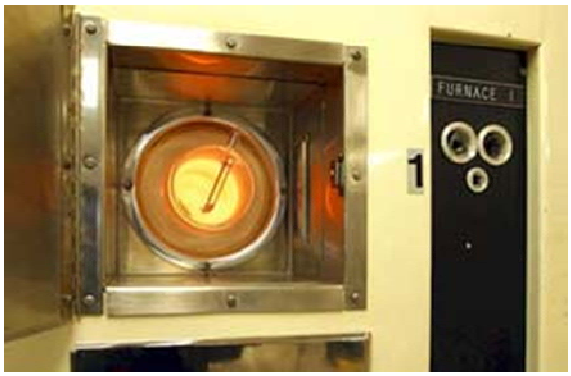

Figure 7: Front of furnace shows lid of one tube.

3.4 Reactive Ion Etching

Reactive Ion Etching (RIE) is an important technique for pattern transfer of various films and substrates in micromachining processes. In contrast to wet etching, it is a dry process which can be controlled easily, is scalable, causes no liquid waste and has a more anisotropic profile. Since little is known about dry etching characteristics and the associated mechanisms and effects on the material [4], RIE on sputtered ZnO was investigated with the aim to utilise the technique for future device application. A picture of the Oxford Instruments Plasmalab 80 Plus RIE is shown in Figure 8. This system has a capacitively coupled power supply. When comparing etch rates across various systems, one has to keep in mind that capacitively coupled plasma has a density around two orders of magnitude lower than inductively coupled plasma [37].

Figure 8: Oxford Instruments Reactive Ion Etcher ① with liquid nitrogen cooling system and nitrogen dewer ②.

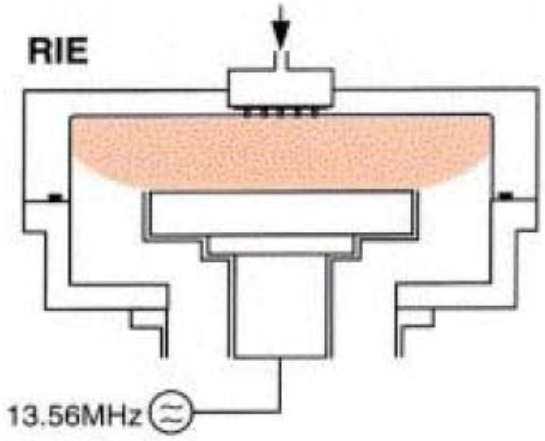

Figure 9: Schematic diagram of the RIE vacuum chamber.

In RIE mode, RF power is applied to the lower electrode to strike and maintain the plasma and to provide ion bombardment of the wafer through the generation of a DC bias on the lower electrode. This allows highly anisotropic etching of the inter-metal dielectric layers, avoiding undercutting metal tracks and maintaining the integrity of the circuit formed by these tracks.

An RIE process is controlled by a number of parameters including pressure, temperature, plasma power and frequency and etchant chemistry. The RIE uses a RF source of 13.56 MHz to create a plasma, where electrons have been ejected from the present atoms and molecules. The plasma is a mix of reactive and neutral species. The reactive species are a mix of ionised atoms and electrons, which either become etchants or recombine, a process that can be visualised through photon emission. Due to their higher mobility, the lighter electrons tend to recombine at the walls of the chamber. This results in a more positive charge on the plasma and areas of lower charge density near the walls, which are known as sheath regions. The lower densities allow ions to be accelerated across these regions to impinge on the substrate. The acceleration is performed by a bias voltage, which is set up when an equilibrium of positive and negative charge is met on the cathode. Since the charge flow on the cathode is initially dominated by electrons, the equilibrium is found with a negative bias on the cathode and the cathode's bias voltage is stabilised at a greater magnitude than the anode due to the cathode's smaller size. The bias influences the bombardment velocity and hence the anisotropy and speed of the etch.

Once the plasma and the bias voltage are set, the etching is generally performed through three mechanisms: sputtering, chemical gasification and energetic ion-enhanced chemistry. Sputtering is simply an ion bombardment process and hence has low selectivity

about the material it etches. To facilitate vertical etching, a long mean free path is required to allow normal incidence on the substrate surface. The long mean free path is provided by the low charge density sheath region. In contrast to sputtering, chemical gasification is a chemical etching process and thus provides excellent selectivity between a substrate and masking material. Plasma gases are chosen specifically to obtain beneficial surface chemistry to allow ions to react with the substrate and increase etching speed. This process tends to be isotropic.

To increase the anisotropy of the etch, sputtering and chemical gasification work together to produce energetic ion-enhanced chemistry. Here, the activation energy for the chemical gasification is provided through ion bombardment, which results in faster etches. Finally, ion-enhanced chemistry also allows passivation of vertical walls on the substrate. This protects the sidewalls, inhibiting sideways etching and allowing for a more anisotropic etch.

3.5 Electron beam lithography

Electron beam lithography (EBL) enables rapid prototyping down to sub-100nm features. The mask-less nature of the EBL also accommodates the production of arbitrary patterns, giving a great flexibility. The Raith 150 system we have used provides a fully integrated high-resolution large-area pattern generation system by combining a LEO 1500 series scanning electron microscope (SEM) with additional hardware, software and a laser-interferometer controlled stage. The system is largely automatic, simplifying load and unload procedures as well as system setup. A picture is shown in Figure 10.

Figure 10: Raith 150 EBL/SEM system.

In EBL, a controlled beam of electrons exposes patterns into an electron-sensitive resist. Obtaining a stable focused beam is achieved through a number of elements. The first is the electron source. In EBL systems electrons are produced by either field emission, where the electrons are extracted from a sharp electrode by an accelerating voltage or thermal emission, where electrons are thermally ejected from a heated metal element. In the case of the Raith 150, the column uses a combination of both thermal and field emission to attain both high beam current and low beam spread.

Once an electron flow has been created, it must be formed into a narrow beam. This is done by a series of lenses and apertures, which guide the beam down the column. The lenses are provided by magnetic coils which are adjusted regularly to maintain acceptable stigmation and focus. Scanning coils at the base of the column deflect the beam to facilitate vector scanning of patterns during lithography exposure. To produce arbitrary patterns a high-speed beam blanker is added to the column. The high data rates required by the scanning coils during operation are achieved by additional pattern generation hardware. Under ideal conditions the system is capable to pattern sub-20 nm features [38].

The entire system is in a high vacuum to increase the mean-free-path of the electrons so that they can travel unabated to the sample.

The most common electron-sensitive resist used in EBL is PMMA. It is spun to a thicknesses of about 100-200 nm onto the layer that requires patterning. Once exposed with the EBL, the exposed PMMA is removed with a developer, normally a solution of methyl isobutyl ketone (MIBK) in isopropyl alcohol (IPA) is used. Development conditions (temperature, agitation and dilution ratios) should be kept consistent. The

remaining PMMA then acts as a mask for the layer underneath and various techniques of pattern transfer are implemented.

The EBL system also doubles as an SEM and is a powerful tool for metrology with a maximum magnification of 1,000,000X. However, charging of insulating samples (i.e. glass or in our case, insulating ZnO films) or environmental influence such as vibrations can degrade the image quality.

3.6 Thermal evaporation

The thermal evaporator was used for metal depositions. A vacuum is created inside the chamber where a crucible holds the material to be evaporated while the sample is attached to a location in the chamber, such that material is deposited at a desired angle, mostly normal to the material flux. Two materials were able to be loaded in the chamber simultaneously, to allow the deposition of two metals without breaking the vacuum, i.e. Au was deposited on a NiCr sticking layer. Figure 11 shows the Balzers thermal evaporator.

Figure 11: Balzers 510-A thermal evaporation system.

3.7 Mask aligner

A Süss MA6 mask-aligner as shown in Figure 12 was used for optical lithography exposures. It houses a UV light source, optical systems for light collimation, a mask support and a substrate stage. There are a range of different setup conditions, including vacuum settings, mask-substrate gap, exposure times, light wavelength, mask-substrate alignment and others.

Figure 12: Süss MA6 mask-aligner.

The mask and sample are inserted into their respective holders and are secured by vacuum. The stage supporting the sample is then brought into contact with the mask while the pitch and roll of the stage are adjusted to provide parallel positioning of the mask and sample (wedge-error-correction). The stage then moves down a set value in the z-direction to allow alignment between the mask and sample to take place with the use of the microscope. The microscope is then displaced by optics that, once the shutter is opened, guides the exposing light through the mask and onto the sample. After the exposure the sample is lowered and removed.

Chapter 4
Characterisation methods

4.1 Photoluminescence spectra measurements

The photoluminescence measuring technique is used for measuring the distribution of defects in a crystal.

Photoluminescence is the optical emission obtained by photon excitation (usually a laser) and is commonly observed with semiconductor materials. This type of analysis allows non-destructive characterisation of the electronic structure of the band gap in semi-conductor materials and can provide an indication of the nature of structural and compositional defects within the material, such as the presence of unintentional dopants and surface related defects. These measurements were performed at the Department of Physics, in collaboration with Paul Miller.

In this system, as shown in Figure 13, a helium-cadmium (HeCd) laser with an output power of 25 mW and a wavelength of 325 nm (UV light) acts as the excitation source. The light is focused onto the sample which is located in a cold finger liquid helium cryostat. For our measurements, the samples were cooled down to 4 K. The emitted photoluminescence (PL) is collected by a collimating lens before being focused into a spex1700 spectrometer for dispersion. A photomultiplier tube is used to measure the intensity of the PL over the range of wavelengths.

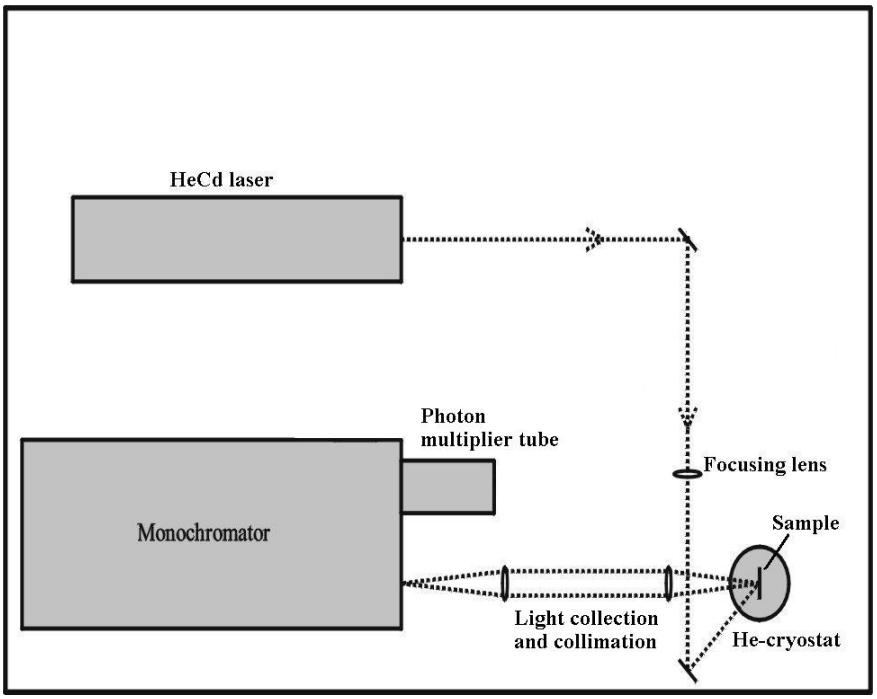

Figure 13: Schematic setup of PL measuring system.

Electrons in the sample are excited from the valence band to the conduction band, provided the photon energy from the laser is greater than the band gap of the material. In direct band gap semiconductors, such as zinc oxide, the electrons in the conduction band rapidly relax by emitting photons, corresponding to the band gap of the semiconductor. The electrons might also recombine with defects and perturbations within the lattice structure of the material, such as valence band holes. These additional energy states may be investigated by examining the energy of the emitted photons.

4.2 Rutherford backscattering

Rutherford backscattering (RBS) is based on collisions between atoms and derives its name from Lord Ernest Rutherford, a New Zealander. In 1911 he was the first to present the concept of atoms having nuclei.

Light ions (He^+) are beamed to the material surface of a sample. By measuring the number and energy of ions in the beam, which backscatter after colliding with atoms in the near-surface region of the sample, it is possible to determine atomic mass and elemental concentrations versus depth below the surface. RBS is ideally suited for determining the

concentration of trace elements heavier than the major constituents of the substrate. Its sensitivity for light masses and for the makeup of samples well below the surface is poor.

When a sample is bombarded with a beam of high energy particles, the vast majority of particles are implanted into the material and do not escape. This is because the diameter of an atomic nucleus is of the order of 10^{-15} m while the spacing between nuclei is of the order of 2×10^{-10} m. A small fraction of the incident particles undergo a direct collision with a nucleus of one of the atoms in the upper few micrometers of the sample. This "collision" does not actually involve direct contact between the projectile ion and target atom. Energy exchange occurs because of Coulomb forces between nuclei in close proximity to each other. However, the interaction can be modelled accurately as an elastic collision using classical physics.

The energy measured for a particle backscattering at a given angle depends upon two processes: Particles lose energy while they pass through the sample, both before and after a collision. The amount of energy lost is dependent on that material's stopping power. A particle will also lose energy as a result of the collision itself. The collision losses depend on the masses of the projectile and the target atoms. The ratio of the energy of the projectile before and after collision is called the kinematical factor.

The number of backscattering events that occur from a given element in a sample depend upon two factors: the concentration of the element and the effective size of its nucleus. The probability that a material will cause a collision is called its scattering cross section.

RBS measurements allow to investigate the stoichiometry of ZnO films and to search for impurities. Measurements were performed at the Institute of Geological and Nuclear Sciences (GNS), Lower Hutt, using a 1.0 MeV $^4He^+$ ion beam. The RBS detector was mounted under 165º in backscattering geometry, enabling a depth resolution at the surface of better than 20 nm. With this setup the stoichiometry of the films and impurities can be traced.

4.3 X-ray diffraction (Debye Scherrer)

X-ray diffraction (XRD) is a versatile, non-destructive analytical technique for identification and quantitative determination of the various crystalline compounds, known as 'phases', present in solid materials and powders. Diffraction is due essentially to the existence of certain phase relations. It is well known that two rays are completely in phase

whenever their path lengths differ by either zero of a whole number of wavelengths. Differences in the path length of various rays arise quite naturally considering how a crystal diffracts X-rays. Figure 14 shows the diffraction of a beam of parallel and monochromatic X-rays of wavelength λ is incident on a crystal at an angle θ, also known as Bragg angle, which is measured between the direction of the incident beam and the crystal plane under consideration.

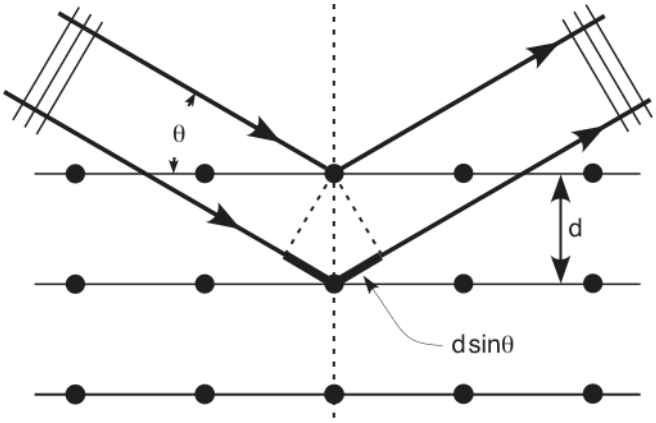

Figure 14: Diffraction of X-rays by a crystal.

The interaction with the first of these planes produces a reflected component at the specular reflection angle θ, which is rather weak if the X-rays are deeply penetrating. For the second and all subsequent planes, there are similar components of reflected energy at the specular angle θ. It can be seen from Figure 14 that the additional path of the lower ray compared to the upper ray is $2d \sin\theta$. Consequently all reflected components can interfere constructively in phase if this distance is a multiple of the wavelength. This condition for efficient specular reflection is known as Bragg's law

$$2d \sin\theta = n\lambda,$$

where n is an integer. Since the atomic arrangement is identical in all the planes under consideration, the Bragg diffraction condition depends on the spacing of the planes but is independent of the atomic arrangement within each plane. Since $\sin\theta$ cannot exceed unity, the basic condition $n\lambda < 2d$ must be satisfied to obtain any diffraction. For a spacing between planes in the order of 3 Å, λ cannot exceed 6 Å. On the other hand if λ is much smaller than d, the diffraction angles are too small to be conveniently measured. Experimentally, by using X-rays of known wavelength λ and measuring θ the spacing d of the planes in a crystal can be determined through Bragg's law.

Following the conventional definitions ω is the angle between the incident beam and the sample, while 2θ is the angle between the incident and diffracted beams, as shown in Figure 15. In a so called $\theta - 2\theta$ scan the analyser slowly rotates with a velocity that is twice the speed of the sample so that ω is always equal to θ. In this case only regions of the sample having constant lattice spacing d_θ contribute to the different reflexes. In the ω–scan the angle 2θ is maintained constant and just the angle ω is changed. Contributions to the reflex come just from sample regions which have well defined lattice spacing, determined by the angle 2θ. The variation of ω makes the tilt of different crystalline grains visible. If the measurement is performed with wide open detector, the full width at half maximum (FWHM) of the curve is obtained. The "rocking curve" is frequently used to quantity for evaluating the structural quality of epitaxial layers.

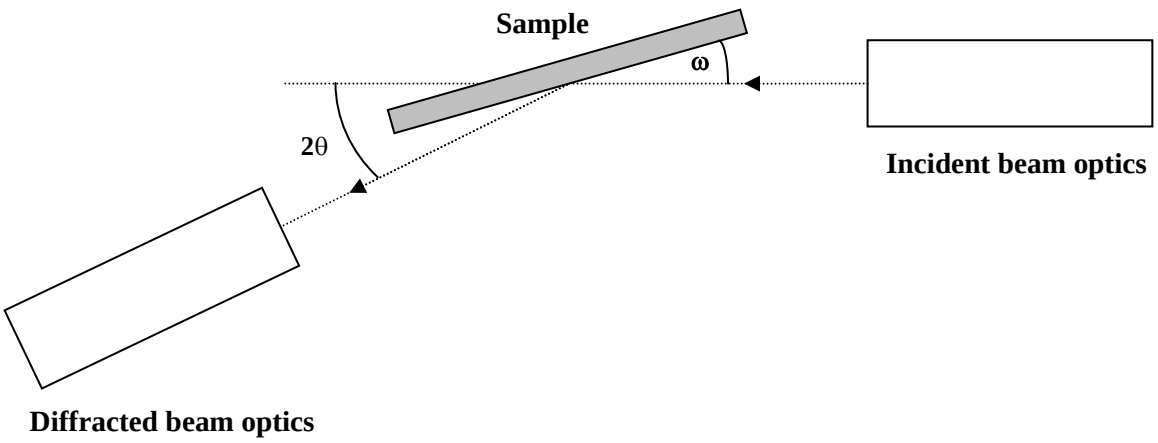

Figure 15: Schematic setup of a XRD measurement system.

About 95% of all solid materials can be described as crystalline. When X-rays interact with a crystalline substance (phase), a similar diffraction pattern is received. The X-ray diffraction pattern of a pure substance is, therefore, like a fingerprint of the substance. The powder diffraction method is thus ideally suited for characterisation and identification of polycrystalline phases. Today about 50,000 inorganic and 25,000 organic single component, crystalline phases, diffraction patterns have been collected and stored as PDF (powder diffraction file) standards. The main use of powder diffraction is to identify components in a sample by a search/match procedure. Furthermore, the areas under the peak are related to the amount of each phase present in the sample.

X-ray diffraction measurements were mainly collected in the Geochemistry laboratory at the University of Canterbury, in collaboration with Stephen Brown, and also at EPFL in Lausanne, Switzerland.

The XRD system at University of Canterbury consists of a source with an X-ray generator (X-ray tube operating at 50kV/40mA), a goniometer (stepping motor assembly) and a monochromator. The detector side consist of an X-ray proportional detector and a diffractometer control linked to a PC with control software and search/match processing software.

In the case of ZnO, we simply compared the measured values with values of ZnO powder contained in a database. Results using this method can be compared with any given materials.

Figure 16 shows the PDF file for powder ZnO. ZnO powder contains crystal in random directions with multiple peaks visible, whereas sputtered ZnO generally only contains grains which are oriented normal to substrate surface. This equals to a peak detected around 34.5 degrees.

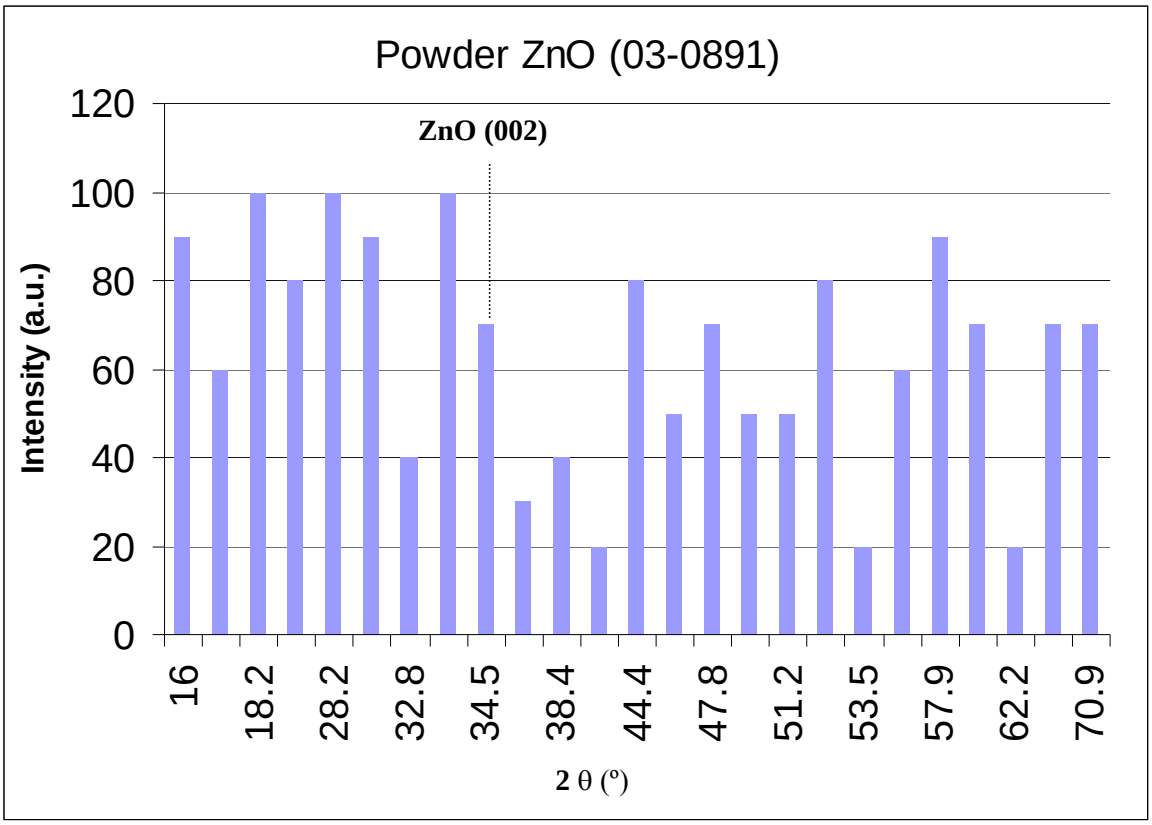

Figure 16: Theoretical XRD diagram showing all possible intensity graphs for powder ZnO, according to powder diffraction file 03-0891.

Strain, both uniformly and non-uniformly, will affect a particular x-ray diffraction peak as follows:

- A non-strained crystal lattice shows a diffraction line at a given angle (2θ)
- A uniformly strained crystal lattice shows a diffraction line at a slightly lower angle (2θ)
- A non-uniformly strained crystal lattice shows a wider diffraction line at a given angle (2θ) and with possibly lower peak count

4.4 Scanning electron microscopy imaging

Scanning electron microscopy (SEM) is a widely used surface analytical technique. SEM, accompanied by X-ray analysis, is considered a relatively rapid, inexpensive and basically non-destructive approach to surface analysis. High resolution images of surface topography, with excellent depth of field are produced using a highly-focused, scanning

(primary) electron beam. The primary electrons enter a surface with high energy and generate many low energy secondary electrons. The intensity of these secondary electrons is largely governed by the surface topography of the sample. An image of the sample surface can thus be constructed by measuring secondary electron intensity as a function of the position of the scanning primary electron beam. High spatial resolution is possible because the primary electron beam can be focused to a very small spot (diameter < 10 nm). High sensitivity to topographic features on the outermost surface (< 5 nm) is achieved when using a primary electron beam with an energy of < 1 keV. In addition to low energy secondary electrons, backscattered electrons and X-rays are also generated by primary electron bombardment.

We used mainly the Raith 150 in our department, which has both SEM and EBL capabilities. Samples sputtered with ZnO were directly placed on a sample holder. Charging problems became more or less apparent, depending on the thickness of the (insulating) ZnO coating or whether the substrate was insulating. To alleviate charging, a conductive layer was sometimes deposited over the sample, such as 10 nm of AuPd, or 5 nm of Ag.

4.5 Atomic force microscope imaging

An atomic force microscope (AFM) utilises a sharp probe moving over the surface of a sample in a raster scan. The probe is basically a tip on the end of a cantilever which bends in response to the force between the tip and the sample. As the cantilever flexes, the light from a laser is reflected onto a split photo-diode. By measuring the difference signal (A-B) changes in the bending of the cantilever can be measured. Since the Cantilever obeys Hooke's Law for small displacements, the interaction force between the tip and the sample can be determined.

The movement of the tip or sample is performed by an extremely precise positioning device made from piezo-electric ceramics, most often in the form of a tube scanner. The scanner is capable of sub-angstrom resolution in x-, y- and z-directions. However, some limiting factors have to be taken in account. Depending on the tip shape, the resolution will be limited as a tip is not able to profile sides of surfaces steeper than the sidewall angle of the tip. For more information refer to [39]. For this project, the department’s AFM, a Digital Instruments 3100 has been used.

The AFM was used for surface topology scans, determination of surface roughness and for the determination of etch rates.

Tip contamination is a common annoyance in microscopy. A large number of scans turned to waste due to tip contamination by the rather soft ZnO. Therefore SEM imaging was used with preference.

4.6 Piezoelectric force microscopy

The Piezoelectric force microscopy (PFM) is an exciting new technique that allows the scanning of local electromechanical (piezoelectric) properties down to the nanometer scale. It is based on the AFM and was developed at EPFL in Lausanne, Switzerland, by Enrico Colla and Alexei Gruverman. For a more detailed description of this technique and its applications refer to [40-43].

While PFM has been intensively utilised for probing ferroelectric materials, more recently it has also been used for ZnO nanobelts [44] as well as GaN studies [45, 46].

Scans of our samples were performed in collaboration with Nagarajan Valanoor at the University of New South Wales. The results contained important findings and were published for the first time in 2007 [47] and led to increased activity in this specialised field. Other papers about PFM on ZnO [48, 49] followed.

Essentially PFM is based on the detection of local electromechanical vibration of the sample caused by an external AC voltage. The voltage is applied through the probing tip, which is used as a movable top electrode. The external driving voltage with frequency ω generates a sample surface vibration with the same frequency due to the converse piezoelectric effect. This surface displacement can be approximated by:

$$\Delta z(t) = \int_0^{t_F} d_{33} E_{AC}(t,z)\,dz \qquad (1)$$

where E_{AC} is the AC electric field as a function of time t and displacement z and t_F is the thickness of the ferroelectric (or piezoelectric) layer. The modulated deflection signal from the cantilever, which oscillates together with the sample, is detected using the lock-in technique. The amplitude of the first harmonic signal from the lock-in amplifier is a function of the magnitude of piezoelectric displacement and phase shift between the AC field and the cantilever displacement. Thus, the magnitude of the displacement is recorded

on one channel of the lock-in amplifier and the phase (orientation of the polar surface) simultaneously on the other channel. The phase signal relates to domain orientation, with up domains therefore providing a positive contrast (bright in PFM phase images) and down domains negative contrast (dark image regions). This means that regions with polarization in the opposite orientation will vibrate in counter phase with respect to each other under the applied AC field and hence appear as regions of strong contrast in the piezoresponse image (those with zero phase difference appear brown and those with a phase difference of 180^{o} appear black).

The images are obtained through a modified AFM technique, as shown in Figure 17. It is a non-destructive method and collects high-resolution nanoscale information. A multimode atomic force microscope (AFM) was employed for the visualisation of the domain structure. Pt/Ir coated cantilevers, with a typical tip radius of 7 nm, a force constant 0.2 N/m and a resonant frequency of 13 kHz, were used at a scan rate of 0.8 Hz. An AC signal $Vac=Vosin(\omega t)$ with amplitude 1.5 V and frequency 7 kHz was applied between the AFM tip (movable top electrode) and the bottom electrode of the sample to acquire the images with the aid of two lock-in amplifiers.

As with AFM scanning, little sample preparation is necessary. A conductive base substrate (highly doped Si) or conductive bottom electrode (Pt on Ti adhesion layer) is sufficient to achieve good scans. Because the piezoelectric response of a sample is caused by an electric charge and the reverse piezoelectric effect, good results can be obtained from highly resistive ZnO films, as reported in [25].

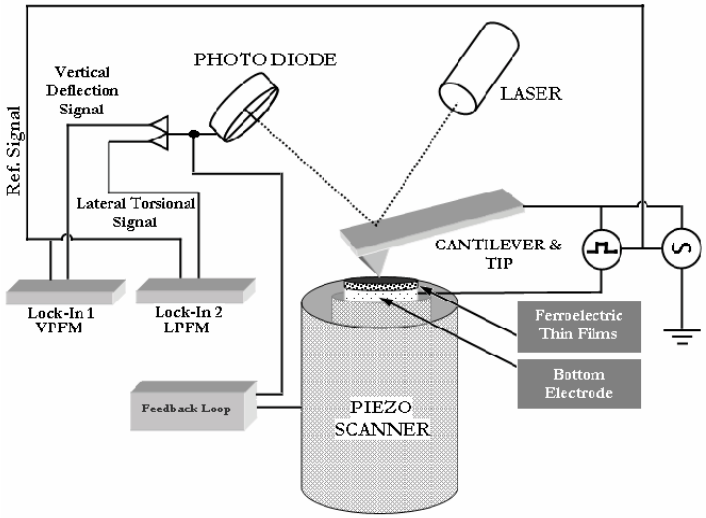

Figure 17: Schematic diagram of the PFM setup for ferroelectric domain imaging at UNSW (from [50]).

4.7 Single beam interferometry system

In order to determine the piezoelectric properties (d_{33}) of sputtered ZnO a single-beam *Michelson* interferometer was employed. In this set-up, an interference pattern is produced by splitting a beam of light into two paths, bouncing the beams back and recombining them. It is the most common configuration for optical interferometry and was invented by Albert Abraham Michelson. Michelson received the Nobel Prize in Physics in 1907.

The system at Macquarie University, Sydney was used for this work. The schematic setup is shown in Figure 18. A full description can be found in [51] and further information is available in [52, 53]. The interference of two beams produces a series of dark and bright images known as the fringes. In order for the fringes to appear, it is necessary to use a monochromatic (or nearly so) extended source. The system at Macquarie University uses a He-Ne laser (Uniphase 1135p) as the light source. The output is a continuous wave (CW) with a wave length of 633 nm. Figure 19 shows the optical setup and the instrument rack is shown in Figure 20.

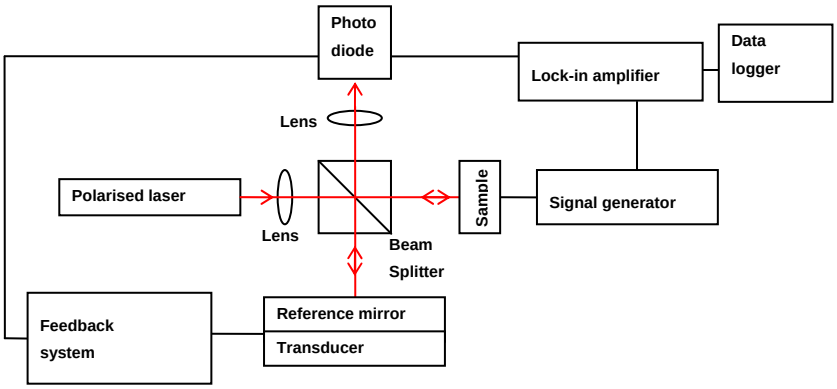

Figure 18: Michelson interferometry setup consisting of a laser (beam shown in red), the sample to be measured, tuneable reference mirror and a 50:50 cubic beam splitter.

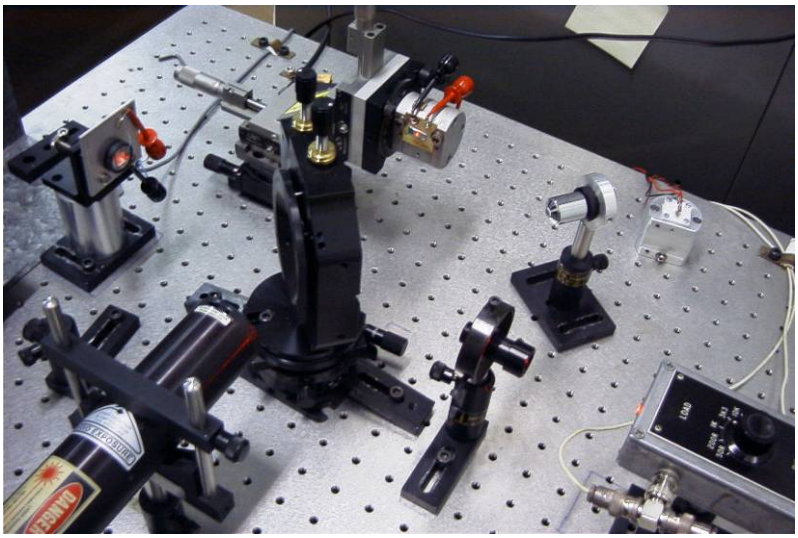

Figure 19: Setup of optical table for interferometric measurement of d_{33}.

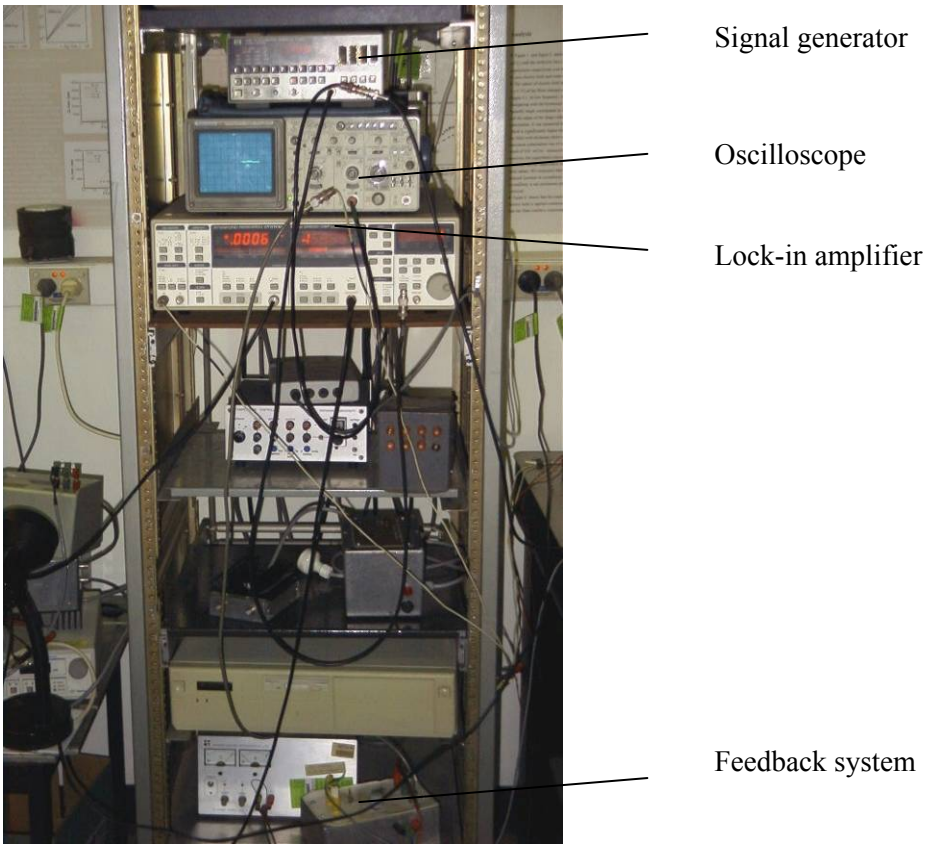

Figure 20: Instrument stack showing main components of the measurement system

However, the single beam interferometry technique is inherently sensitive to sample buckling as reported in [52] and also explained later. The system is very sensitive to temperature change, drafts, ambient light change and vibrations. Before performing measurements, the system was left on for an hour to reach thermal equilibrium. The "best" measurements were obtained after-hours, since disturbances such as vibrations from nearby elevators were kept to a minimum.

4.8 Double beam interferometry system

The double-beam *Mach–Zender* interferometer [52] is a further development based on the single-beam Michelson interferometer. The double beam set-up automatically eliminates the errors introduced by bending/warping of the sample, as the probing beam reflects simultaneously from both the front and back faces of the sample.

The system at EPFL, Lausanne, Switzerland was used for these measurements.

The optical arrangement of the double-beam interferometer is shown in Figure 21. Figure 21a shows the sample in relation to the two laser beams. The polarised beam from a He–Ne laser (Spectra Physics model 117A) passes through a diaphragm and travels to a λ/2 plate, which rotates the polarisation vector of the incident light. The λ/2 plate is used to equalise the light intensities in the reference and probing arms of the interferometer. A polarised beam splitter, PB-1, is used to split the probing and the reference beams. The probing beam reflects from the driving electrode and returns to PB-1 with the polarisation changed by 90° due to the λ/4 plate. Subsequently, the probing beam is reflected in the orthogonal direction by PB-1 to the mirrors M-1 and M-2 and similarly probes the back side of the substrate just opposite to the probing point at the driving electrode. Therefore, the back side of the substrate needs to be polished to optical quality and coated by a reflecting metallic layer as well. The lenses L-1 and L-2 focus the incident beam onto the sample.

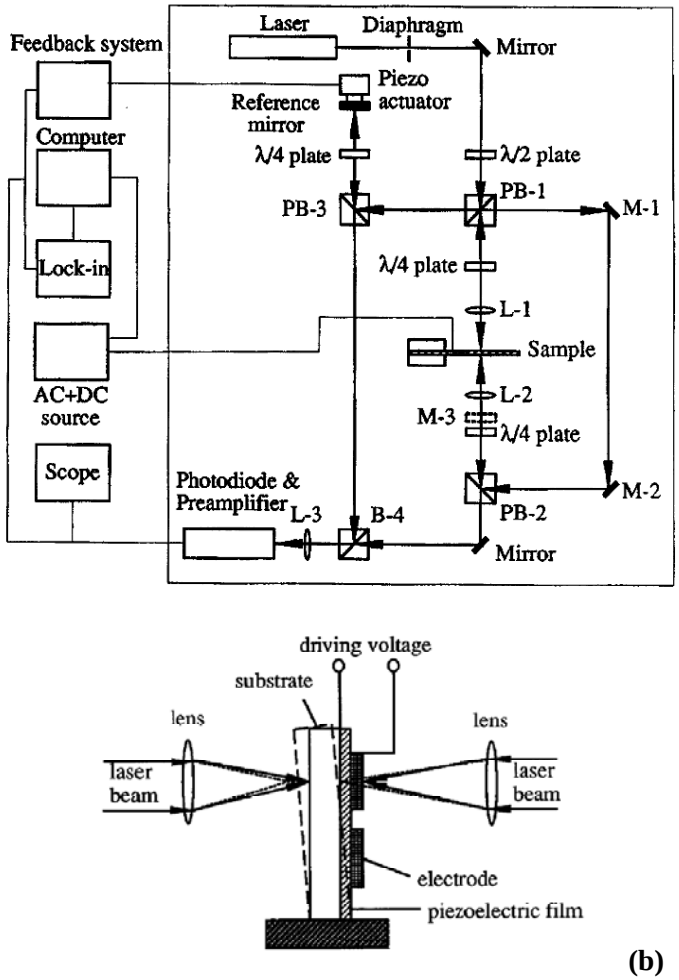

Figure 21: (a) Schematic of the double-beam laser interferometer and (b) principle of the elimination of bending motion of the substrate (from [52]).

4.9 Resistance measurement

The resistance across two probes was measured using the semiconductor parameter analyser HP 4155A and the probe station, as shown in Figure 22. The probe station is contained in a shielded and light proof cabinet. This is an approximate measurement only, as the shape of the contact electrodes and the manual positioning does not allow repeatable positioning with regard to distance between the electrodes and the contact area. The distance between the two probes was kept at 1 mm.

Figure 22: Semiconductor parameter analyser HP 4155A with probe station in background.

For sputtered films which were Zn-rich, resistance values of 12.78 kΩ were measured (i.e. conductive). Stoichiometric films however, showed very high values, the same as when a glass slide without any added coating was measured. Individual results are listed in Appendix C. Later measurement were performed using Schottky contacts, which are listed in Chapter 8.2.1.

Chapter 5
ZnO deposition

5.1 Common deposition methods

ZnO can be deposited or grown using a multitude of methods, which are listed in Table 2.

Method	Outcome	Reference
Bulk ZnO grown by vapour-phase transport method	Single crystal boules	[54]
Bulk ZnO grown by pressurised melt method	Single crystal boules	[55]
Bulk ZnO grown by hydrothermal method	Single crystal boules	[56]
ZnO thin films on sapphire grown by PLD	Epitaxial thin films	[57]
ZnO thin films on sapphire grown by molecular beam epitaxy (MBE)	Epitaxial thin films	[58, 59]
Chemical vapour deposition (CVD)	Thin films	[60]
Vacuum arc plasma evaporation	TCO	[61]
Metal-organic chemical-vapour deposition (MOCVD)	Thin films	[62]
Polymer assisted deposition (PAD)	Epitaxial thin films	[63, 64]
Zinc oxide films formed by oxidation of zinc	Nanostructures	[65, 66]
Sputtered ZnO	Thin films	[6, 25, 67-81]

Table 2: List of various known deposition methods.

The sputtering method was the obvious choice for this research as it was already established in earlier experiments [82]. Sputtering is a "cheap", relatively fast and well established technology. During the experimental work towards my ME, we proved qualitatively that sputtered ZnO can be optimised to have piezoelectric properties.

For this, the ZnO thin films must have a columnar structure with void-free grain boundaries [67, 73]. In order to achieve a high piezoelectric coefficient for the required thickness extensional mode, columnar ZnO grains with the c-axis perpendicular to substrate are required.

5.2 Thin film sputtering of piezoelectric ZnO

In this work, *reactive magnetron* sputtering has been used for most experiments. *Reactive* sputtering means that an oxide film is grown by the sputtering of a metallic target (Zn) in an oxidising atmosphere using DC sputtering. This technique has the potential to achieve films with piezoelectric properties [74, 78, 83-85] suitable for SAW devices. Since RF sputtering has a proven track record for piezoelectric properties as well [73, 75, 76] it was decided to perform additional sputtering experiments using an insulating ZnO target and to compare the outcomes. *Magnetron* sputtering utilises magnetic cathodes which trap the secondary electrons in the magnetic field close to the target. This technique increases the sputtering yield of the cathode and allows the use of lower pressures during the process for improved film finish. As reported in [25] a low sputtering rate promotes the oxidation of the target, leading to a better stoichiometry.

For our intended use, ZnO should have the following properties:

- Preferred crystal structure ([002] orientation, crystal growth normal to surface)
- Highly insulating
- Piezoelectric characteristics

ZnO can be sputtered on a wide range of materials and on irregularly shaped objects. Sputtered ZnO films show, with a proper fine-tuning of parameters, a natural tendency to grow with a preferred [002] orientation, which is necessary for the coating to be piezoelectric.

Figure 23 shows the microstructure zone diagram of metal films deposited by magnetron sputtering. T is the substrate temperature and T_m is the coating material melting point. It clearly illustrates that Zone 1 is the desired working area during sputtering. That is columnar growth of individual crystals defined by voided growth boundaries. These voided growth defects are a consequence of atomic shadowing. Shadowing induces open

boundaries because high points on the growing surface receive more coating flux than valleys, particularly when a significant oblique component is present in the flux [86]. This means, a low sputtering temperature and the proper pressure range are critical to achieve the proper crystal composition.

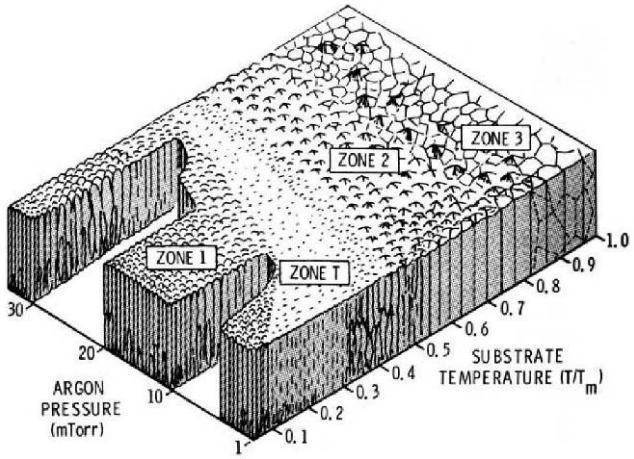

Figure 23: Microstructure zone diagram for metal films deposited by magnetron sputtering (from [86]).

It has to be noted that ZnO could contaminate semiconductor fabrication equipment through its oxygen content. A simple way around this is the application of a passivation layer. A thin silicon nitride layer, which prevents contamination, can be deposited to cover the ZnO layer [87].

5.2.1 Investigation of the growth mechanism of DC sputtered ZnO

In order to study the forming mechanism of polycrystalline films, a series of short depositions were performed on glass slides using DC sputtering. As usual, the glass slides were not pre-heated prior to sputtering.

Sputtered films grow from the vapour phase. Initially, adatoms form on the glass substrate and have still enough energy to migrate and coalesce with other adatoms. After a sputtering time of only 30 seconds, individual nucleation islands with a diameter of less than 20nm are visible, as shown in Figure 24, Sample 1. With longer sputtering times, shown in Figure 24, Sample 2 down to Sample 5 these islands grow in diameter until the voids become small and the islands coalesce to form bigger grains and a continuous film.

Note: Some SEM micrographs show charging, therefore blurring causes the nucleation islands to appear bigger than in reality. Thickness readings are approximate only (average as indicated by the crystal monitor).

Sample 1

Sputtering time: 30 sec
Indicated thickness ~2.5 nm

The deposited structures are nanodots with a diameter between 10 and 20 nm.

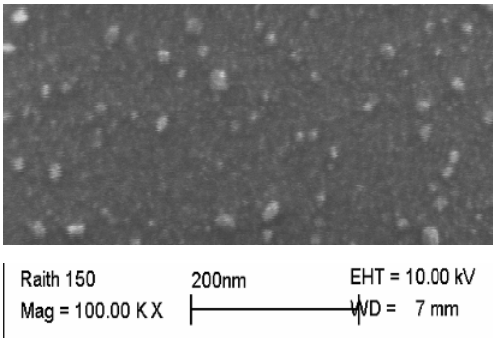

Sample 2

Sputtering time: 1 min
Indicated thickness ~ 6.3 nm

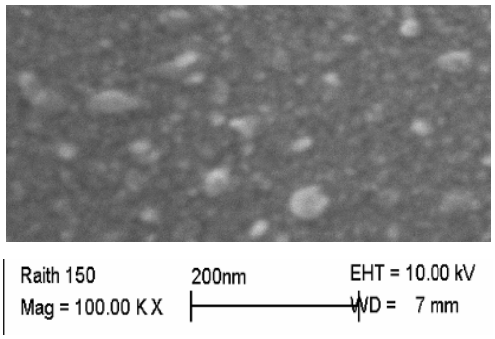

Sample 3

Sputtering time: 2 min
Indicated thickness ~ 11.7 nm

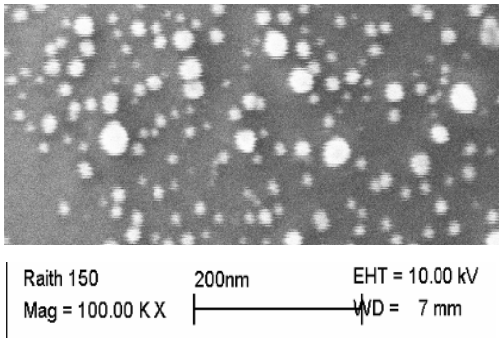

Sample 4

Sputtering time: 4 min
Indicated thickness ~ 18.1 nm

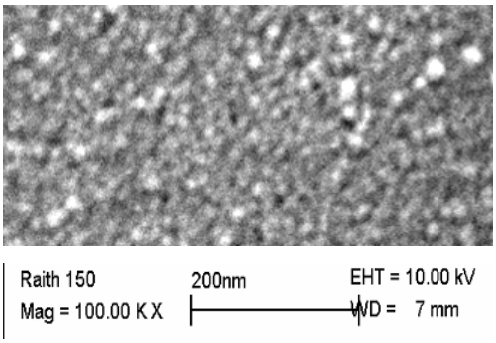

Sample 5

Sputtering time: 10 min

Indicated thickness ~ 80 nm

Outcome:

Fully developed ZnO film.

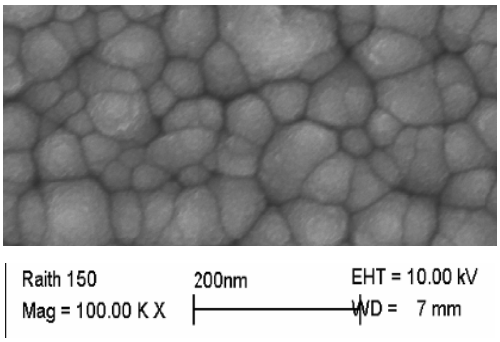

Figure 24: SEM micrographs of ZnO deposited on glass shows the forming of nucleation islands.

This effect is also described in [88]. It suggests that a sputtered ZnO film needs to have a minimum thickness of > 50 nm for the grains to properly develop for full coverage of the substrate, as shown in Figure 25 .

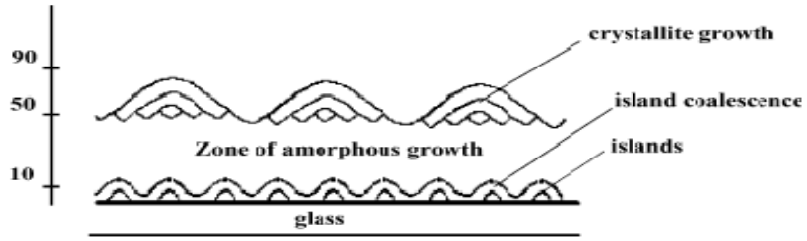

Figure 25 Schematic diagram of the structural evolution of ZnO thin film deposited on glass substrate. The ordinate axis shows the film thickness in nm (from [88]).

During sputtering the films receive particles with sufficient kinetic energy and therefore adequate mobility, which allows rearranging of the structure. Surplus O_2 and other impurities are displaced to the grain boundaries. Other authors [25] suggest that a mechanism called “preferred nucleation” occurs if there is only a weak interaction between the nucleus and the substrate surface. In that case, nuclei having a plane of low surface energy parallel to the substrate surface will form, provided the experimental conditions are such that equilibrium can be attained. This is the case when the atom (surface) mobility is not too small and the flux of growth species towards the substrate is not too large.

5.2.2 Issues affecting sputtering quality

The sputtering and the quality of the deposited films depends on a multitude of factors. During a deposition run target poisoning [89, 90] as well as the accurate control of gas flow and chamber pressure can make or break a "good" deposition. Long term drifts tend to be harder to detect. Over time the geometry of the sputter setup is changing due to target eroding. The sputtering chamber is coated by insulating ZnO deposits, which lead to a "disappearing" anode. The vacuum chamber and all auxiliary parts (sample, sample holder, shutter and shield) are normally grounded and act as anode. However, during sputtering these parts are progressively covered by the sputtered material, which makes them partially insulating. Besides that, the sputtering system is also used for other processes using various metallic or insulating materials, which inevitably leads to cross-contamination. Also, the contamination of vacuum gauges leads to false indications, while the repair or exchange of faulty components (i.e. turbo pump) will certainly require a recalibration of the process. A thorough clean of the whole system certainly helps to achieve fast pump-down times and repeatable, high quality deposition.

5.2.2.1 Target poisoning

The DC reactive sputtering technique has one drawback: target "poisoning". The chemical reactions between Zn and O_2 occur not only in the vacuum but on the sputter target surface as well. This leads to an insulating coating on the target and therefore lower currents and reduces the thin film growth rate.

Figure 26 shows a typical hysteresis curve obtained when a metal target is sputtered in a reactive gas [35]. As the reactive gas flow rate is increased, a sudden transition occurs where a compound forms on the surface of the target. The sputter rate drops and the partial pressure of the reactive gas increases, which leads to further target poisoning (positive feedback loop).

Generally, the conditions required to obtain a highly stoichiometric compound are at the knee of the hysteresis curve and therefore the process is carried out in an unstable condition. Very careful control of the gas flow is thus required.

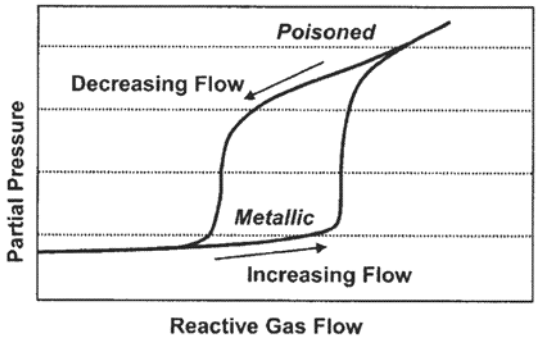

Figure 26: Schematic hysteresis loop in reactive sputtering (from [91]).

5.2.3 Successful DC sputtering procedure

After preliminary experiments on our sputtering system, the sputtering procedure was defined as follows:

1. Load samples on sample holder, locate above sputter target for uniform sputtering
2. Pump down to 10^{-5} mbar
3. Introduce O_2 (9 sccm)
4. Introduce Ar (6 sccm), or amount necessary to desired pressure of 1.2×10^{-2} mbar
5. Set up DC plasma source (nominally 250 W)
6. Ignite plasma
7. Presputtering for ten minutes
8. Sputtering to required thickness

Following these steps, the sputtered films normally achieve the desired properties

5.3 Comparisons between DC and RF sputtered ZnO films

During the ME Thesis research we proved that DC sputtered ZnO has the necessary piezoelectric properties for use as SAW device. Highly piezoelectric films were grown at our institute and SAW devices were fabricated and successfully tested. However to achieve a complete picture we decided to perform experiments using RF sputtering as well.

One of the advantages of RF sputtering is that materials from insulating targets, such as ZnO can be sputtered. However, compared with a DC setup, RF sputtering requires a more

expensive RF power supply and additionally an RF-matching unit and the striking of the plasma is not always straight-forward.

For this assessment, all parameters were kept identical as far as possible, including geometry, vacuum and power settings. While DC sputtering was performed using reactive sputtering (by introducing Oxygen) and Argon as sputtering gas, RF sputtering from a ZnO target was performed with Argon as sputtering gas only. In this chapter we compare the results of sputtering comparisons using SEM, AFM, RBS and resistive measurements. More in-depth comparisons follow in Chapter 6 and Chapter 7.

The following micrographs are of DC and RF sputtered ZnO on glass substrates:

DC sputtered ZnO

Deposition

- Using Zn target (reactive sputtering)
- Sputtering gas Ar (6 sccm)
- Reactive gas O_2 (9 sccm)
- Deposition power = 250 W
- Chamber pressure = 1.2×10^{-2} mbar

RF sputtered ZnO

Deposition

- Using ZnO target
- Sputtering gas Ar (15 sccm)
- Deposition power = 250 W
- Chamber pressure = 1.2×10^{-2} mbar

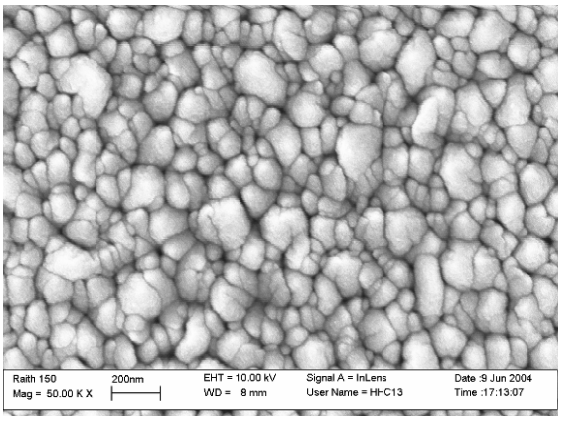

(a) SEM micrograph of DC sputtered ZnO

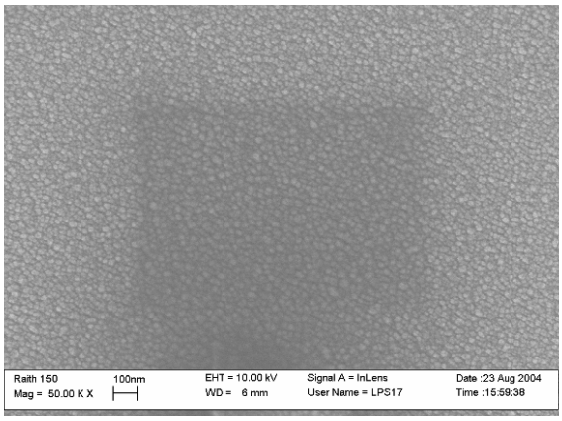

(b) SEM micrograph of RF sputtered ZnO

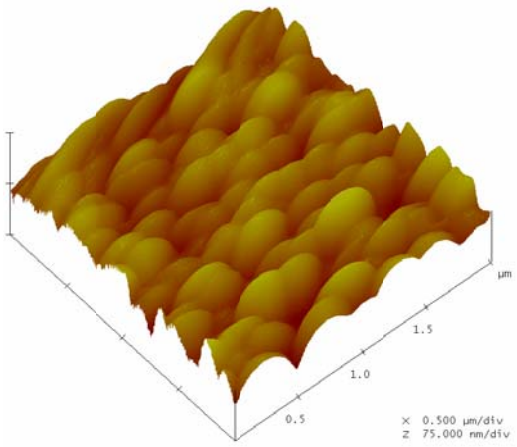

(c) AFM micrograph of DC sputtered ZnO

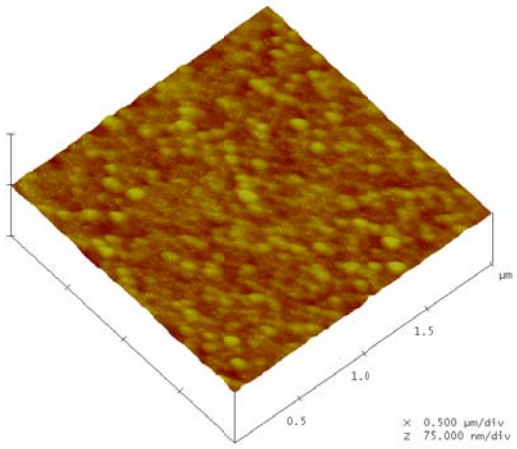

(d) AFM micrograph of RF sputtered ZnO

Figure 27: Various AFM and SEM micrographs of DC and RF sputtered ZnO.

Figure 26 shows the SEM micrographs of DC (a) and RF (b) sputtered ZnO. In (c) and (d) the AFM micrographs of DC and RF sputtered ZnO, repectively are shown.

Outcome (DC sputtered ZnO)

Deposition rate ≈ 10 nm/min

Analysis from AFM micrographs:

- Average grain diameter: 200 nm
- Grain height: 40 nm
- Surface RMS roughness: 75 nm
- Resistance: Insulating (same as glass) (according to method listed in Chapter 4.9)

Outcome (RF sputtered ZnO)

Deposition rate ≈ 35 nm/min

Analysis from AFM micrographs:

- Average grain diameter: 50 nm
- Grain height: 5 nm
- Surface roughness: 7 nm
- Resistance: 10 kΩ (according to method listed in Chapter 4.9)

These experiments clearly show, that DC sputtering using the recipe given in Chapter 5.2.3 yields high resistivity films, which in turn should have high d_{33} values. With our sputtering system, the same outcome may be achievable using RF sputtering, however detailed optimisation studies would be necessary. Other authors [92] also found that DC sputtered films are not electrically conductive, while RF sputtered films (using the same setup) have conductive properties.

Using reactive DC sputtering, the stoichiometry of the sputtered films can be set by changing the gas ratio, which is a fairly straight forward task. Therefore we decided to focus on DC sputtering.

The SEM micrographs in Figure 28 show cross sections of DC sputtered ZnO. The individual grains and some voids in the grain boundaries are clearly visible. For further comparisons between DC and RF sputtered ZnO please refer to [79].

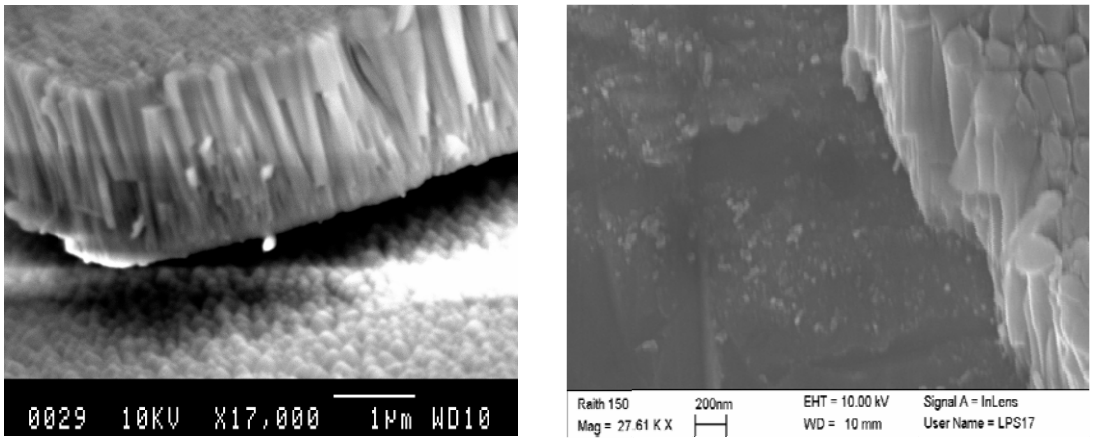

Figure 28: Cross sectional SEM micrographs show a suspended ZnO thin film with a thickness of around 1.5 μm on the left-hand side. On the right-hand side another film with a thickness of around 1 μm is shown.

Both the DC and RF sputtered films appear transparent on glass and have a 1:1 (Zn:O) stoichiometry throughout the films, as determined by RBS.

5.3.1 RBS results of various DC and RF sputtered samples

RBS scans were performed both on DC and RF sputtered samples to determine the stoichiometry of the films.

DC sputtering using reactive sputtering allows the stoichiometry to be set by adjusting the gas ratio, as explained in Chapter 5.2. In Figure 29 the graphs of six samples are shown. The steps shown in the channel area just under 300 are O peaks and the steps shown in the channel area from 420 to 500 are Si peaks, Si is measured from the base material of the glass sliders (SiO). The steps shown in the channel area of around 320 are O peaks measured from the film. The peaks shown in the channel area from 600 to 700 are Zn peaks and the width of the peak is a measure of the thickness of the coating. Good stoichiometry is confirmed for the samples ZnO-2 and ZnO-3.

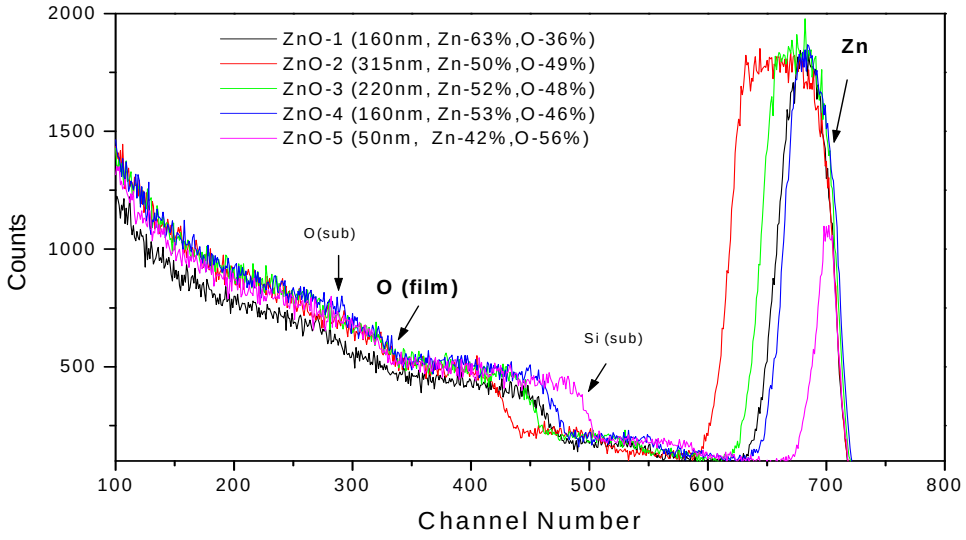

Figure 29: RBS spectra of ZnO films deposited using DC sputtering on glass.

Film	Thickness (nm) *	Composition (at.%) ± 1%	Zn/O ratio	Surface roughness (estimate)	uniformity	Thickness of oxygen rich layer at surface (nm)
ZnO-1	160 ± 20,	Zn= 63% O=36%	1.75	≈30 nm	Ok	10 ± 5
ZnO-2	315 ± 20,	Zn= 50% O=49%	1.02	≈50 nm	Ok	20 ± 5
ZnO-3	220 ± 20,	Zn= 52% O=48%	1.08	≈30 nm	Ok	10 ± 5
ZnO-4	160 ± 20,	Zn= 53% O=46%	1.15	≈30 nm	Ok	10 ± 5
ZnO-5	50 ± 10,	Zn= 42% O=56%	0.75	≈20 nm	Ok	N/A

* ZnO thickness based on density as 5.6 g/cm^{-3}

Table 3: Detailed RBS results of ZnO film deposited using DC sputtering on glass.

The RBS results, as shown in Figure 30 for the RF sputtered films RF01 to RF05 (not RIE) show that the stoichiometry of all films is 1.0, i.e. the Zn to O ratio is 1.0.

Furthermore, some films show signs of two heavy element impurities. In the spectra they are labelled Sn and Au.

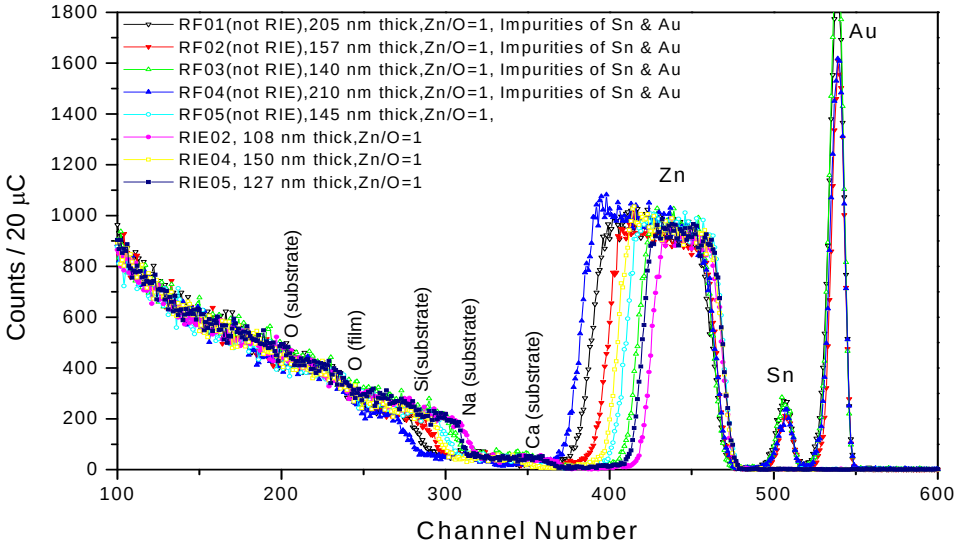

Figure 30: RBS spectra of ZnO films deposited using RF sputtering on glass.

The DC sputtered films have grains with a diameter in the range of 200nm while RF sputtered grains have smaller grains with a diameter in the range of 50 nm. It has to be noted that DC sputtering was performed from a metallic Zn target, while RF sputtering was performed from an insulating ZnO target.

On selected DC sputtered samples it was attempted to perform Hall effect measurements. Because the optimised films have too high resistivity compared with the capabilities of our system (utilising a 0.52 Tesla magnet) no useful results were obtained.

Resistive measurements using a probe station were unsuccessful. The semiconductor parameter analyser detected the same high resistivity values both for a naked glass substrate and a substrate with a ZnO thin film on top. However, measurements of Schottky contacts fabricated on ZnO deposited on Si substrates were successful. For results please refer to Chapter 8.2.1.

Summary

ZnO can be deposited using a multitude of techniques. One of the most commonly used methods, sputtering, was used for this work. Sputtered films yield grains that grow preferably normal to the substrate surface. DC sputtered films have been optimised to yield highly resistive films which have the potential to achieve good d_{33} values. In contrast, RF sputtered films have lower resistivity.

Chapter 6
Post-sputtering treatments: Results of annealing and dry etching

6.1 Introduction

It is generally accepted that annealing is an effective method to improve the quality of thin films [93-98]. During annealing the overall atomic mobility increases, which leads to lower intrinsic stress, distortion and lattice mismatch. At higher temperatures this can lead to interdiffusion between substrate and film.

In addition, reactive ion etching (RIE) was performed on selected samples. RIE generally introduces slight structural damage and surface roughening on the films.

The first part of this chapter describes the results of post-annealing and RIE on DC and RF sputtered ZnO films on Si substrates. The films were annealed at temperatures of up to 900 °C, followed by RIE. Analysis was performed using XRD, SEM, RBS and PL.

The second part focuses on ZnO films, deposited using DC sputtering, this time on multiple substrate materials and higher annealing temperatures. Most reports list annealing temperatures only up to 900 °C [81, 97, 99]. However, in order to gain further insight, we attempted to increase the annealing temperatures to up to 1200 °C, the highest temperature the furnace allowed.

6.2 Results and discussion of ZnO deposited on Si substrate

Various films were deposited using DC and RF sputtering method to a thickness of approx. 500 nm and annealed in N_2 atmosphere. Details of the sputtering method are listed in Chapter 3.2 and Chapter 5 and the annealing procedure is described in Appendix B.

The XRD scans (shown in Figure 31) on the as-grown DC sputtered films showed only one peak at 34.18°, which confirmed strongly c-axis oriented (002) polycrystalline growth of ZnO. For RF sputtered films, there was only one weaker peak at 34.08°, which confirmed c-axis oriented (002) polycrystalline growth.

Both DC and RF sputtered films appeared transparent on glass and had 1:1 (Zn:O) stoichiometry throughout films (without post-annealing), as determined by RBS depth profiling.

The PL response on as-grown films was very weak as shown in Figure 32 for DC sputtered ZnO and Figure 33 for RF sputtered ZnO, respectively. Therefore post-growth annealing was performed.

SEM micrographs show the film surface and grain size of as-sputtered ZnO in Figure 34(a) for DC sputtered ZnO and Figure 35(a) for RF sputtered ZnO.

6.2.1 Annealing

The ZnO thin films on Si substrates were annealed at 600 to 900 °C in N_2 atmosphere for 30 min. During annealing the overall atomic mobility increased, which led to lower intrinsic stress, distortion and lattice mismatch as evident by XRD measurements. The results are shown in Figure 31 for DC and RF sputtered ZnO and show increased peak values up to a temperature of 800 °C, which indicated improved crystallinity due to annealing. At 900 °C however, the peak values decreased slightly, which indicated some disturbance of the crystal structure. The FWHM however, continued to decrease with higher annealing temperature. This was in agreement with annealing experiments as reported in [97, 99, 100]. A slight shift of the (002) peak position was observed; it was caused by relaxation of the films during annealing.

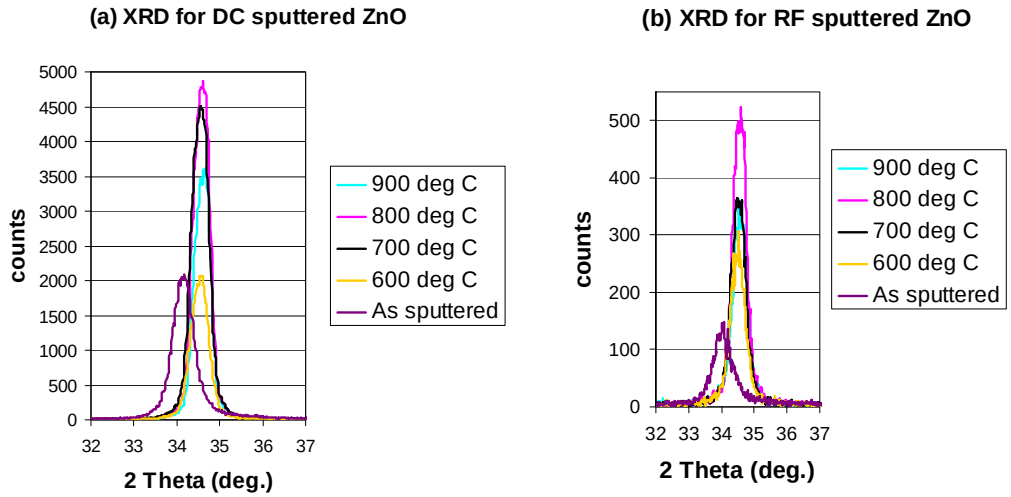

DC sputtered ZnO

Annealing temperature	As sputtered	600 °C	700 °C	800 °C	900 °C
FWHM ZnO (002) peak	0.532	0.484	0.488	0.47	0.466
Peak angle (Degrees)	34.18	34.54	34.56	34.62	34.66

RF sputtered ZnO

Annealing temperature	As sputtered	600 °C	700 °C	800 °C	900 °C
FWHM ZnO (002) peak	0.536	0.446	0.516	0.482	0.492
Peak angle (Degrees)	34.08	34.52	34.48	34.6	34.52

Figure 31: (a) XRD scan for DC sputtered ZnO and (b) for RF sputtered ZnO at various annealing temperatures. The tables show the FWHM and peak angle for different annealing temperatures.

The strength of the PL generally increased with annealing temperature both on DC and RF sputtered ZnO, as shown in Figure 32 and Figure 33 (all PL measurements were performed at 4 K). PL of DC sputtered ZnO had about 30 times higher intensity compared with RF sputtered ZnO.

For DC sputtered ZnO the PL intensity increased dramatically to up to 800 °C annealing temperature, as shown in Figure 32. The two peaks in the near band edge region are the donor-acceptor pair at 3.32 eV and a neutral donor bound exciton at 3.355 eV.

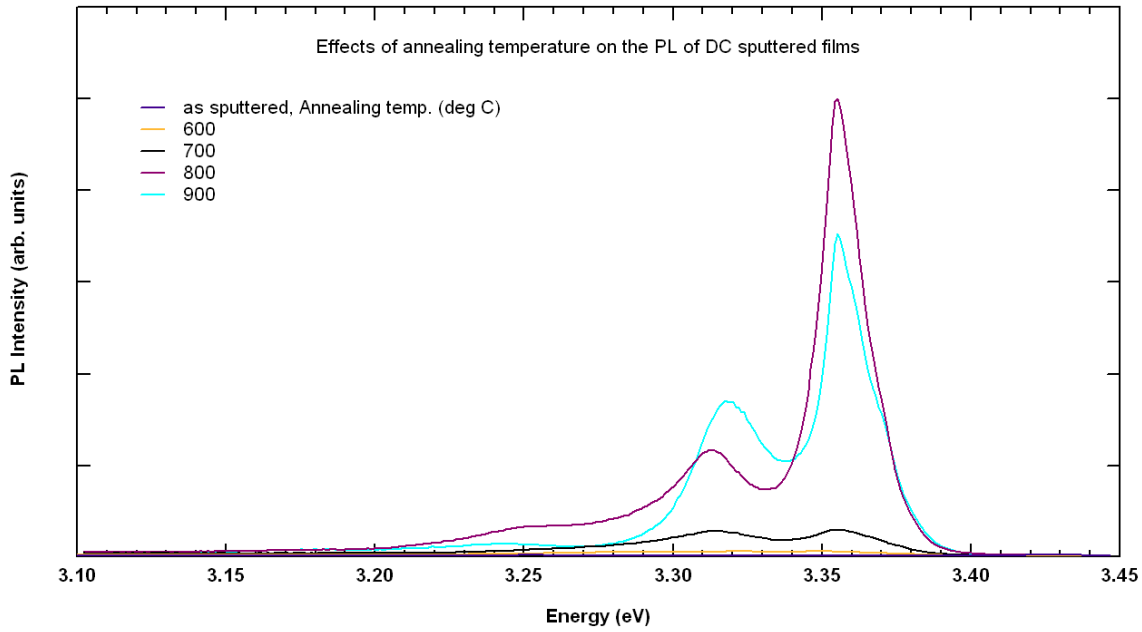

Figure 32: PL spectra (recorded at 4 K) of DC sputtered ZnO at various annealing temperatures. Generally, the strength of the PL increases with higher annealing temperature, however, the PL intensity drops for at 900 °C annealed samples.

For RF sputtered ZnO the PL intensity increased dramatically with higher annealing temperatures, as shown in Figure 33. DC sputtered films produced better quality films, as evident by the narrower line width of the near-band-edge PL.

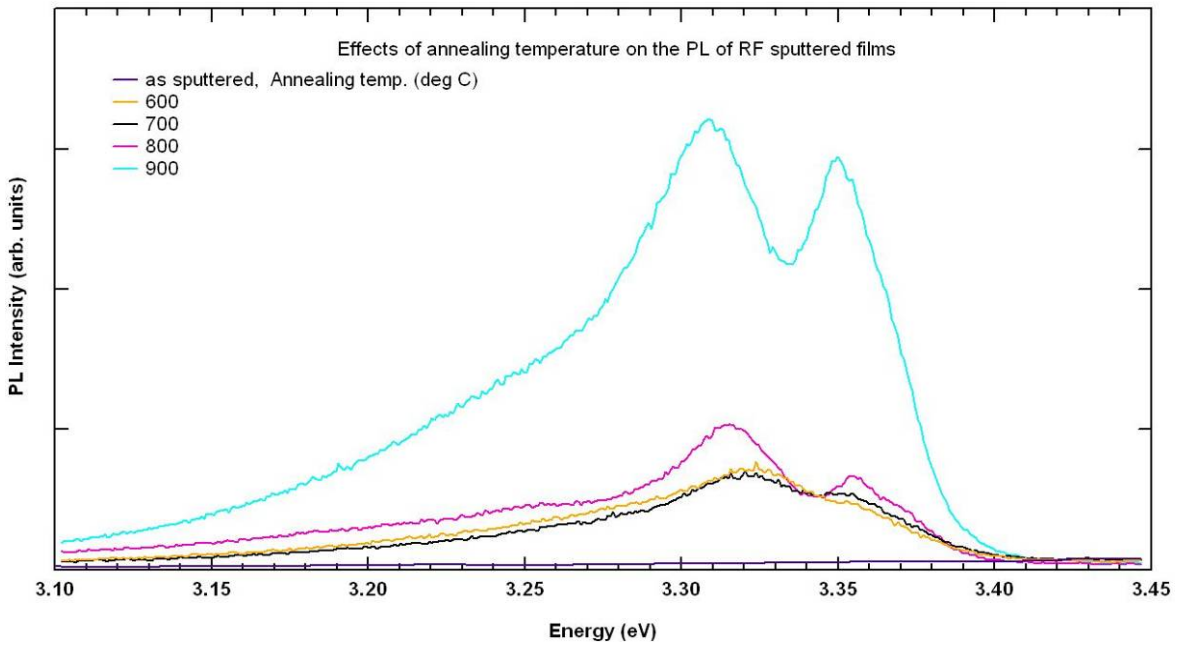

Figure 33: PL spectra (recorded at 4 K) of RF sputtered ZnO at various annealing temperatures. The strength of the PL increases with higher annealing temperatures.

The SEM micrographs (all shown with same magnification) in Figure 34 and Figure 35 show that the grain size for both DC and RF sputtered films increased with annealing temperature. DC sputtered films had a grain size in the range of 100 to 200 nm, while the RF sputtered films had a finer grain size in the range of 20 to 100 nm.

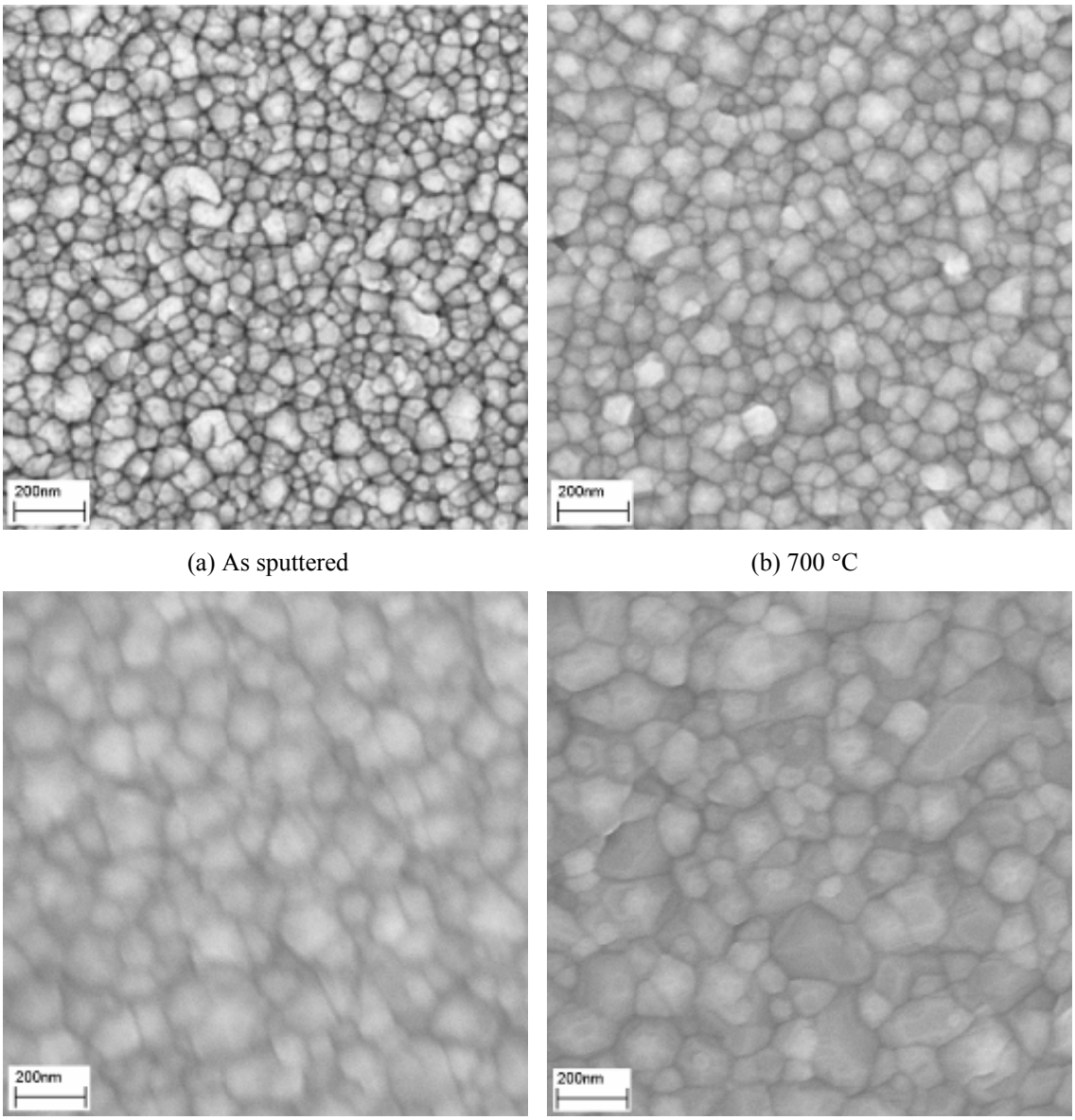

(a) As sputtered (b) 700 °C

(c) 800 °C (d) 900 °C

Figure 34: SEM images of DC sputtered and annealed ZnO. The grain size increased with higher annealing temperatures.

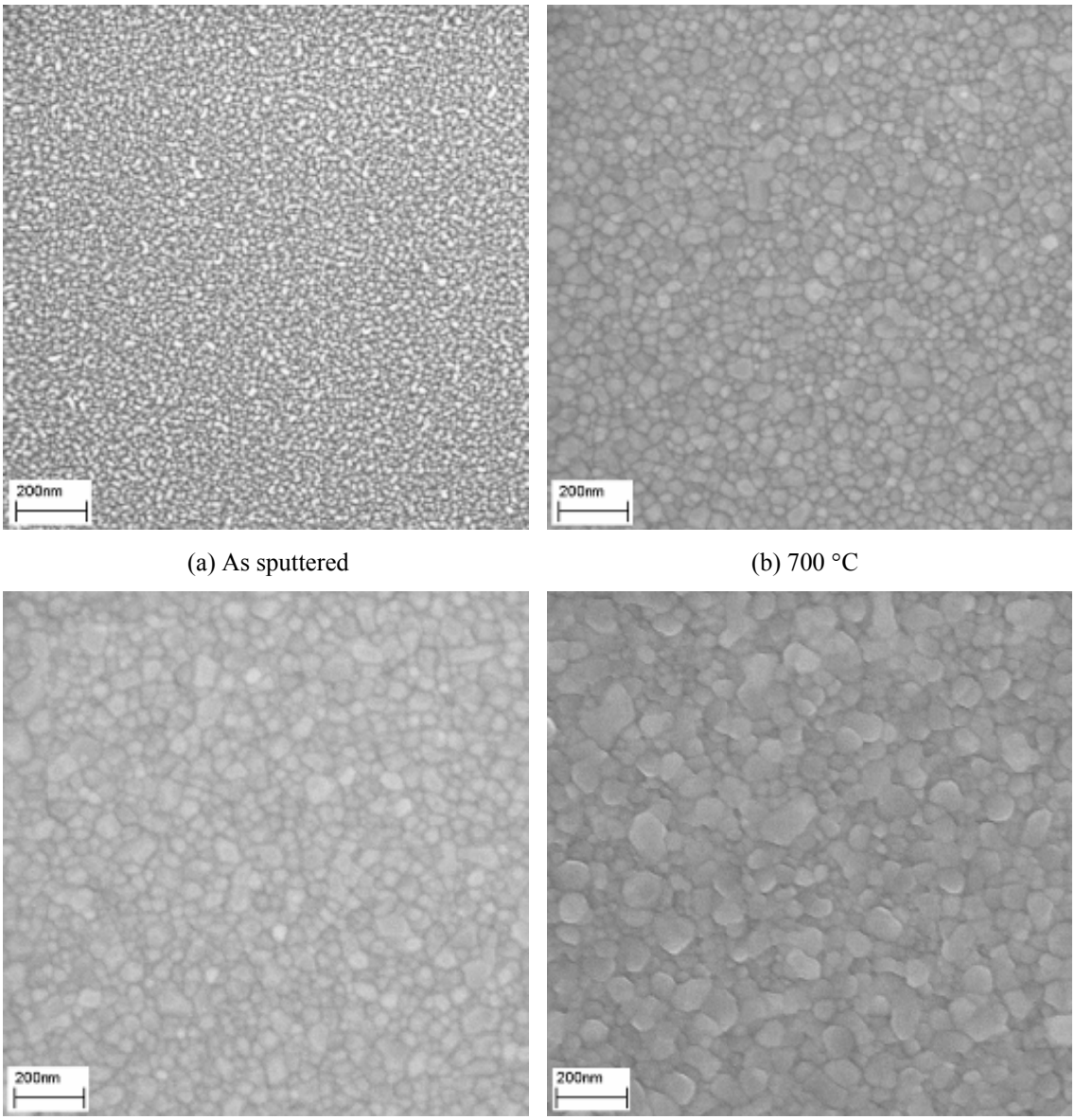

(a) As sputtered (b) 700 °C

(c) 800 °C (d) 900 °C

Figure 35: SEM images of RF sputtered and annealed ZnO. The grain size increased with higher annealing temperatures.

RBS scans of both DC and RF sputtered samples revealed oxygen rich surface layers on all annealed samples (for detailed RBS results refer to Appendix D (samples analysed 01/2005)). It is speculated that atomic oxygen was trapped in the films during sputtering, especially at the interfacial layer between the sputtered ZnO and the substrate [101]. During annealing in N_2 parts of this excess loosely bound O_2 diffused toward the end of the sputtered grains and left the sample on top of the films (also reported in [102].

6.2.2 Dry etching of ZnO films

RIE was performed on selected samples, with a plasma power of 200W (power density = 2.5W/cm^2). CHF_3 was used as etching gas with a flow of 25 sccm, and the etching pressure was kept at 20 mTorr.

For DC and RF sputtered films the XRD results are presented in Figure 36. They show only one peak, which confirmed c-axis oriented polycrystalline growth. Compared with the not etched samples (Figure 31) the peaks were smaller, indicating that the crystal structure had been slightly damaged during the etching process. A slight shift of the peak position for the annealed samples was visible both before and after dry etching and indicated that inherent strain in the ZnO films had been relaxed during annealing and had not been altered during subsequent dry etching.

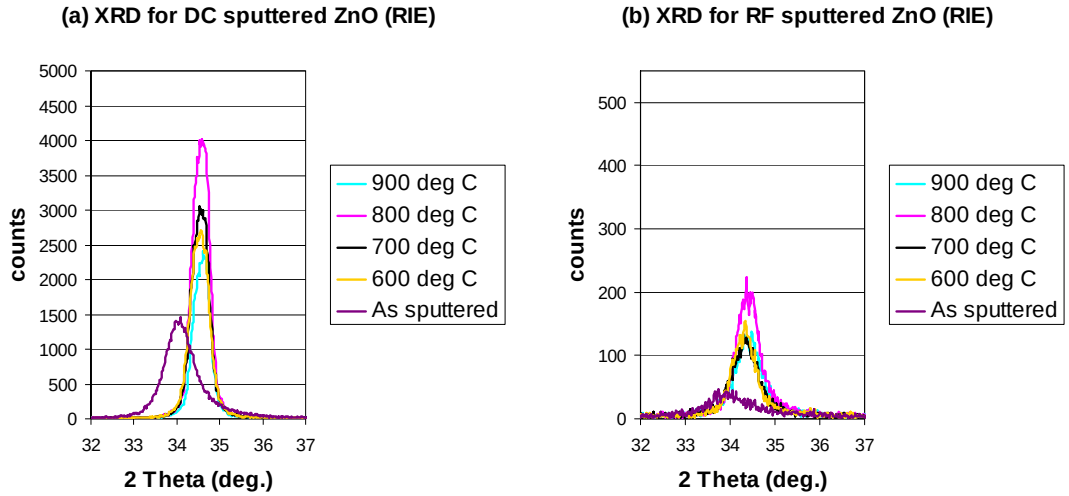

DC sputtered ZnO

Annealing temperature	As sputtered	600 °C	700 °C	800 °C	900 °C
FWHM (002) peak	0.632	0.508	0.486	0.478	0.466
Peak angle (Degrees)	34.08	34.56	34.52	34.58	34.62

RF sputtered ZnO

Annealing temperature	As sputtered	600 °C	700 °C	800 °C	900 °C
FWHM (002) peak	0.644	0.566	0.57	0.522	0.672
Peak angle (Degrees)	33.74	34.34	34.28	34.26	34.48

Figure 36: (a) XRD scan for DC sputtered and dry etched ZnO and (b) for RF sputtered and dry etched ZnO at various annealing temperatures. The tables show the FWHM and peak angle for different annealing temperatures.

Surface scans using SEM and AFM showed no significant change after the RIE process. The surface topology (roughness) for etched and not-etched surfaces was analysed using the AFM. Figure 37 (a) shows images of DC sputtered coatings. The average grain diameter was 200 nm, the grain height 40 nm and surface RMS roughness 75 nm, determined from AFM images. Figure 37 (b) shows images of RF sputtered coatings. The average grain diameter was 50 nm, the grain height 5 nm and surface RMS roughness 7 nm, determined from AFM images.

(a) DC sputtered ZnO (as sputtered) (b) RF sputtered ZnO (as sputtered)

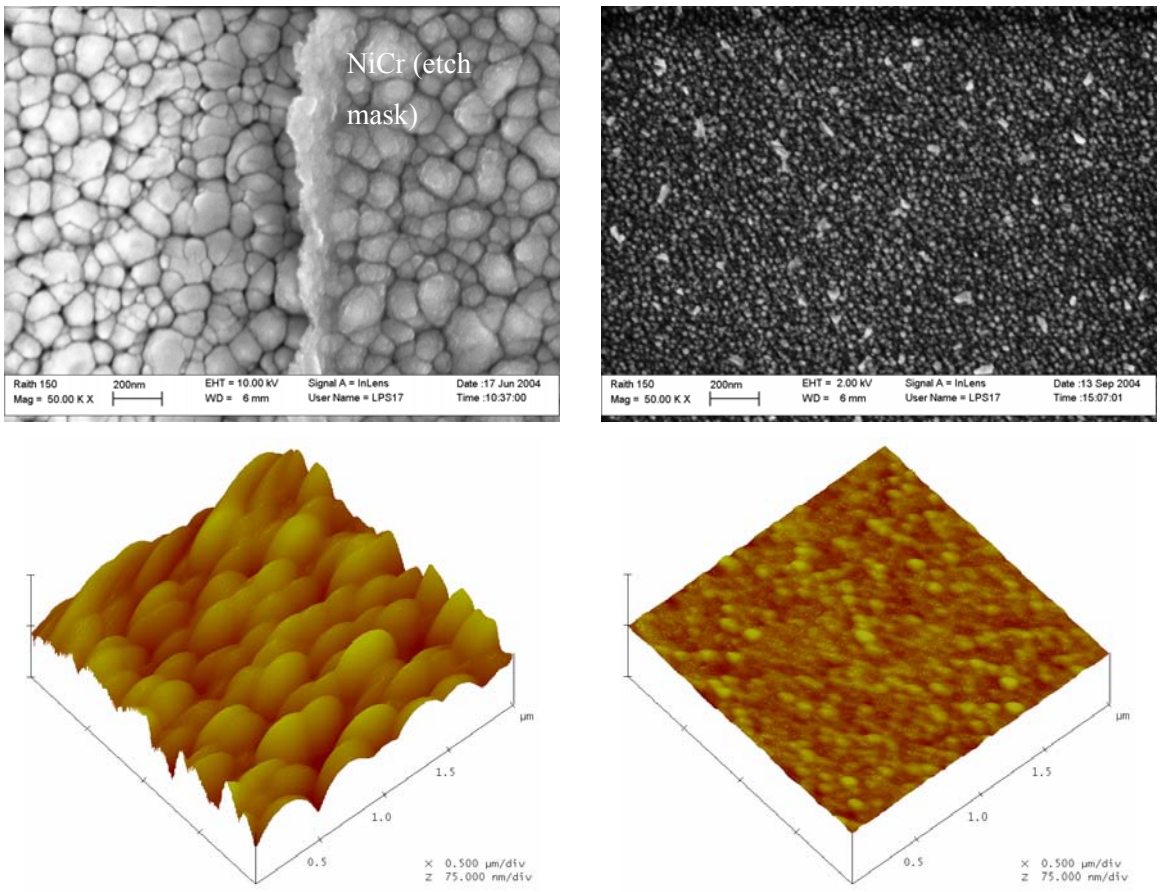

Figure 37: SEM and AFM images show (a) the surface of DC sputtered films, (b) the surface of RF sputtered films.

Figure 38 (a) shows images of DC sputtered coatings after RIE. The average grain diameter was 200 nm, the grain height 26 nm and surface RMS roughness 61 nm, determined from AFM image. Figure 38 (b) shows images of RF sputtered coatings after RIE. The average grain diameter was 50 nm, the grain height 3 nm and surface roughness 11 nm, determined from AFM images.

(a) DC sputtered ZnO (after RIE) (b) RF sputtered ZnO (after RIE)

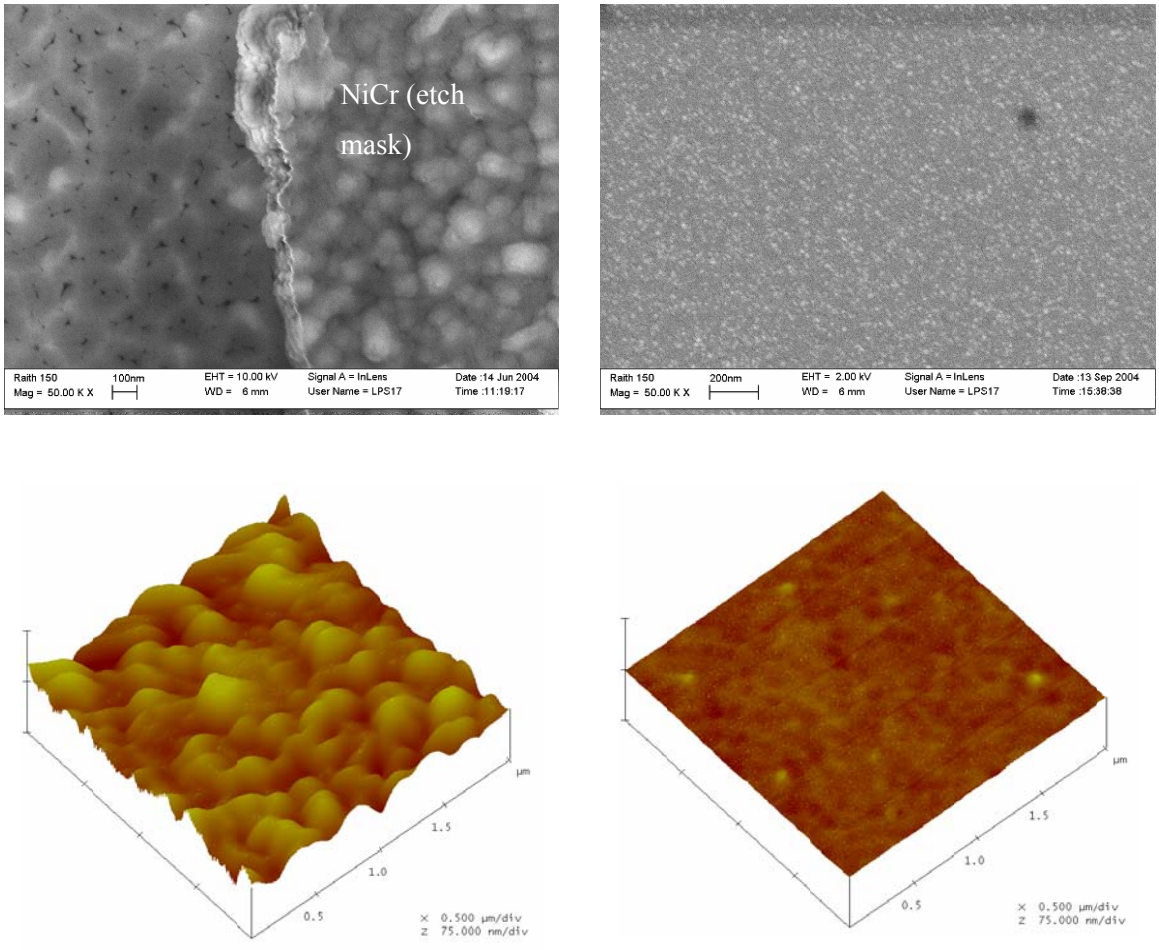

Figure 38: SEM and AFM images show (a) the surface of DC sputtered and dry etched films, (b) the surface of RF sputtered and dry etched films.

For the DC sputtered and dry etched samples the anisotropic etch rate was 5.6 nm/min. The outcome was a film with slightly lower roughness values. For the RF sputtered and dry etched samples the anisotropic etch rate was 5 nm/min. The outcome was a film with slightly higher roughness values.

6.2.2.1 Depth profiling of dry etched samples

A selected number of annealed and dry etched samples were analysed using RBS.

Results for DC sputtered films revealed a carbon (C) rich surface layer on all dry etched samples across all annealing temperatures. In a typical sample, the amount of C in the

45 ± 2 nm thin ZnO surface layer was quantified to 25 ± 2 at.%. The following 235 ± 2 nm thick ZnO layer was measured to be stoichiometric (Zn:O ratio 1:1 ± 0.05).

Dry etching using CHF_3 is considered physical etching, suggesting that C was incorporated in the surface layer originating from the CHF_3 gas. Generally, physical dry etching leads to slight roughing of the surface, which seems to promote the retention of carbon. Also, no undercut (which would point to chemical etching) was evident.

RBS analysis on RF sputtered and dry etched films revealed a similar depleted surface layer with a thickness of 30 ± 2 nm, followed however by a 40 ± 2 nm interface layer of silicon incorporating Zn as an impurity (Zn:Si) = (0.1 ± 0.05 :1.0 ± 0.05). No other elements were traced using a combination of ion beam analysis techniques of RBS, particle induced X-ray emission (PIXE) to probe for heavy elements and nuclear reaction analysis (NRA) to probe for nitrogen. The films had generally a slightly higher roughness after dry etching, which probably aids the retention of carbon.

The dry etching of DC sputtered ZnO led to further increase in PL intensity, as shown in Figure 39, especially for samples previously annealed at 900 °C. Compared to Figure 32, most peaks were enlarged considerably and were slightly shifted towards lower energy bands. This was accompanied by a widening of the PL spectrum, which might indicate the creation of new defect centres.

For RF sputtered ZnO annealed at 900 °C as shown in Figure 40, the PL slightly decreased during dry etching, while the PL for the sample annealed at 800 °C increased considerably. These observations led to speculate that the optimum annealing temperature could lie between 800 °C and 900 °C. This assumption was supported by XRD results as well.

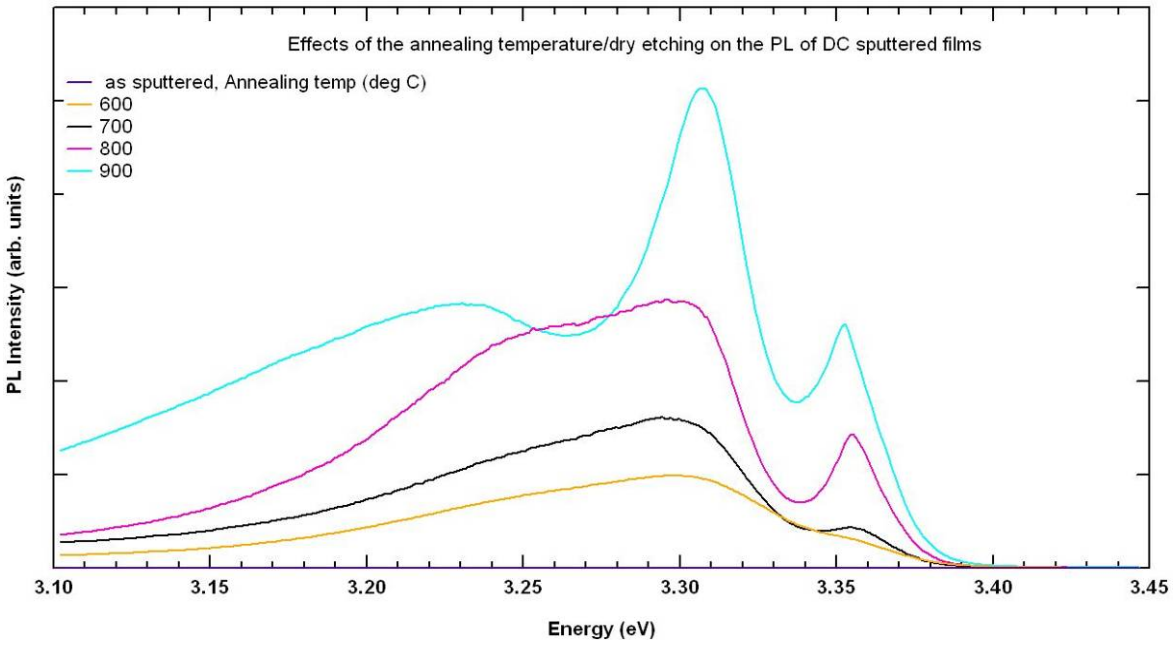

Figure 39: PL spectra (recorded at 4 K) of DC sputtered ZnO (annealed and dry etched). Compared with the not etched samples (shown in Figure 32) the dry etching leads to further increase in PL intensity.

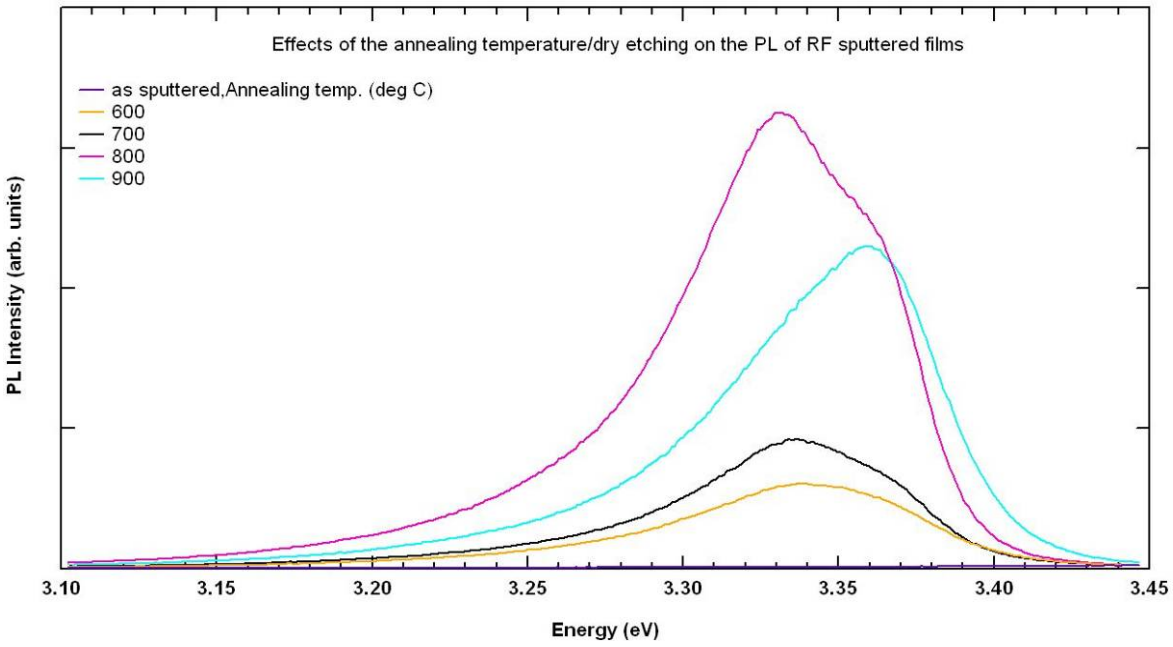

Figure 40: PL spectra (recorded at 4 K) of RF sputtered ZnO (annealed and dry etched). The PL slightly decreases during dry etching, while the PL for the sample annealed at 800 °C increases considerably.

6.2.3 Outcome

ZnO films were deposited using both DC and RF sputtering techniques. RF sputtered films generally had a finer surface and smaller grains. DC sputtered films, however, had a strong piezoelectric response, as determined in Chapter 7.

As reported in [103], DC and RF sputtering are based on quite different phenomena. The DC discharge is based upon the generation of ion-induced secondary electrons at the cathode (target). Therefore, large target voltages are necessary to sustain the plasma because the electron emission increases almost linearly with the ion velocity. On the other hand, the RF plasma is mainly driven by ionisation due to electrons which perform an oscillating motion in the plasma body. The electrons are able to follow the RF frequency of 13.56 MHz while the ions are not, due to their large inertia. This kind of excitation is far more effective compared to the ionisation by non-oscillating secondary electrons and leads to lower target voltages in an RF discharge. As reported in [104] the grain boundaries seem to be influenced by impurities and defects, which in turn are different depending on the kind of sputtering. It is thought that the bigger grain size of DC sputtered ZnO promotes the forming of highly resistive grain boundaries which inhibit charge transfer between individual grains, which is also favourable for piezoelectric properties.

The films were annealed at temperatures of up to 900 °C and dry etched using CHF_3. The annealing led to relaxation of the ZnO structure, bigger grains and increased peaks in XRD measurements as well as a peak-shift due to crystal relaxation. PL response increased dramatically with annealing temperature due to thermal relaxation of the films.

XRD confirmed c-axis oriented growth and a slightly damaged crystal structure, due to RIE. In Figure 41 a comparison is shown between dry etched and not etched films, both for not annealed and for at 800 °C annealed samples. RIE of DC sputtered films led to slightly lower peak count, which indicates slight surface modification. RIE of RF sputtered films led to considerable lower peak count, which indicates more severe surface modification.

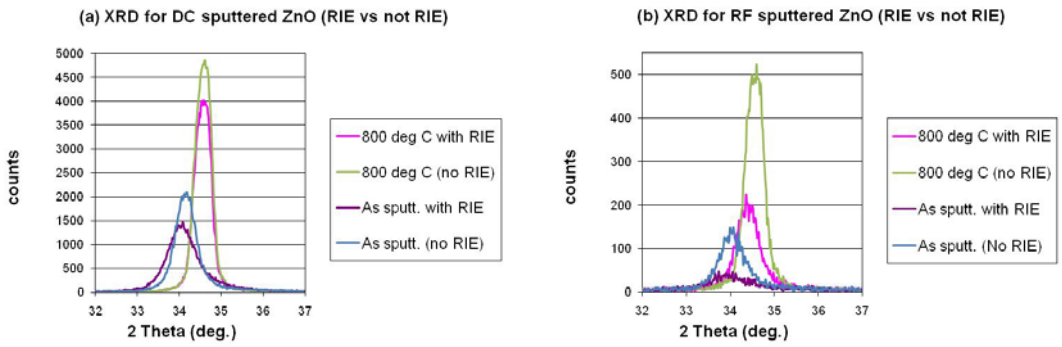

Figure 41: XRD scans (RIE vs not RIE) show a single peak for (a) DC sputtered films and (b) RF sputtered films, for both as sputtered and at 800 °C annealed samples.

Dry etching using CHF_3 led to a slight roughing of the film surface. Therefore the PL response (intensity) was generally further increased, with widening of the spectra after the dry etching process. This indicates the likely creation of new defect centres in the crystal structure.

A carbon rich layer near the surface was traced using RBS, this might have contributed to further widening of the PL spectra, which is also reported in [105, 106].

However, due to the XRD peak dropping at the 900 °C annealing temperature, it was decided to perform further experimental work up to higher annealing temperatures.

6.3 Effects of substrate materials

This section describes and compares the effects of annealing on DC sputtered ZnO. This time films of approx. 300 nm thickness were deposited on four different substrate materials and annealed in N_2 over a wide temperature range of up to 1200 ºC. To ensure consistency, all samples were subject to the same treatment throughout all experiments. Photoluminescence (PL) scans, all recorded at 4 K, on the various films showed a marked difference in temperature behaviour. The results for films deposited on Si, FSG, sapphire and quartz are detailed below.

6.3.1 Annealing results on Si substrate

Samples deposited on silicon and annealed at various temperatures showed enhanced PL with increased annealing temperature (shown in Figure 42), but a lower and very scattered response at 1200 ºC annealing temperature. The PL response showed a sharp peak at around 3.36 eV with phonon replicas at lower energy levels.

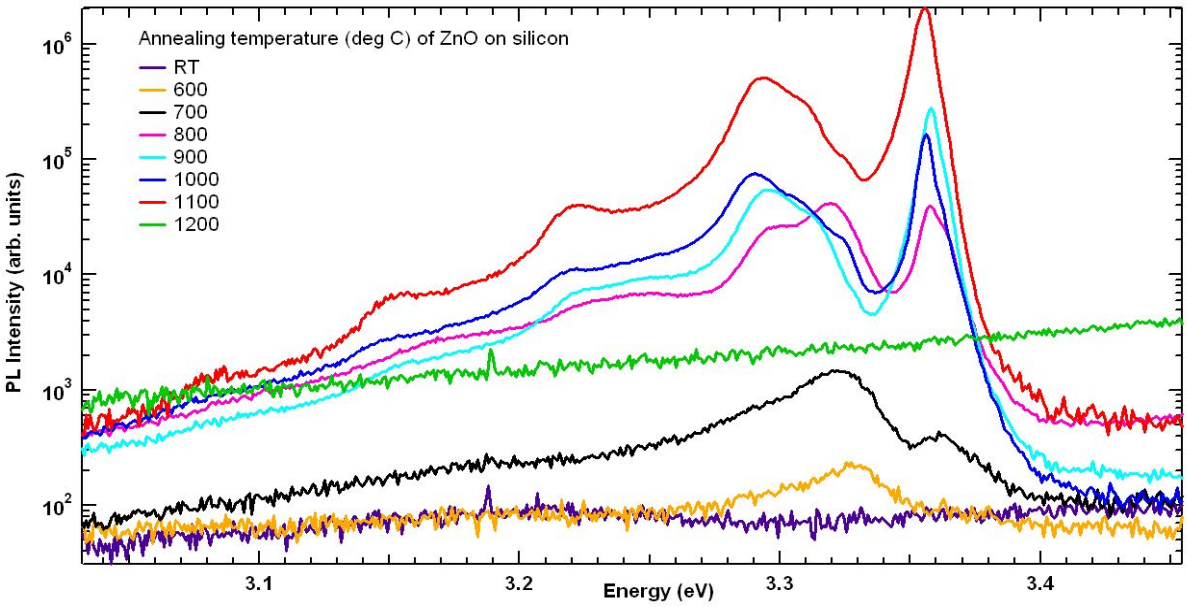

Figure 42: PL response for ZnO deposited on Si for varied annealing temperatures show increasing PL at annealing temperatures up to 1100 ºC. No PL is detected at 1200 ºC annealing temperature.

The SEM images in Figure 43 show the extent of crystal growth due to increase in annealing temperature. At low and medium annealing temperatures, the surface morphology of the ZnO film showed individual grains clearly and the grain size enlarged as the annealing temperature increased. At high annealing temperatures (1100 to 1200 ºC) further crystal modification was apparent (melting) and possibly also mixing with the Si substrate. Some of the annealed films showed cracks, due to a large difference of the thermal expansion coefficient between the films and the substrates.

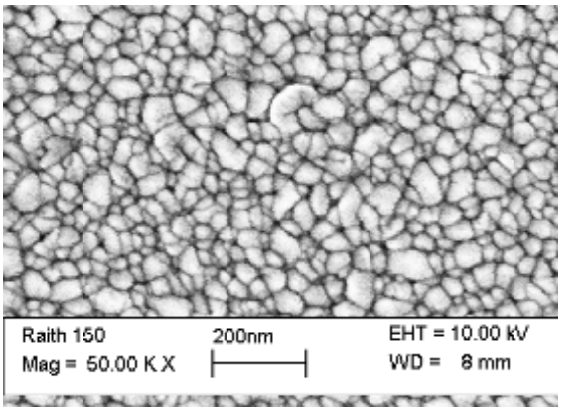

RT

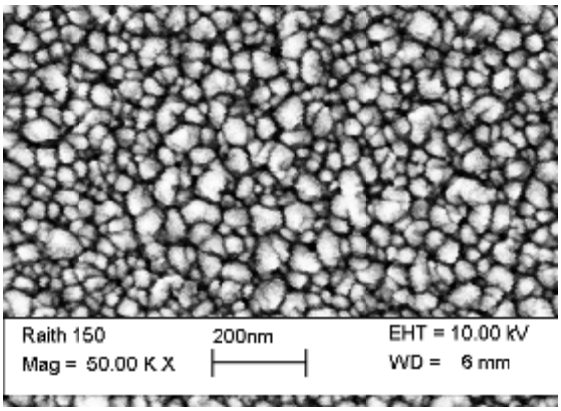

600 °C

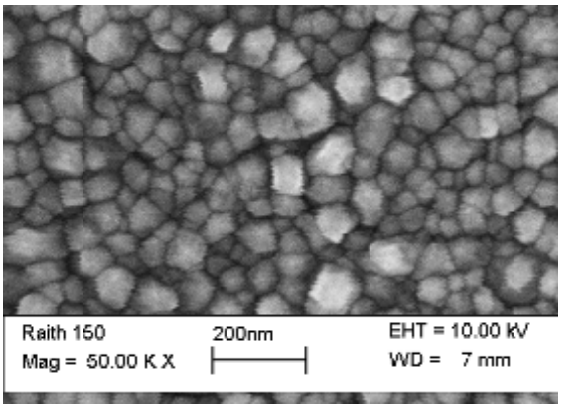

700 °C

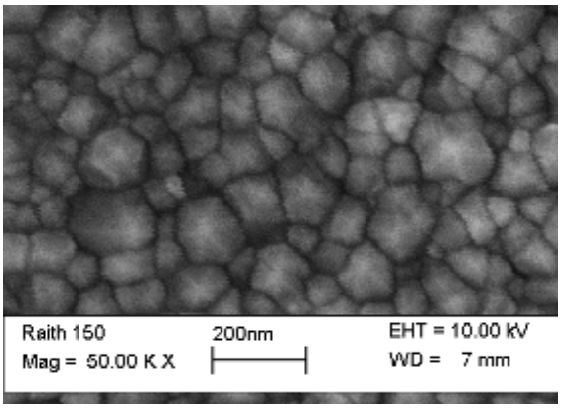

800 °C

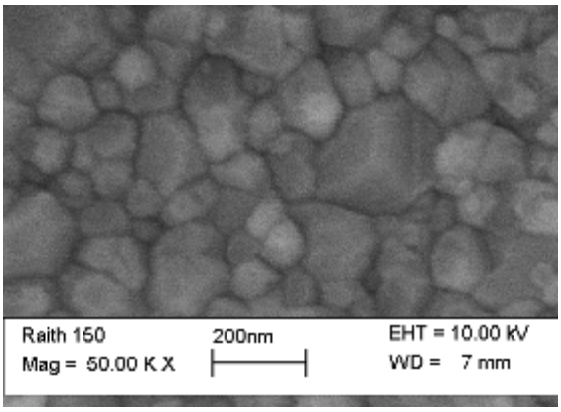

900 °C

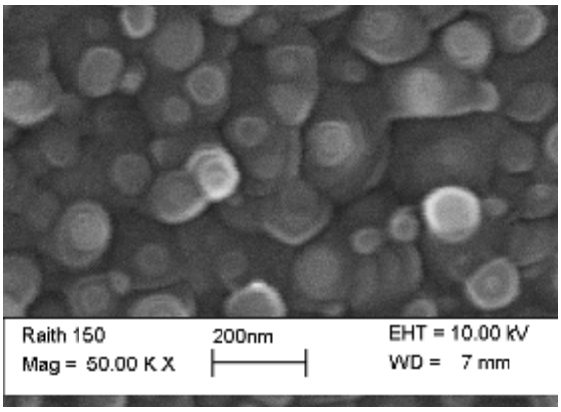

1000 °C

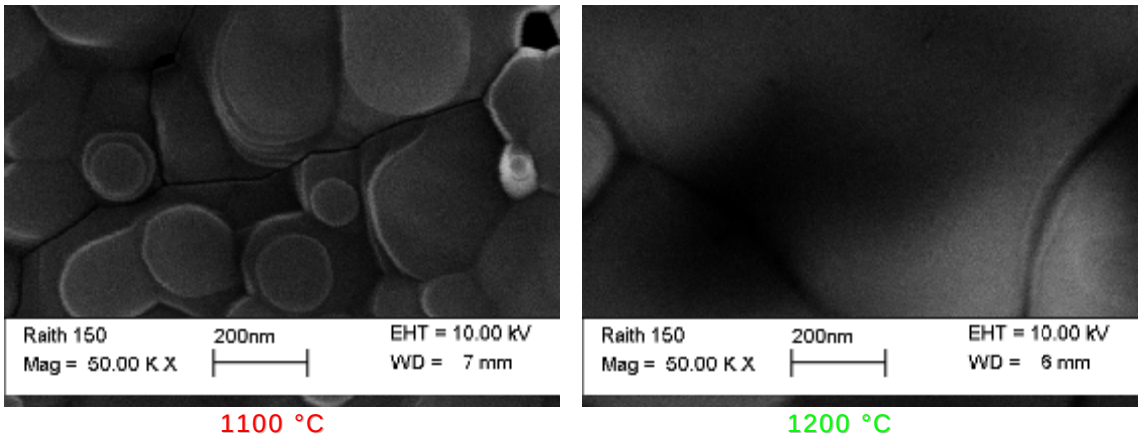

Figure 43: SEM images for annealed ZnO films on Si show increased crystal size with higher annealing temperature.

XRD results of the (002) peak of the same films (shown in Table 4) confirmed a decreasing FWHM due to increased annealing temperatures. This pointed to higher crystal alignment and slightly increasing peak angle for the (002) ZnO peak, due to relaxation of the films.

Figure 44 shows the XRD of this series. The graph for the at 1200 ºC annealed sample shows only a small ZnO peak and a couple of new peaks which are associated with Zn_2SiO_4 (zinc silicate compound), as determined by PDF analysis. Zn_2SiO_4 was the product of the interaction of ZnO with the base substrate (also reported in [107]). At this high temperature the Si substrate is close to its melting point of 1414 °C which allows interdiffusion between the substrate and the ZnO layer.

Annealing temperature	As sputt.	600 ºC	700 ºC	800 ºC	900 ºC	1000 ºC	1100 ºC	1200 ºC
FWHM (002) peak	0.536	0.446	0.516	0.482	0.492	0.402	0.376	N/A
Peak angle (Degrees)	34.08	34.52	34.48	34.6	34.52	34.66	34.66	N/A

Table 4: XRD results for annealed samples on Si show a slight peak shift and a decrease in FWHM with higher annealing temperatures.

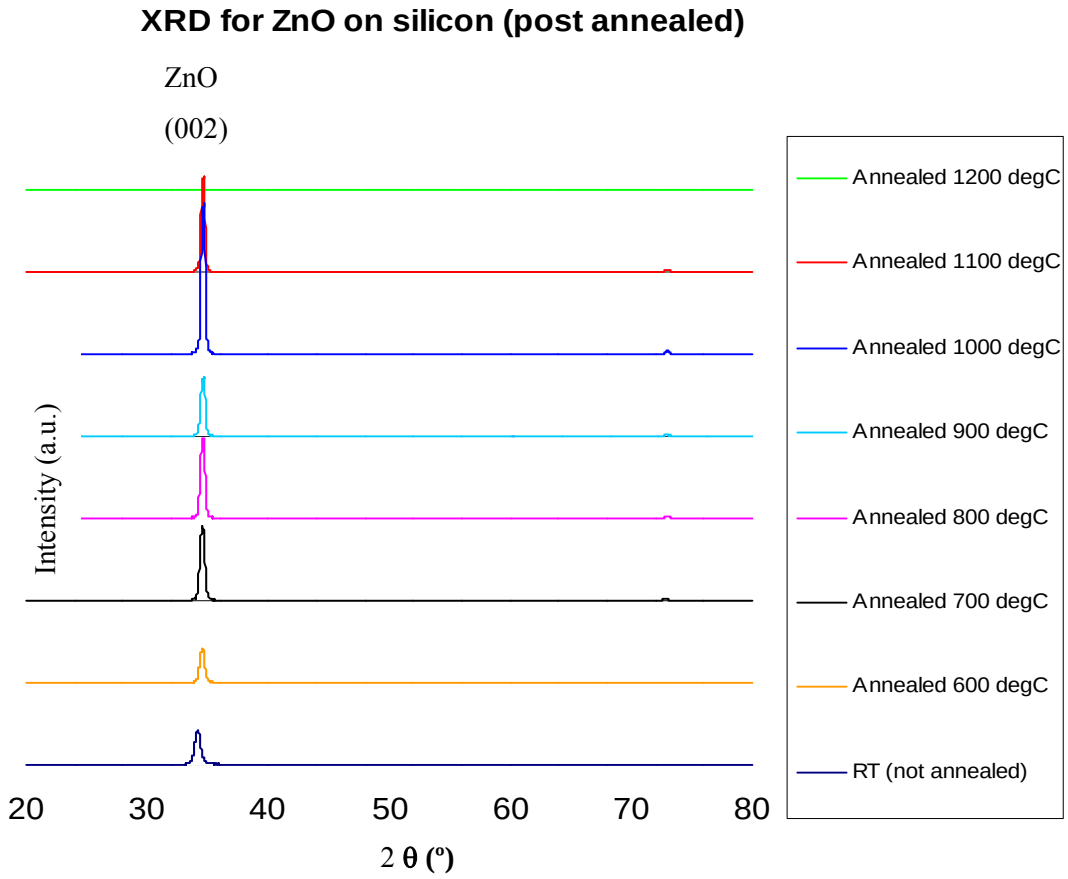

Figure 44: XRD for annealed ZnO films on Si show the highest peak for samples annealed at 1100 ºC and new peaks for samples annealed at 1200 ºC.

6.3.2 Annealing results on sapphire substrate

ZnO deposited on sapphire showed very good PL without post-annealing (shown in Figure 45). The small lattice mismatch between the ZnO and sapphire enables to grow films with higher crystal order. Low temperature annealing at 600 ºC led to a sharp decrease in PL response. In the range of 800 to 900 ºC the PL regained its intensity but dropped again at higher values. At annealing temperatures of 1000 and 1100 ºC a very scattered response was observed.

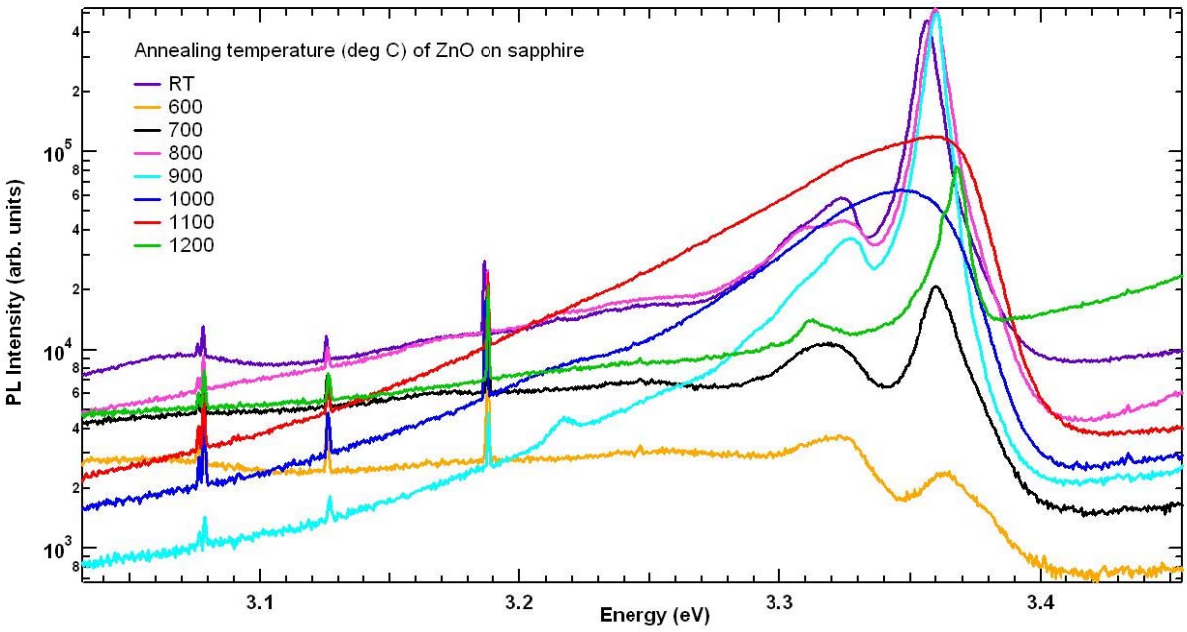

Figure 45: PL response for ZnO deposited on sapphire for varied annealing temperatures show good PL for as-sputtered samples and only a small PL for low annealing temperatures and again high PL for moderate annealing temperatures.

The SEM images in Figure 46 show the extent of crystal modification due to increase in annealing temperature. At low and medium annealing temperatures, the surface morphology of the ZnO film shows a "spaghetti" like structure, at 900 ºC to 1000 ºC the film structure looks very flat and the grain size increases with the annealing temperature. At high annealing temperatures (1100 to 1200 ºC) further crystal modification is apparent (melting). Sapphire has a melting point of 2040 ºC and extremely high chemical stability even at high temperatures. Therefore we do not expect any intermixing between the substrate and the sputtered ZnO.

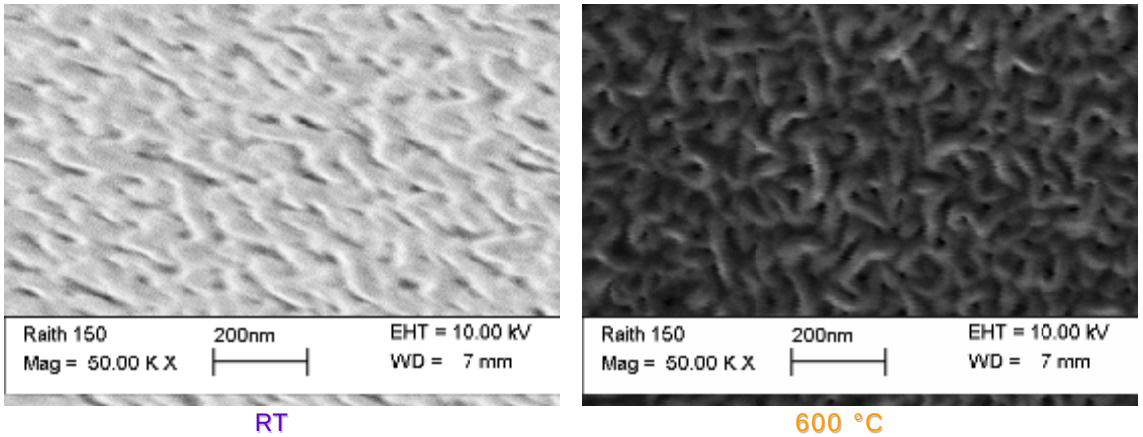

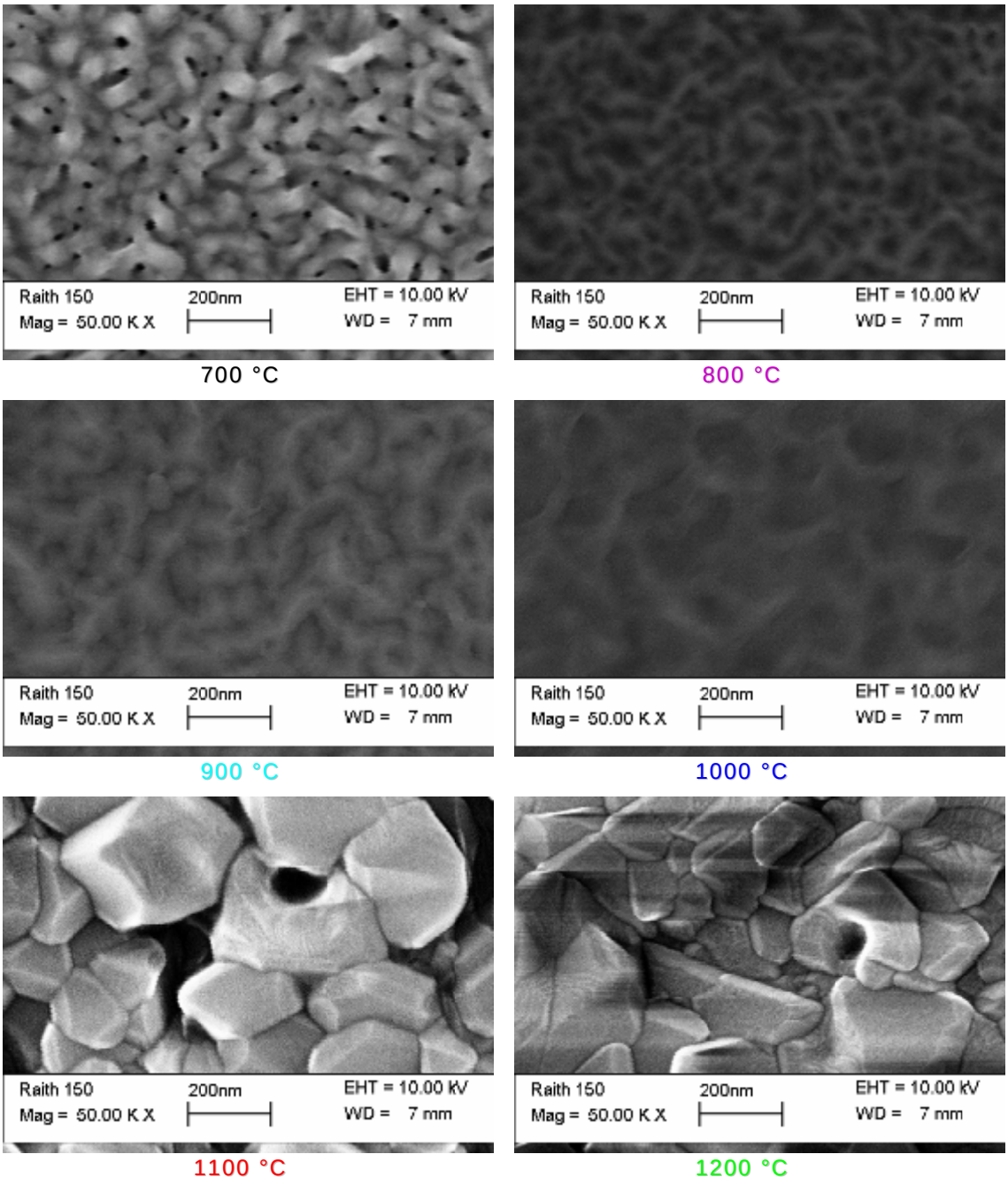

Figure 46: SEM images for annealed ZnO films on sapphire show increased crystal size with higher annealing temperatures.

XRD results of the (002) peak of the same films (shown in Table 5) confirmed a narrow FWHM for as-sputtered films (highly aligned). For films annealed at 600 and 700 ºC the FWHM value was considerably increased, which means that the crystal alignment deteriorated. However, at higher annealing temperatures the FWHM again became narrower.

Figure 47 shows the XRD of this series. The graph for the sample annealed at 1200 ºC shows no ZnO peak, but a couple of new peaks which were associated with $ZnAl_2O_4$, (zinc aluminium oxide), as determined by PDF analysis. $ZnAl_2O_4$ was the product of the interaction of ZnO with the base substrate (Al_2O_3).

Annealing temperature	As sputt.	600 ºC	700 ºC	800 ºC	900 ºC	1000 ºC	1100 ºC	1200 ºC
FWHM (002) peak	0.430	1.090	2.332	0.210	0.250	0.648	0.650	N/A
Peak angle (Degrees)	34.60	34.54	34.56	34.62	34.60	34.54	34.48	N/A

Table 5: XRD results for annealed samples on sapphire show a slight peak shift and changing FWHM with higher annealing temperatures.

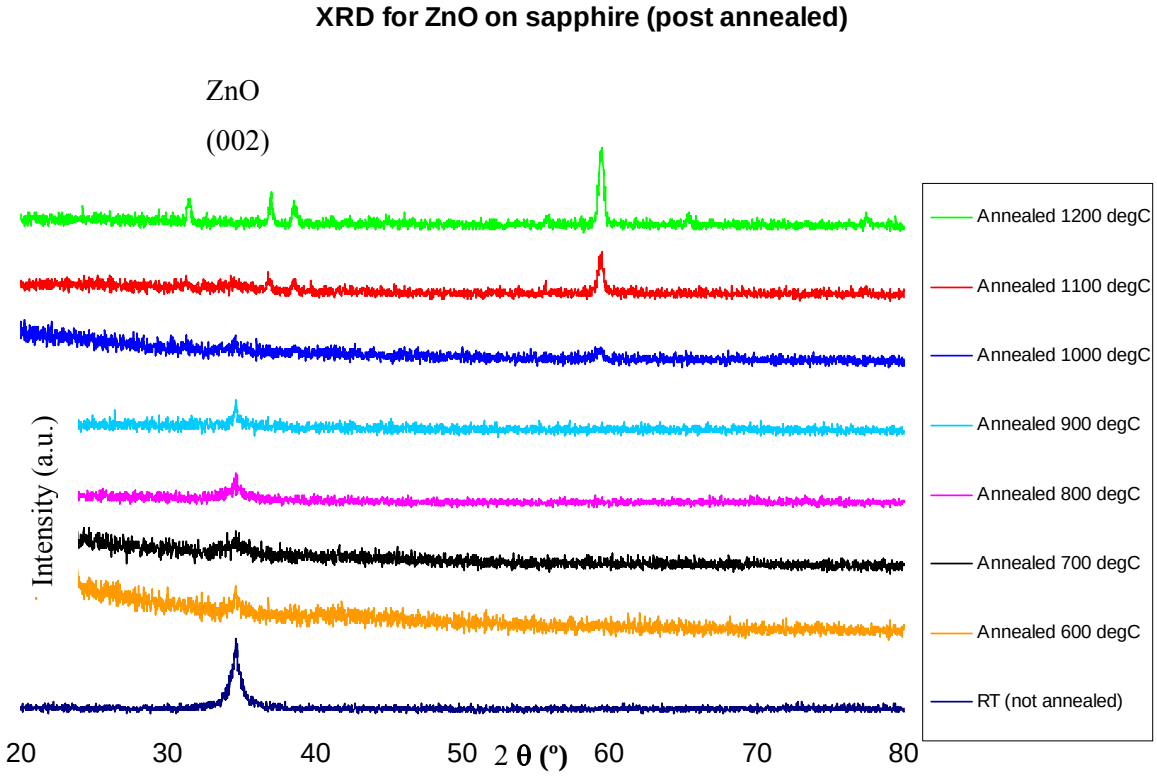

Figure 47: XRD for ZnO films annealed on sapphire show ZnO peaks with variable intensity for not annealed and moderate to medium annealing temperatures and new peaks at 1000 ºC to 1200 ºC annealing temperature.

6.3.3 Annealing results on FSG substrate

Samples deposited on FSG and annealed at various temperatures showed enhanced PL with increased annealing temperature but a lower and very scattered response at 1200 ºC

annealing temperature. As shown in Figure 48, the PL response is generally very broad, with no visible phonon replicas, which is typical for polycrystalline films.

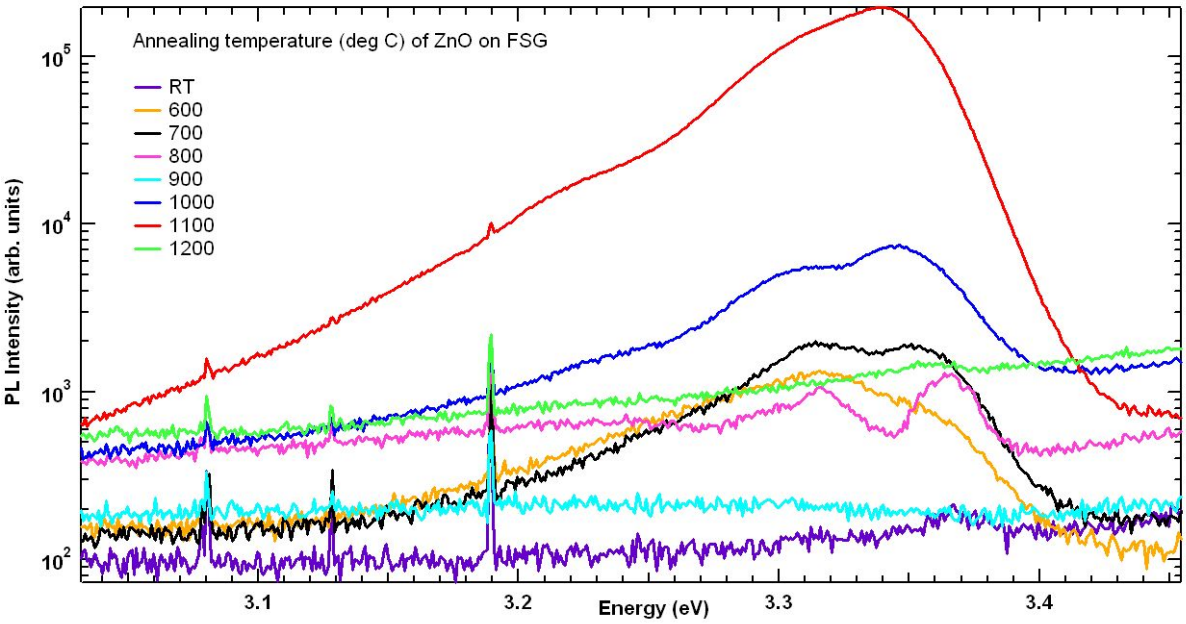

Figure 48: PL response for ZnO deposited on FSG at varied annealing temperatures generally shows very scattered PL which increased with higher annealing temperatures.

The SEM images in Figure 49 show the extent of crystal growth due to increasing annealing temperature. At low and medium annealing temperatures the surface morphology of the ZnO film showed individual grains clearly and the grain size enlarged as the annealing temperature increased. At annealing temperatures of 1100 ºC further crystal modification was apparent, the individual grains coalesced tightly and the grain boundaries became ambiguous. After annealing at 1200 ºC the film changed into a finely grained structure. Most likely a chemical reaction occurred between the base substrate and the ZnO layer. Most of the annealed films showed cracks due to a large difference of the thermal expansion coefficient between the films and the substrates.

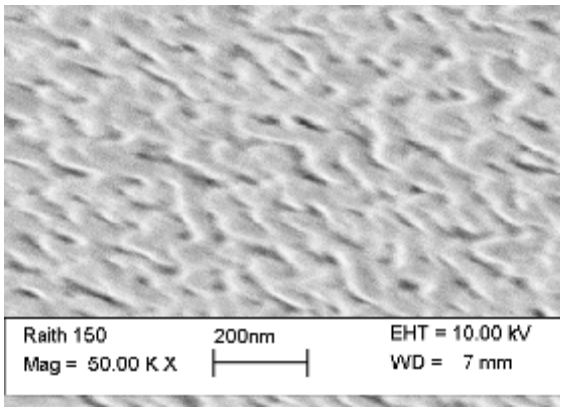

RT

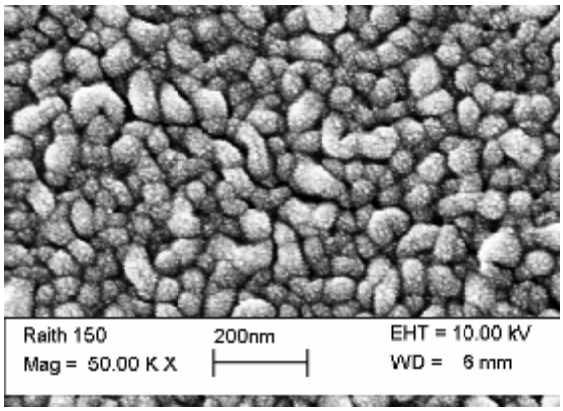

600 °C

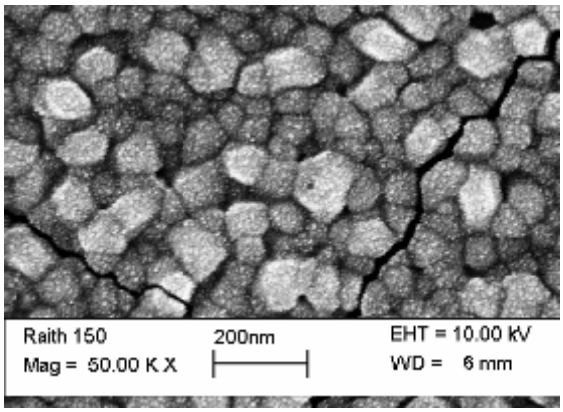

700 °C

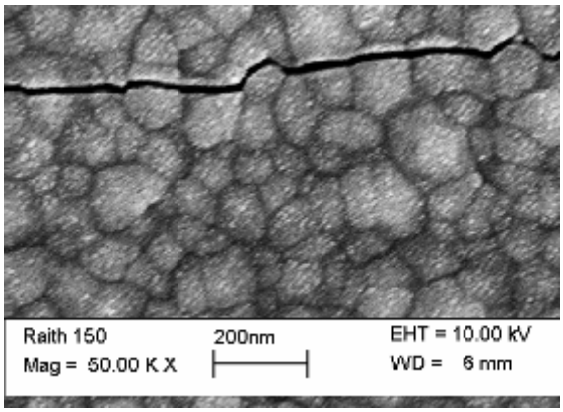

800 °C

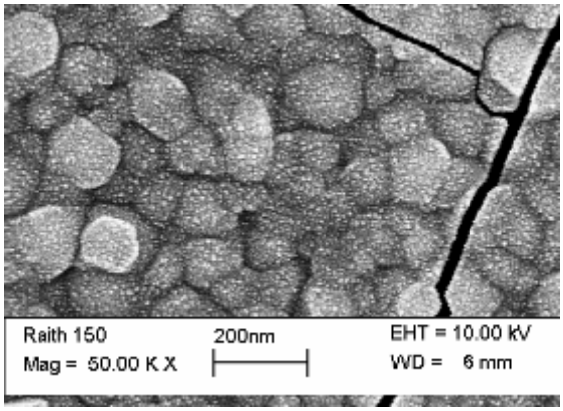

900 °C

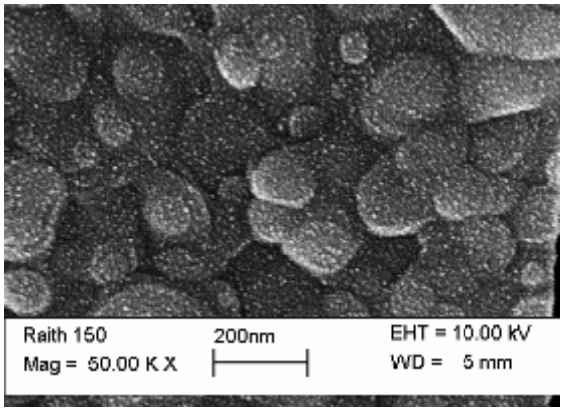

1000 °C

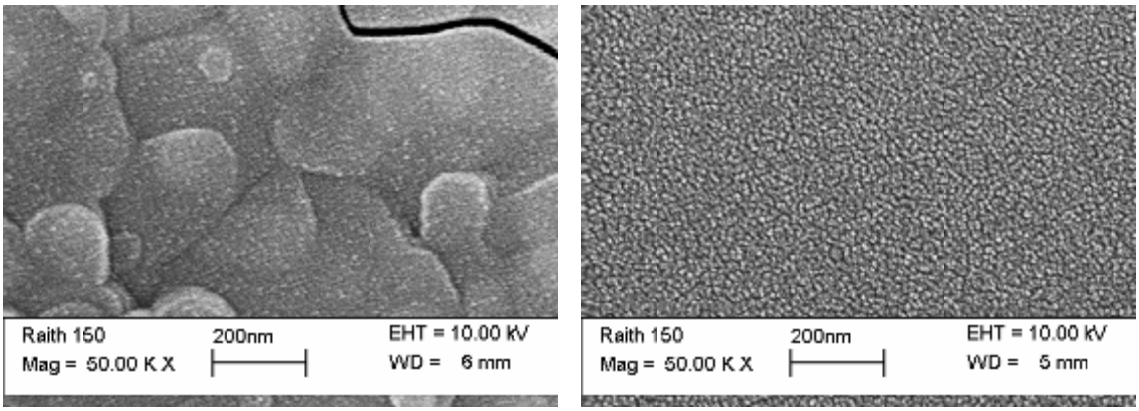

Figure 49: SEM images for annealed ZnO films on FSG show increased crystal size with annealing temperature.

No XRD scans were performed on these samples.

6.3.4 Annealing results on quartz substrate

Samples deposited on quartz and annealed at various temperatures showed enhanced PL with increased annealing temperature, as shown in Figure 50, but a slightly lower response at 1200 ºC annealing temperature. The PL response showed a sharp peak at around 3.36 eV with phonon replicas at lower energy levels.

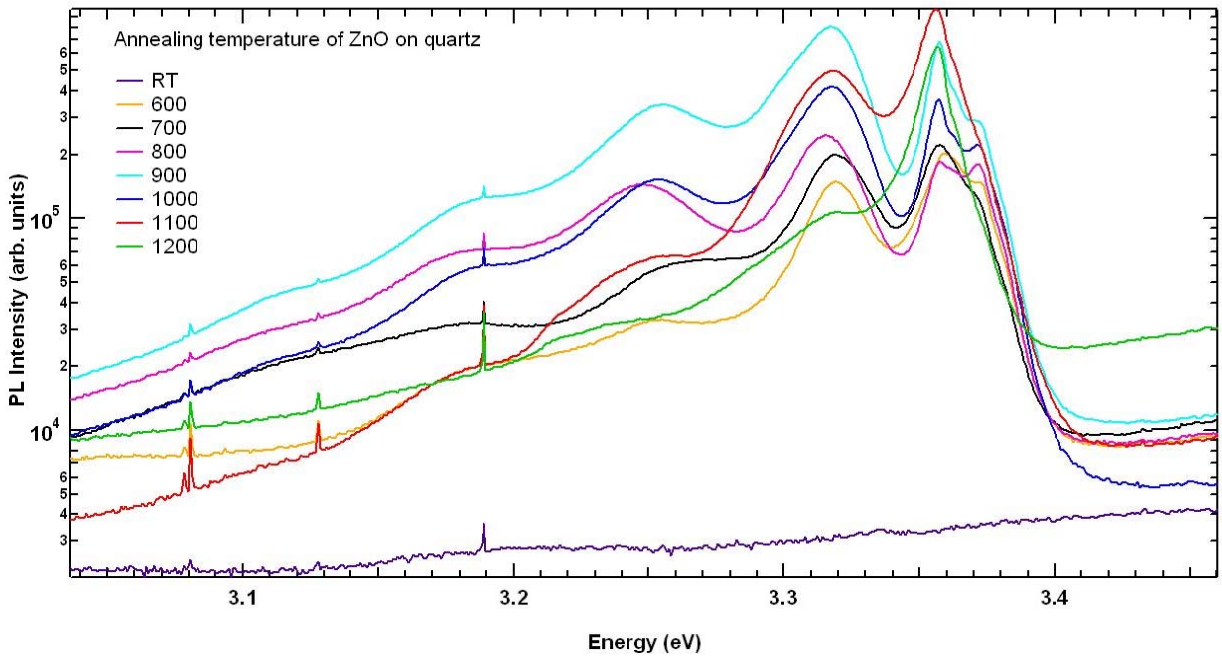

Figure 50: PL response for ZnO deposited on quartz at varied annealing temperatures show increasing PL at annealing temperatures up to 1100 ºC. Good PL is recorded even for samples annealed at 1200 ºC.

The SEM images in Figure 51 show the extent of crystal growth due to increase in annealing temperature. At low and medium annealing temperatures, the surface morphology of the ZnO film showed individual grains clearly and the grain size enlarged as the annealing temperature increased. At high annealing temperatures (1100 to 1200 ºC) further crystal modification (melting) was apparent. Most of the annealed films showed cracks.

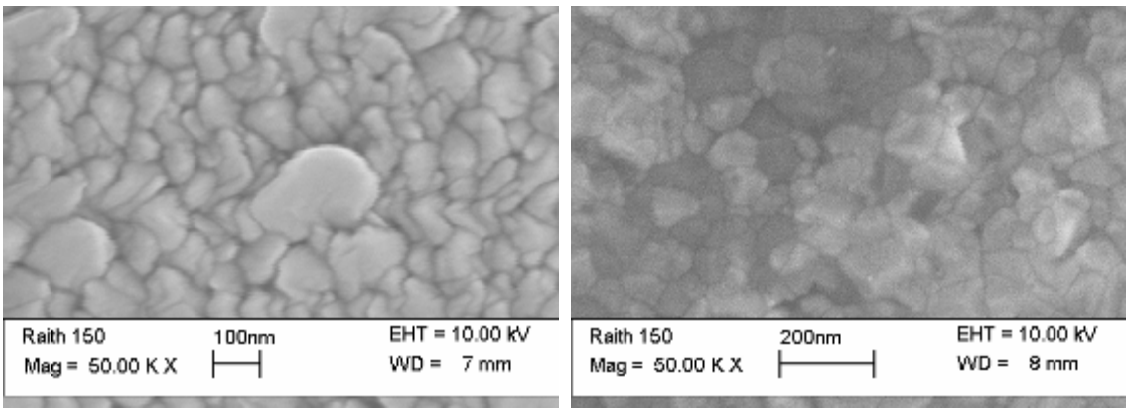

RT 600 °C

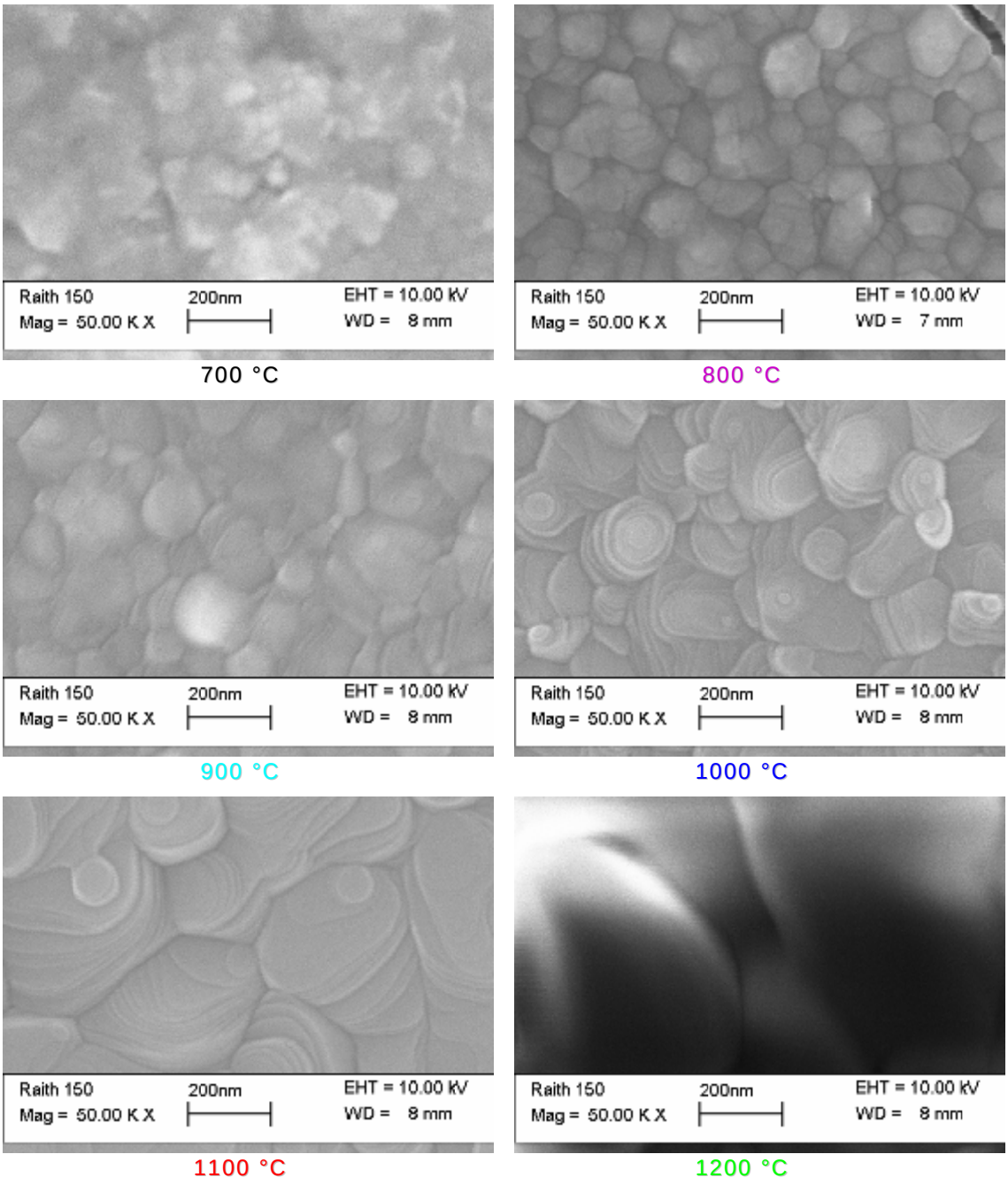

Figure 51: SEM images for annealed ZnO films on quartz show larger crystal size with increasing annealing temperature.

XRD results of the (002) peak of the same films (shown in Table 6) confirmed a decreasing FWHM due to increased annealing temperature. This points to higher crystal alignment and slightly increasing peak angle for the (002) ZnO peak, due to relaxation of the films. Figure 52 shows the XRD of this series. The graph for the sample annealed at 1200 °C shows only a small ZnO peak and a couple of new peaks which are associated with Zn_2SiO_4 (zinc silicate compound), as determined by PDF analysis. Zn_2SiO_4 was the

product of the interaction of ZnO with the base substrate (also reported in [107]). The origin of the small peak at 40 degrees (visible at most annealing temperatures) is unknown since it could not be matched via PDF database.

Annealing temperature	As sputt.	600 ºC	700 ºC	800 ºC	900 ºC	1000 ºC	1100 ºC	1200 ºC
FWHM (002) peak	0.672	0.410	0.350	0.306	0.270	0.370	0.294	N/A
Peak angle (Degrees)	34.24	34.66	34.66	34.649	34.72	34.72	34.72	N/A

Table 6: XRD results for annealed samples on quartz show a slight peak shift and a decrease in FWHM at higher annealing temperatures.

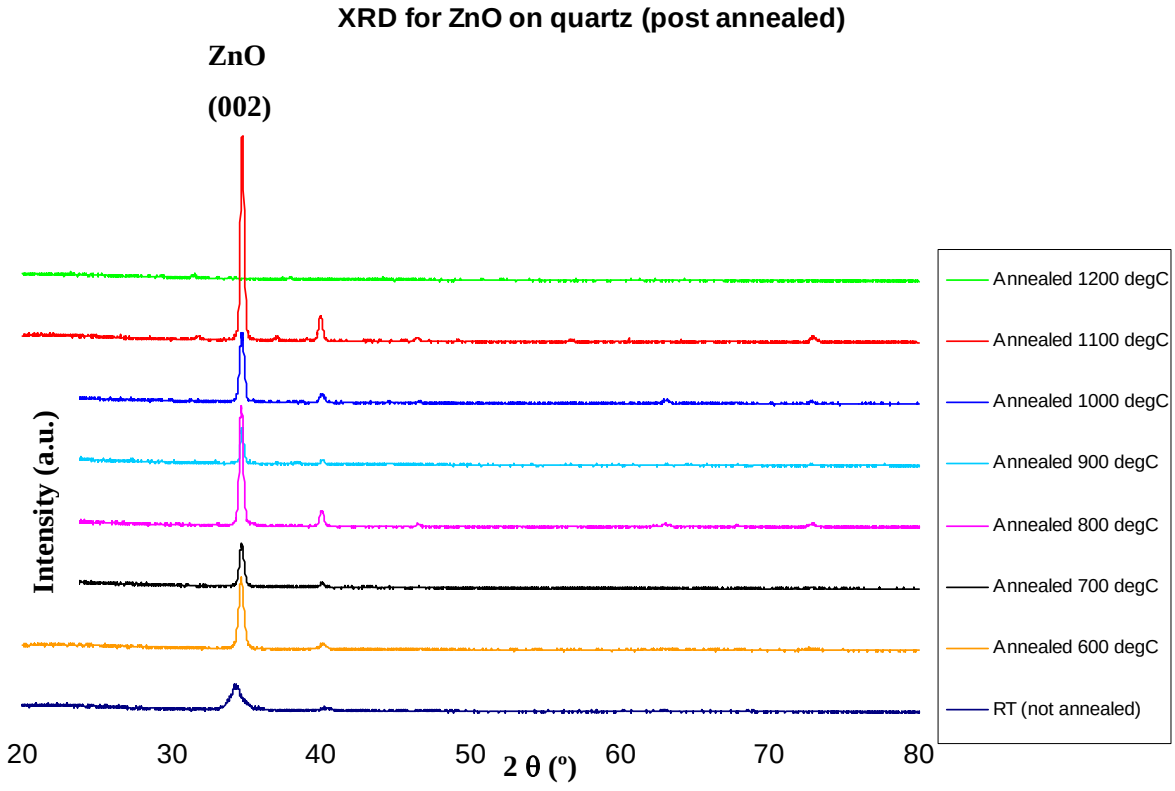

Figure 52: XRD for annealed ZnO films on quartz show the highest ZnO peak for samples annealed at 1100 ºC and no ZnO peak at 1200 ºC annealing temperature.

6.4 Concluding remarks

In summary, Figure 53 shows the PL response for ZnO deposited on Si, sapphire, FSG and quartz substrate against varied annealing temperatures of up to 1200 ºC. ZnO deposited on Si showed good PL for samples annealed in the range from 800 up to

1100 ºC, while ZnO on sapphire showed good PL for as-sputtered samples (RT) and samples annealed above 800 ºC up to 1100 ºC, however, it displayed lower PL values in the temperature range of 600 to 700 ºC. ZnO deposited on FSG showed good PL response only on samples annealed at 1100 ºC. ZnO deposited on quartz showed good PL at 900 ºC and again at 1100 ºC. The highest PL response was obtained from ZnO sputtered on Si substrates, with a post-annealing temperature of 1100 ºC.

A point worth mentioning is that all graphs show local minima for the at 1000 °C annealed samples. It is thought that during annealing at temperatures of up to 900 ºC the intersticials gain just enough energy to realign themselves, so point defect modifications occur. The defect concentration decreases with the increase in grain size. Around the 1000 ºC mark diminishing PL might be caused by O_2 loss at the surface. At even higher temperatures bulk transport happens between substrate and film.

In that regards, a correlation clearly exists between the XRD and PL scans.

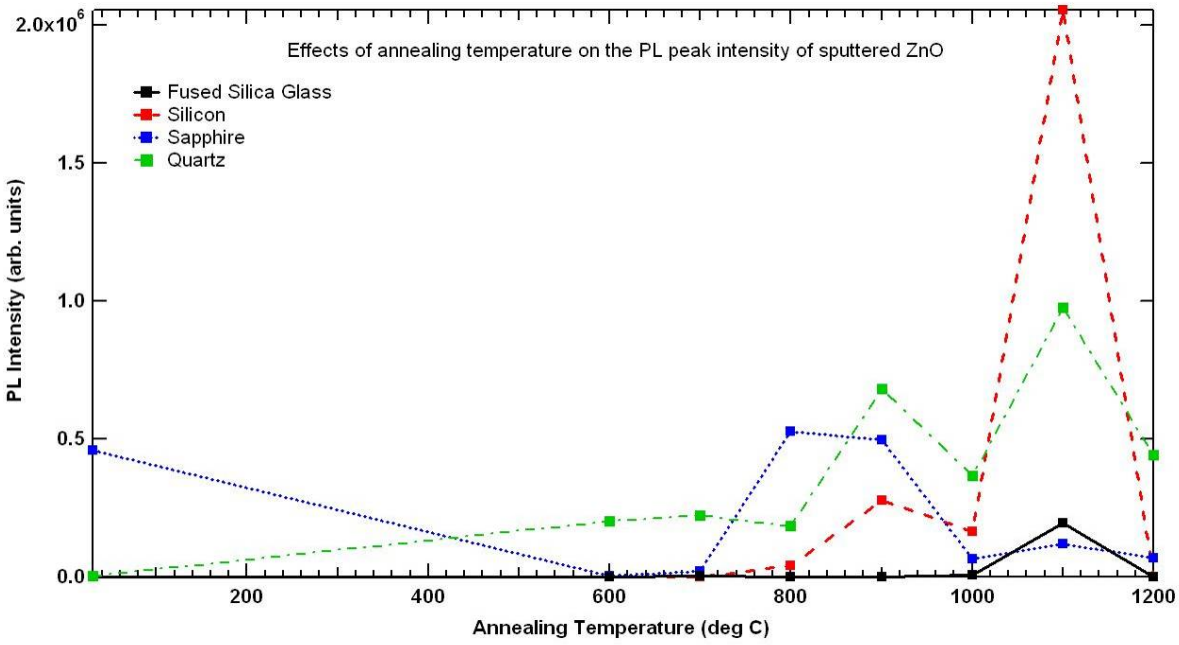

Figure 53: PL response for ZnO deposited on FSG, Si, sapphire and quartz substrate at various annealing temperatures.

Clearly, a number of conditions have to be taken in account in order to achieve coatings with high PL values. Namely the choice of base substrate, the sputtering technique and parameters and post-sputtering treatments such as annealing and dry etching. In our setup

DC sputtered films yield higher PL response than RF sputtered films. As discussed in the next chapter, the best d_{33} values were achieved on DC sputtered films without post-annealing or at 600 °C annealed samples.

As shown on sapphire, substrates with good lattice matching yield high-quality PL response without any post treatment. On all other substrates, the PL response increased dramatically with annealing, especially at high temperatures.

Chapter 7
Determination of piezoelectric properties

7.1 Introduction

ZnO needs to be strongly piezoelectric if it is to be used as base substrate for SAW devices or any other sensing devices that rely on the piezoelectric properties. One way of qualitatively proving piezoelectricity is to fabricate a SAW device on the film in question. This is a labour intensive process and indicates only the presence of piezoelectricity but not its strength and properties. In order to understand the factors that influence the piezoelectric properties and to optimise material properties, it is important to determine the quantitative amount of piezoelectricity on various samples.

Piezoelectric properties can be measured using various techniques, broadly speaking, direct film measurements and indirect film measurements [83]. Direct film measurements are performed using quasi-static measurements (i.e. an applied pressure gives rise to a voltage) or dynamic measurements (i.e. an applied oscillating electrical field gives rise to travelling bulk acoustic waves). Indirect methods rely on measuring related properties, such as surface morphology, internal microstructure, composition or optical and dielectric properties.

The principal performance-determining parameter for piezoelectric materials is called "d_{33}", the piezoelectric coefficient. It indicates the charge per unit force in the polarisation direction of the sample; the electric field and the strain are both along the polarisation axis. "d_{31}" indicates a charge per unit force in the polarisation direction of the sample, but the deflection of interest is that orthogonal to the polarisation axis; the electric field and the strain are orthogonal to each other.

For this work, various methods were employed to determine and quantify piezoelectric properties. Both interferometric measurements using lasers and scanning methods using AFM were employed to determine the d_{33} of various films.

Firstly DC and RF sputtered films were measured in detail using single beam interferometry. The results were ambiguous for DC sputtered samples and no piezoelectricity was detected on the RF sputtered samples. Further checks and investigations were performed to evaluate the set-up. Later, measurements using double beam interferometry were performed on a small number of DC sputtered samples. In

addition to this, selected films were analysed using Piezo-force microscopy (PFM). This technique, which has only become available recently, allows the piezoelectric coefficient of thin films to be determined down to the nanometer scale [41]. PFM is based on Atomic Force Microscopy (AFM) and is used to investigate the converse piezoelectric effect of piezoelectric materials. In collaboration with Nagarayan Valanoor (UNSW) we have mapped the d_{33} of sputtered ZnO for the first time [108]. In this chapter we present results for ZnO sputtered on various substrate materials. We illustrate that sputtered ZnO has a complex domain structures with inversion domains.

7.2 Determination of d_{33} values using single beam interferometry

7.2.1 Sample preparation

The ZnO to be measured was deposited on a conductive substrate (i.e. on highly doped Si substrate or conductive bottom layer), which acts as bottom electrode. For selected samples, post-annealing was performed at this stage, followed by RIE. Afterwards, a conductive/reflective Al layer was deposited on top, which acts as top electrode as well as mirror for the laser beam, refer to Figure 54. The driving voltage was applied between these two electrodes and caused vibrational modes in piezoelectric materials. The laser beam reflected off the sample was modulated by these vibrational modes.

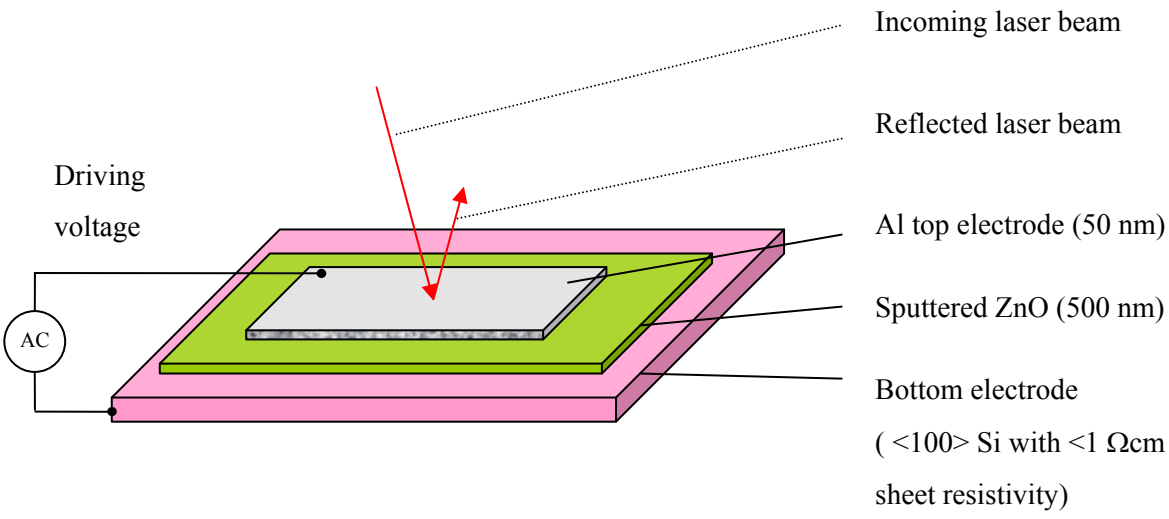

Figure 54: Illustration of prepared sample showing electrodes for excitation.

The samples were bonded to a brass holder using composite glue. Great care was taken to achieve a proper bond to avoid buckling of the samples due to strain induced by piezoelectricity. Finally, both electrodes were connected to the signal generator.

7.2.2 d_{33} Results

Various samples of both DC and RF sputtered ZnO (with and without post-annealing) were analysed. The driving voltage across the two electrodes on the ZnO was varied in the range of 0.5 to 2 Volt and the frequency was kept at 1 kHz. The d_{33} was determined on various points on the samples. A matched stimulus led to a stable output signal with a phase value of around -90 deg.

On DC sputtered samples very high piezoelectric values with d_{33} of up to 100 pm/V were observed. Commonly, d_{33} values of only around 11-17 pm/V for ZnO films are reported in the literature [109]. RF sputtered samples however did not yield any steady piezoelectric response, as indicated by unstable phase values.

Because of the very high readings a range of other tests were performed to ascertain the reliability of the setup and the accuracy of the measurements.

Selected results are listed in Appendix F.

7.2.3 Sanity check: d_{33} of known LiNbO3 sample

To ascertain whether the measuring system behaved as expected, a previously analysed "reference" bulk $LiNbO_3$ sample with both bottom and top electrode was measured repeatedly and at different locations. The averaged result was determined as 6 pm/V, against a theoretical d_{33} of 8.6 pm/V. The values did not depend on the location of the laser beam and the application of an offset voltage did not have an influence on the readings, therefore no electrostriction was detected. The single beam interferometry system performed well on $LiNbO_3$.

7.2.4 Influence of offset voltage on d_{33}

"Ordinary" piezoelectric materials show d_{33} results which are not influenced by an offset voltage. They behave in linear fashion. This was confirmed by Ian Guy, at Macquarie

University in Sydney, an expert in piezo measurements [110]. During our measurements on sputtered ZnO this effect was traced for the first time.

An offset voltage of up to ±10 Volt was applied across the electrodes for a range of measurements. The readings either increased/decreased depending of the polarity of the offset voltage. This phenomenon could be caused by electrostriction. Electrostriction is a parabolic function, while the piezoelectric effect is a linear function. If these two functions are superimposed, the output can either be larger (where both functions are positive), or smaller (where the two functions have a different sign). The lock-in amplifier allows recording the signal for the base frequency of the signal and also the harmonics. The first harmonic contains the electrostrictive signal.

For further details about electrostriction please refer to the introduction in chapter. 2.1.2.

7.2.5 Influence of sample bending and buckling on d_{33} readings

In order to ascertain the influence of sample-buckling on the measured d_{33}, several measurements were performed on one sample at various locations. The averaged values of several measurements on various spots are listed besides Figure 55.

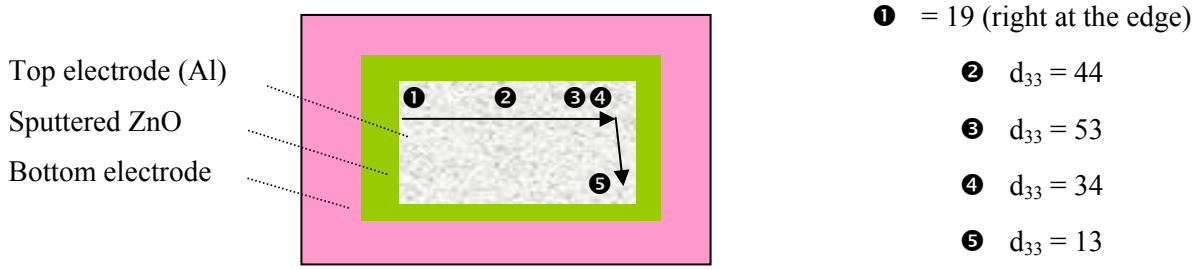

Figure 55: Illustration of measurements locations of test-sample.

Outcome

The d_{33} values vary up to a factor of three within one sample. This considerable effect could have been caused by buckling/warping of the samples.

Clearly, the results are highly variable and therefore have to be treated with caution. Despite these perturbing findings it was decided to analyse further samples in order to establish the possible influence of annealing and dry etching on d_{33}.

Great care was taken to prepare the samples for measuring and everything was kept the same in order to achieve repeatable results.

7.2.6 Influence of annealing temperature and dry etching (RIE) on d_{33}

The d_{33} of a series of samples was measured after annealing at various temperatures, with and without dry etching.

As shown in Figure 56, the piezoelectric values of the measured ZnO films are affected by the annealing temperature.

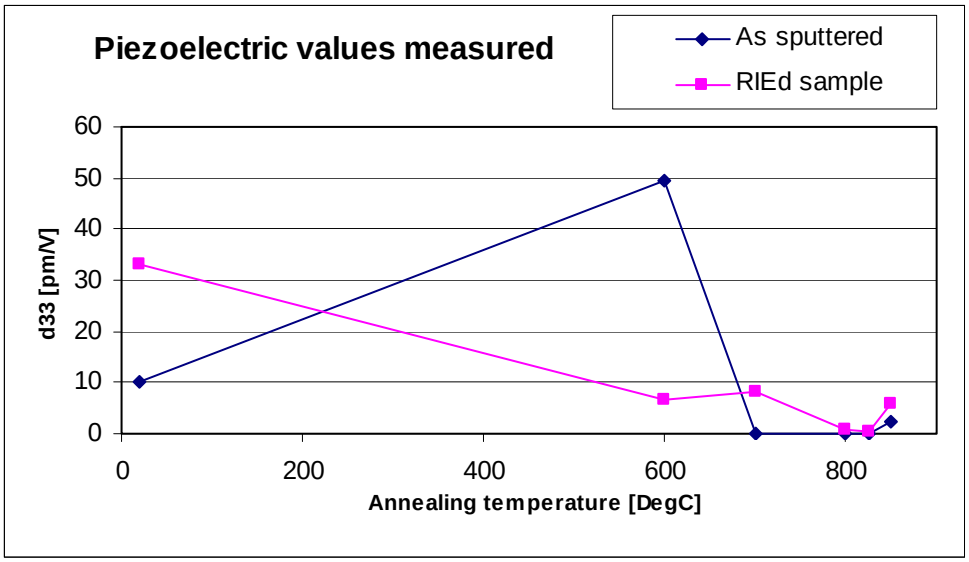

Figure 56: Piezoelectric values measured on annealed / dry etched films.

For DC sputtered samples the d_{33} increased with annealing at 600 °C. Higher annealing temperatures led to diminishing d_{33}.

RIE led to improved d_{33} for as-sputtered samples, but also to diminishing values for samples annealed at 600 °C. However, for the samples annealed at 700 °C with subsequent RIE the d_{33} improved slightly again.

These finding are indicative only, due to the limited accuracy achieved using the single beam interferometry system.

The RIE using CHF_3 as etching gas is considered as physical etching [79]. The result is a slightly damaged crystal surface, which shows up as slightly wider PL response and seems

to enhance the piezoelectricity. For more information about the dry etching process refer to Chapter 6.

7.2.7 Outcome

DC sputtered samples were analysed by using the single beam interferometry instrument and very high d_{33} values of up to 100 pm/V were detected. Therefore, a number of tests were performed which suggested that the results were inflated by sample buckling/bending and also by electrostriction effects. The d_{33} measurements were also strongly dependent on the sampling location, averaged results varied between 13 and 53 pm/V.

The annealing of DC sputtered samples at 600 °C improved d_{33}, but no d_{33} was detected after annealing at higher temperatures. Dry etching of not-annealed samples led to improved d_{33} while dry etching of annealed samples at low annealing temperatures led to weaker d_{33}.

The material to be measured only shows piezoelectricity between bottom and top electrode, as the electric field is generated normal to the surface and between the two electrode areas. Measurements close to the edges of the top electrode show very small displacements, because the electric field is locally distorted. Therefore measurements preferably need to be taken near the centre of the samples (away from the edges). However, if buckling does occur, it tends to occur in the centre of the sample as well.

Due to the discrepancies in the results, additional measurements using a double beam interferometry system were performed. Double beam interferometry [111] only measures thickness changes of samples and automatically deducts the effects of sample bending or buckling.

7.3 Determination of d_{33} using double beam interferometer

7.3.1 Sample preparation

ZnO was DC sputtered on Al bottom electrodes both on double sided polished Si wafers and FSG. Top electrode dots of 0.55 mm diameter consisting of 10 nm thick Cr and 100 nm thick Au were deposited on sputtered ZnO of 500 nm thickness. A back mirror

was deposited on the FSG to allow the laser to reflect off the surface (the Si wafers already had a mirror finish).

7.3.2 d_{33} results

The driving voltage across the ZnO was varied in the range of 0.5 to 5 Volt and the frequency in the range of 1 to 11 kHz. The d_{33} was determined on various points on the samples. A matched stimulus led to a stable output signal and had a low phase angle of 0 to ± 3 deg. The d_{33} was determined in the range of 3.3 to 4.3 pm/V, which is low compared with the results determined using single beam interferometry. The design of the double beam interferometer allows it to automatically cancel out sample buckling/warping. Selected results are listed in Appendix F.

The offset voltage (important to detect electrostrictive phenomena) was fixed at zero due to limitations of the signal generator used. Therefore, electrostriction could not be traced using this setup.

Considering that the measured films were in no way optimised these values look reasonable. As reported in [109] the d_{33} values of optimised ZnO films are around 11-17 pm/V.

After this analysis the samples were again analysed using single beam interferometry. They returned values of 27 pm/V, with perfectly linear response. One explanation of this discrepancy could be that our samples were subject to heavy buckling/bending.

7.4 Determination of d_{33} using piezoelectric force microscopy (PFM)

PFM is a new technique based on AFM that allows the piezoelectric properties of films to be determined down to the nanometre scale, the inherent resolution limit of the AFM.

Scans were performed on as-sputtered and annealed samples deposited on doped Si, glass and sapphire.

7.4.1 ZnO sputtered on Si

Figure 57 is a set of typical images (1 x 1 μm^2) for a ZnO film sputtered on Si at room temperature. Figure 57 (a) shows the topography, (b) the magnitude of the out-of-plane

displacement and (c) the phase image. In Figure 57 (b) (and for the remainder of the PFM images) bright regions indicate those grains, or cluster of grains, with high piezoresponse or d_{33} constant. The film, even over a length scale of 1 μm^2, shows a variety of contrasts implying a spread in the local d_{33} values. A point worth mentioning is that not all regions are vibrating in phase with the applied signal. In Figure 57 (c), there are two types of contrast visible, brown (vibrating in phase) and black (vibrating 180° out-of-phase).

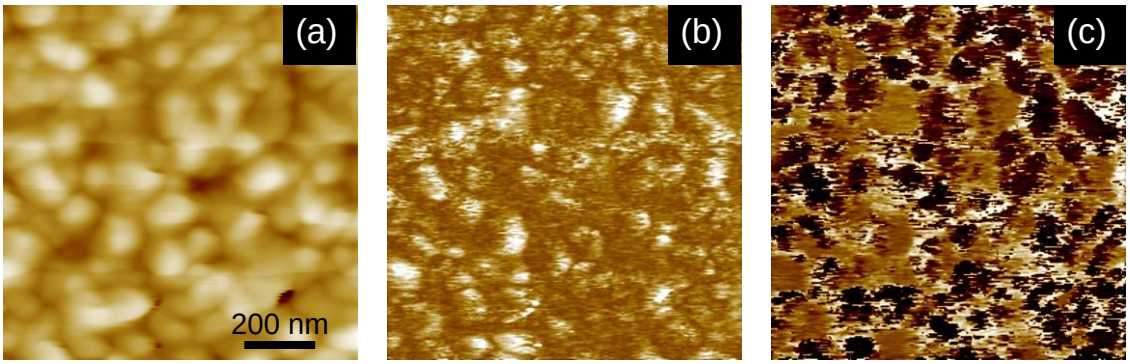

Figure 57: ZnO film sputtered on Si. (a) topography scan, (b) PFM magnitude, (c) phase image.

After seeing these scans the first time, we needed to verify whether the observed contrasts are influenced by topography effects.

7.4.2 Considerations about influence of topography

In order to exclude the influence of topography effects in the PFM results, higher magnification (500 x 500 nm) scans were employed as shown in Figure 58. Again (a) is the topography, while (b) and (c) are PFM magnitude and phase images respectively. Visually it can readily be discerned that the observed phase contrasts are independent of topography. For example, the region marked as "A" in all the images in Figure 58 appears bright in the topography scans, which indicates that it is the top of a crystal. The PFM magnitude for this grain is not very high as indicated by its dark colour in the magnitude image (b); we deduce that grain A is vibrating out-of-phase with the applied signal, as it is also dark in the phase image (c). Position "B" also appears bright in the topography, indicating that it corresponds to a crystal grain, but also appears bright in the PFM magnitude (b) and phase images (c). In comparison, grain C in the top left corner is bright in the topography and magnitude image, but dark in the phase image. Grain "D" is perhaps

most interesting: It appears dark in the topography image (depression). However, the magnitude image in "D" appears bright (high d_{33} magnitude) and the phase image brown (in-phase with the applied signal). Figure 58 (d) shows a cross-section plot along a line that runs through grains A, B and C. The lack of correlated peaks or depressions between topography, PFM magnitude and phase is a strong indication that these images are not convoluted by topography or scanning artefacts.

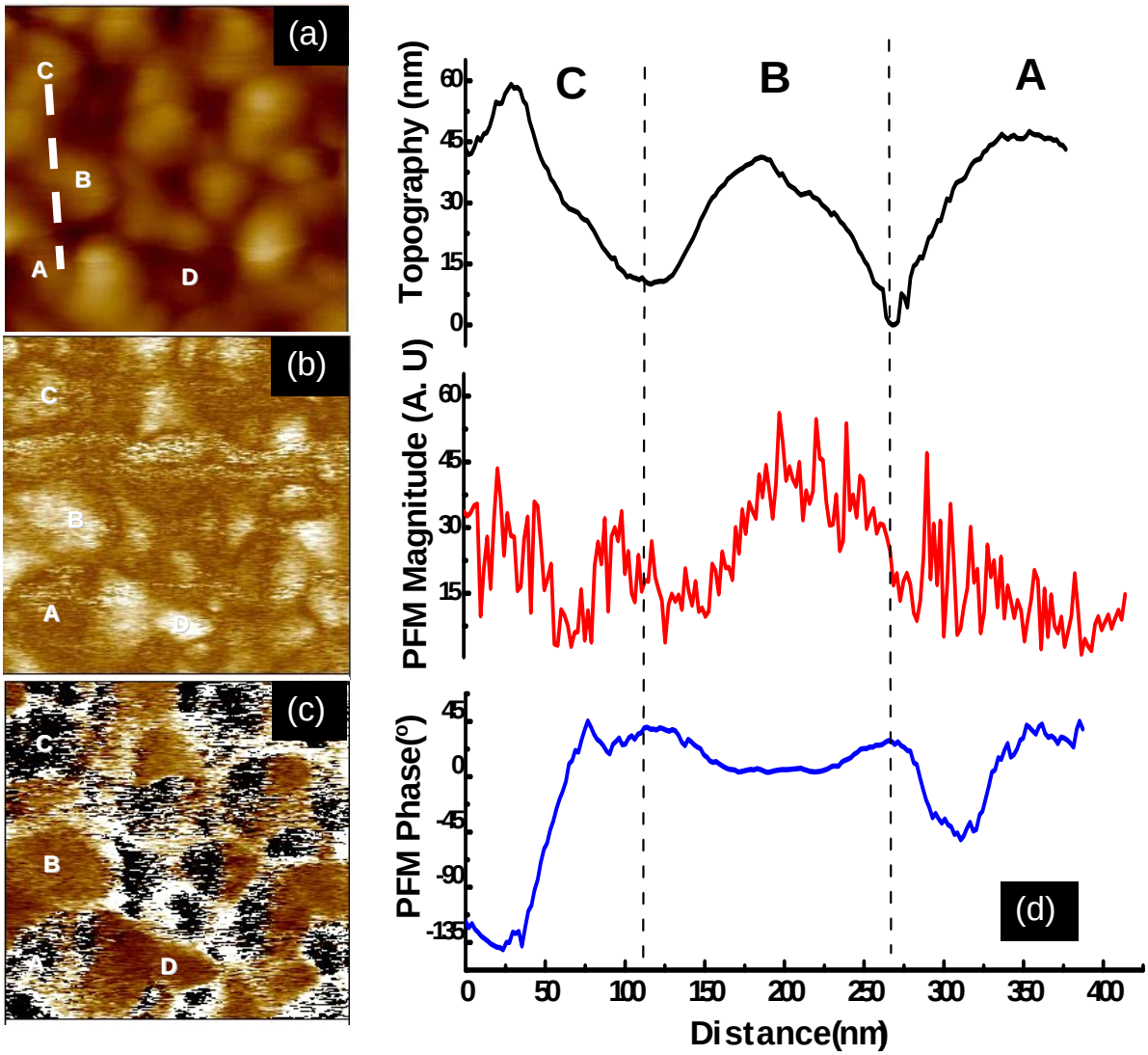

Figure 58: ZnO film sputtered on Si. 500 x 500 nm^2 scans (a) topography scan, (b) PFM magnitude, (c) phase image, (d) line profile of the topography (black), PFM magnitude (red) and PFM phase (blue) along the dashed line indicated in (a). A, B and C in (d) indicate the positions of the grains A, B and C respectively.

In order to compare the piezoelectric response directly with the surface morphology, Figure 59 shows maps of the magnitude (a) and phase (b) of the PFM signal overlaid by a contour map derived from the physical height of the surface. These contours were

obtained from the data of Figure 58 (a). The magnitude and phase correspond to (b) and (c). There was some noise in the signals obtained from the lock-in amplifier and it was noticed that the phase signal could at times quite abruptly swing from +180° to -180°. Both values represent the same physical behaviour, a surface vibration out-of-phase with the driving voltage. In Figure 59 (a) the light regions represent regions of higher d_{33} magnitude, while the grey regions indicate lower magnitude. In (b) the green coloured regions are those where the phase difference between the applied AC signal and the vibration of the ZnO surface is zero, while red coloured regions represent those which vibrate 180° out-of-phase. Several instances can be confirmed where the topography of two regions is the same, as indicated by the contour lines, but the PFM magnitudes as well as the phase are vastly different.

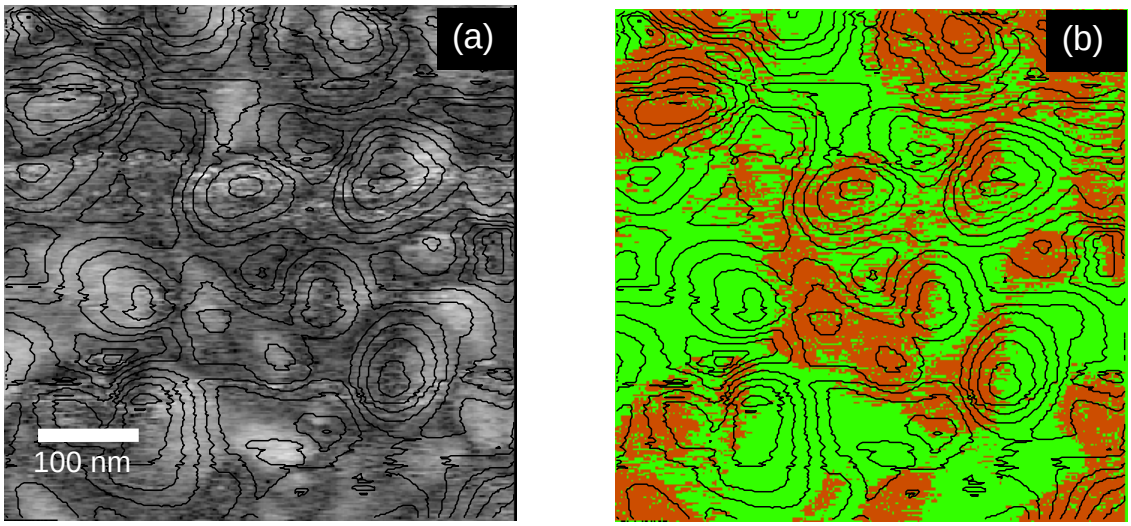

Figure 59: Contour map (derived from the physical height of the surface) overlaid on (a) PFM magnitude and (b) PFM phase (same graph as in Figure 58).

Having confirmed that the PFM observations are not dependent on topography, it is important to understand the meaning of the brown and black regions in the phase image. As mentioned before these two colours in the images represent regions of the surface which are vibrating in-phase (brown) or 180° out-of-phase (black) with respect to the driving voltage. ZnO crystallises in the wurtzite structure and thus does not possess inversion symmetry. This lack of inversion symmetry leads to polarity effects, particularly along the [0001] direction which results in a net dipole moment along this direction. It is possible that these oppositely directed vibrations arose from regions of the sample where the polarisation is also opposed and thus the contrasts observed in our PFM images could

strongly be related to polarity effects. Indeed, there have been recent reports on imaging the polarity of ZnO thin films using electrical scanning probe microscopy techniques. Previously Kelvin Probe Microscopy (KPM) [112, 113] and electric force microscopy [114] have been used to study polarity effects. The electric force microscopy study deduced that the observed contrast was due to a screening charge, induced piezoelectrically by strain at the defect and not due to the intrinsic polarisation of the film. However, Kelvin probe studies deduced that in non-polar ZnO films the contrast observed was due to intrinsic crystal polarisation. Both these observations were based on non-contact AFM techniques, which are highly sensitive to surface charge.

PFM however, is a contact-based technique. Only the first-harmonic of the signal is monitored, the contribution of surface-charge induced effects in the image can be neglected [115]. Moreover, the contrast mechanism in PFM is dominated by the phase of the displacement, which is linked to the surface polarity. Thus we conclude that the brown and black regions show the locations where the polarity is completely opposite to each other, called inversion domains. In comparison, other research showed that PFM images of ZnO single crystals (not shown here) had a uniform phase contrast.

This could explain why thin films show a much poorer d_{33} in comparison to ZnO bulk crystals. It is known from GaN studies that inversion domains are detrimental to performance [116].

7.4.3 ZnO sputtered on glass

In Figure 60 typical PFM images are showed, obtained for ZnO on glass where observations similar to Figure 57 and Figure 58 can be made. Figure 60 (a-c) shows 1×1 μm scans, (d-f) a zoomed 500×500 nm region. In addition, it was found that the films on glass consistently showed higher PFM magnitude than the films on Si. While the exact reasons (chemistry of interfaces, structural quality etc.) are unknown, recent theoretical calculations predict an increase in d_{33} for piezoelectrics deposited on glass due to the high compliance (S_{12}) of glass [84]. One observation in the case of glass is that all regions of high d_{33} are associated with zero phase difference (brown coloured).

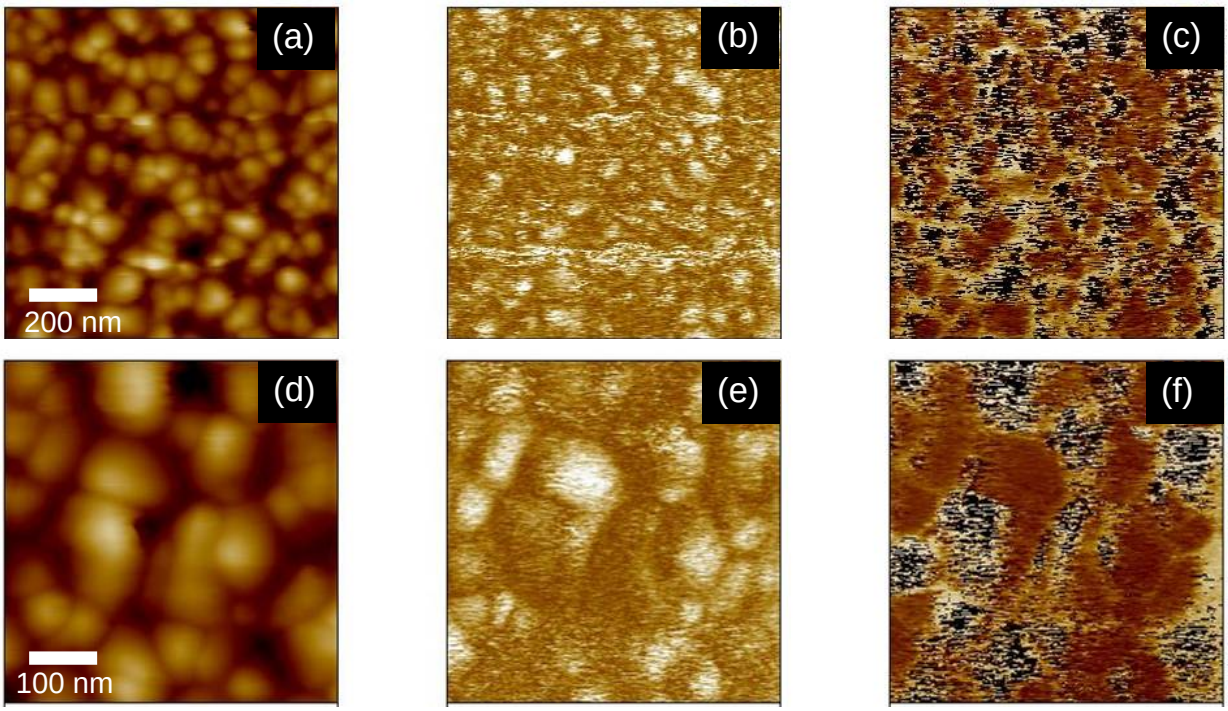

Figure 60: ZnO film sputtered on glass. (a-c) are 1 x 1 μm^2 scans while (d-f) are 500 x 500 nm^2 scans. (a, d) topography scan, (b, e) PFM magnitude, (c, f) PFM phase image.

Annealing of these films leads to improved d_{33} response, however the inversion domains are unaffected. After annealing, the regions of strong piezoresponse in the films are all correlated to domains that are out-of-phase with the applied signal.

7.4.4 ZnO sputtered on sapphire

Figure 61 shows the PFM images of ZnO deposited on sapphire. Similar to Figure 60, (a, d) represent topography, (b, e) the PFM magnitude and (c, f) the PFM phase. Figure 61 (a-c) are 1× 1 μm^2 scans while (d-f) are zoomed 500 × 500 nm^2 scans of the region inside the dashed square in Figure 61 (b). The PFM response of the ZnO films deposited on sapphire is quite different to films deposited on FSG and Si substrate. The regions rendering as white in (c, f) are vibrating +180° out-of-phase.

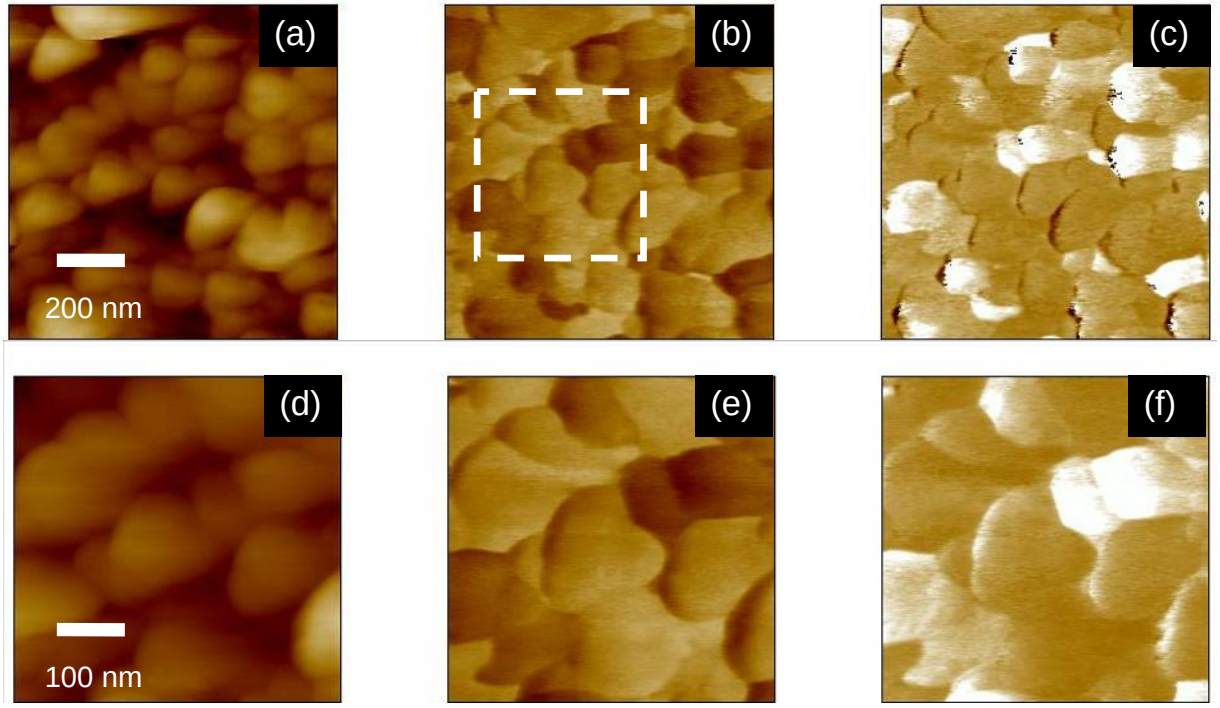

Figure 61: PFM images of ZnO deposited on sapphire. (a-c) are 1 x 1 μm2 scans while (d-e) are 500 x 500 nm2 scans from the area delimited by the frame in (b). (a, d) topography scan, (b, e) PFM magnitude, (c, f) phase image.

It is found that all these grains which appear white in the phase image show up quite dark in the PFM magnitude plots (Figure 61 (b, e)). This indicates a much lower d_{33} response, similar to the films deposited on glass substrates. Those grains that appear brown (i.e. zero phase difference) have larger d_{33} magnitudes.

In an attempt to improve the d_{33} response, the ZnO films were annealed at various temperatures. It was found that the films on silicon and sapphire did not adhere very well after the annealing procedure and hence could yield ambiguous results. However the films on glass were intact and indeed showed significant enhancement and improvement. Figure 62 is a typical set of high-magnification topography, magnitude and phase images 500 x 500 nm^2 taken after an anneal carried out at 600^{o}C. It is virtually impossible to compare the exact same regions before and after annealing; however, to ensure a rigorous comparison, the imaging conditions such as scan size, tip vibration signal etc. were kept identical. Both Figure 60 (d-f) and Figure 62 (a-c) were acquired under these identical conditions and the images before and after annealing have the same contrast scales. After annealing the topography is smoother and the PFM intensity has also increased. In addition, all regions with high d_{33} are uniformly black, which is opposite to the as-grown

case. High-resolution images were recorded to investigate the nature of the domains with the opposite phase and their correlation to grain boundaries. Figure 62 (d) and (e) shows 160 x 160 nm^2 PFM images. Cross-section analysis (not shown here) across Figure 62 (e) shows that the domain inversion takes place in a very sharp manner, the width of the inversion wall is only approx. 1.5 nm. To explain why the inversion domain widths are so narrow, it is necessary to understand the origins of such domains. According to the structure model based high-resolution transmission electron microscopy (HRTEM) [117], inversion domains in (000*l*) ZnO films are created when a (000*c*) region is stacked right against a $(000\bar{c})$ due to a planar defect. These planar defects are no more than a 1 or 2 lattice constant wide and are in fact regions where the crystal symmetry is inverted. Hence the inversion boundary should be a sharp demarcation. In comparison for GaN the inversion domain boundary was found to be of the order of 100 nm or so [46].

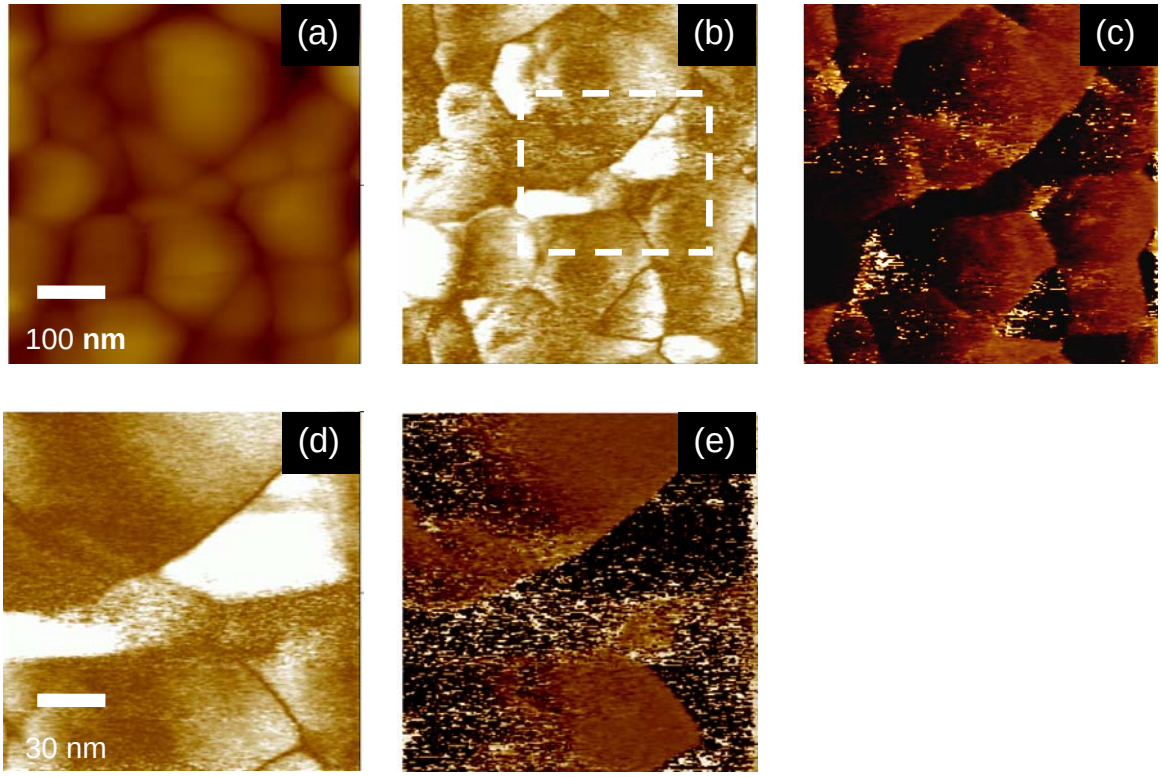

Figure 62: ZnO film sputtered on glass, with post-annealing. (a-c) are 500 x 500 nm^2 scans while (d, e) are 160 x 160 nm^2 scans from the area delimited by the frame in (b). (a) topography scan, (b, d) PFM magnitude, (c, e) PFM phase image.

7.5 Conclusion

The piezoelectric properties (d_{33}) of various ZnO thin films were determined using single beam interferometry, double beam interferometry and PFM. Using single beam interferometry inflated values on DC sputtered samples were reported which could be caused by buckling/bending of the samples. No reliable d_{33} was detected on RF sputtered samples. Clearly, DC sputtered ZnO (using a Zn target and O_2 for reactive sputtering) and RF sputtered ZnO (using a ZnO target) are based on different phenomena, as explained in [103] and in chapter 6.2.3. Therefore the films are readily distinguishable upon inspection using a SEM or AFM. DC sputtered films have a bigger grain size, typically in the range of 150 nm to 200 nm and roughness values around 40 nm, while RF sputtered films have a smaller grain size, typically around 50 nm and roughness values in of around 7 nm (refer to Chapter 5.3 for details) and higher resistivity than RF sputtered films. Also, the grain boundaries are more pronounced in DC sputtered films. It has been reported previously [104], that the grain boundaries are zones where surplus O_2 and other impurities are located. Therefore, the grain boundaries are zones of high stress, which are highly insulating and therefore prevent charge carriers from moving across. All these effects seem to promote the piezoelectric properties on our samples.

In contrary, our RF sputtered ZnO films have generally smaller grains, less pronounced grain boundaries and lower resistivity, which seems to inhibit d_{33}. It has to be noted that other groups have sputtered strongly piezoelectric ZnO films using RF sputtering as well [67, 73, 80]. However, after preliminary results, we decided to focus exclusively on DC sputtered ZnO.

We also determined that RIE performed on DC sputtered and not-annealed samples leads to increased d_{33} values.

Double beam interferometry excludes the influence of sample buckling/bending so the results appear more realistic.

Both interferometry methods have limitations in regards to the laser beam size, as the instrument measures an averaged d_{33} over the spot size. With our polycrystalline samples, which have mixed O_2 / Zn polarity areas, this results in a lower average d_{33}.

Both using single beam interferometry and PFM proved that the d_{33} of DC sputtered ZnO can be improved considerably through post annealing at 600 °C. However, no d_{33} was detected at higher temperatures.

PFM experiments reveal that the ZnO films have a complex domain structure with inversion domains. Cross-section profile analysis shows that these inversion domains are found independent of topography or piezoresponse in the as-grown samples. It is found that the intensity of the piezoresponse is dependent on the substrate and this has been related to the elastic compliance of the substrate. An attempt to improve the d_{33} response through annealing was performed. Although this improves the piezoresponse of ZnO on glass, the inversion domains still persist. Interestingly, after annealing, the regions of strong piezoresponse in the films are all correlated to domains that are out-of-phase with the applied signal. The cross-section analysis of the inversion domains shows domain boundary widths of approx. 1.5 nm and is in accord with HRTEM based investigations. The presence of inversion domains is believed to be one of the reasons for poorer d_{33} and PL response, compared to ZnO single crystals. Interestingly, the inversion band does not always follow the grain boundaries but can spread straight down the middle of a grain.

Chapter 8
Fabrication of device structures

8.1 Introduction

ZnO is a unique material that exhibits both semiconducting and piezoelectric properties. ZnO has its band edge at around 380 nm, which equals to a band-gap energy of around 3.37 eV. Light with a shorter wavelength (equals to higher energy, i.e. UV light) interacts with the film surface, excites electrons and sends them to higher energy states, generating electron-hole pairs [118, 119]. These added free carriers in the semiconductor layer also lead to lower resistivity. Visible light does not excite electrons,

ZnO is a "visible blind" UV sensing material [120, 121]. In this chapter we describe two methods of using ZnO coatings as a sensing surface.

In the latter part we attempted to combine piezoelectricity and UV detection capability into one device. The design, fabrication and characterisation of a "super coating" is described. It consists of a layer which has been optimised to achieve good PL and another layer with good d_{33} characteristics.

8.2 UV sensing experiments

Before elaborating further, I recall our main aim of this research, which is to deposit ZnO films with high resistivity, for potentially high d_{33} and PL. This has been achieved using DC sputtering (see chapter 5.2). Non-stoichiometric (Zn-rich) films with low sheet resistivity were rejected.

In order to test a UV light sensor an interfacing structure is required. One approach is to measure the sheet resistivity $R_{\square}$ as a function of (UV-) light exposure. A preliminary assessment using a probe station showed indeed light dependence. However, in order to obtain consistent measurements, more reliable contacts are required to be added on the films.

Schottky contacts are ideally suited for defect characterisation and device fabrication. By matching the contact materials and the ZnO layer these contacts create a depletion region at the boundary between them. This results in a diode structure.

However, the fabrication of Schottky contacts is quite labour intensive, as three different metals (Pt, Ti, Al) have to be deposited. In addition, these contacts have to be wired to an instrument, which necessitates a probe station or wire bonding.

A more elegant solution is the use of a surface acoustic wave (SAW) device structure that is added on the ZnO film to be analysed. No physical connection is required between the sensing surface and the interrogator. The fabrication requires only one lithographical step and a single metal deposition. No wire bonding is necessary and the quality of contacts (i.e. local depletion layer) is irrelevant. By carefully controlling environmental influences such as temperature variations or stress on the device the oscillating frequency of the device is tuned by UV wavelengths only. SAW sensing devices can be placed in hostile and inaccessible areas, with remote readout.

8.2.1 Determination of current-voltage characteristics using Schottky contacts

For this experiment, ZnO was DC sputtered on n-type silicon <100> substrates and post-annealed at various temperatures. Using optical lithography and lift-off a planar diode structure was fabricated on the films, as shown in Figure 63. It consists of a Pt circle (thickness = 25 nm) and Ti/Al annular ring (thickness = 40 nm/100 nm), capped with Pt (thickness = 30 nm). All metal depositions were performed using e-beam evaporation.

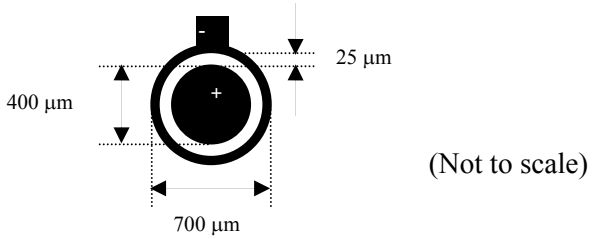

Figure 63: Planar diode structure consisting of Pt circle (anode) and Ti/Al/Pt annular ring (cathode).

All measurements were performed in an enclosed chamber which shielded the samples from unwanted stray fields and ambient light. A probe station was used to connect the Schottky contacts to the HP 4155A semiconductor parameter analyser which was used to perform the measurements.

The samples were exposed to various light sources:

- Dark, no ambient light
- Fluorescent light tube (daylight type), does not emit any energy in the UV spectrum
- "IV lamp", Leica CLS 150X, consisting of 50W cold light source and optical fibre light guides
- "UV lamp", contains halogen light bulb (UV filter removed), which emits energy in the UV spectrum

The sample annealed at 800 °C gave particularly good results as listed below.

In Figure 64 the I-V graphs are shown for sample measured with no ambient light and with progressively increased exposure to UV light. The black graph shows the response with no ambient light, the blue graph shows approximately the same response for fluorescent light, the amber graph shows increased current, because the IV light contains energy in the UV range. The yellow graph shows an order of magnitude increased conductivity compared with no ambient light, as the sample is exposed to even more UV light. However, the polarity of the diodes was opposite to those on bulk n-ZnO.

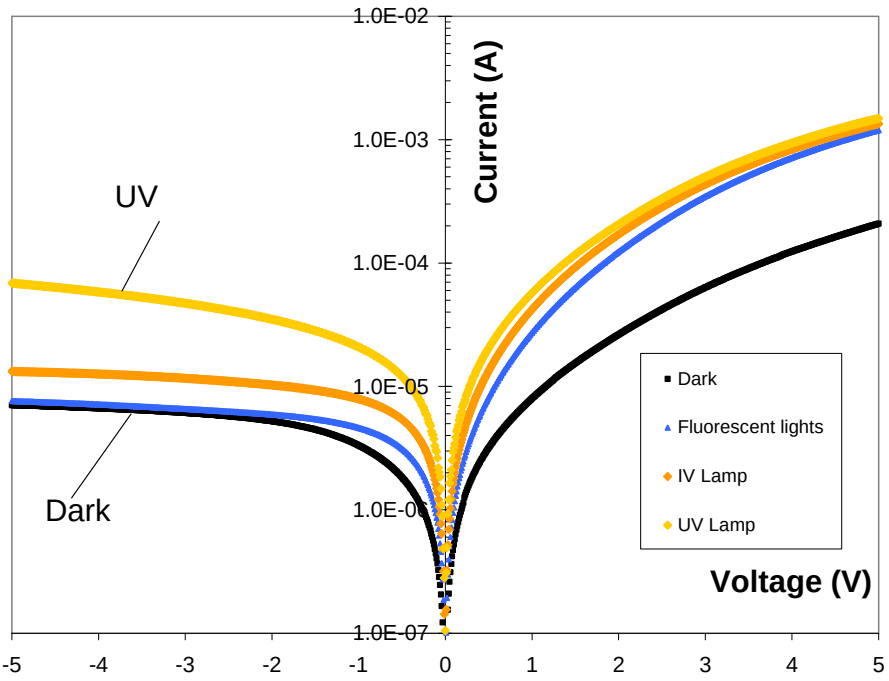

Figure 64: I-V graph: The various graphs show increased conductivity due to the sample being exposed to UV light.

The phenomenon of reverse polarity could be caused by two reasons:

a) vertical conduction mechanism, as shown in Figure 65.

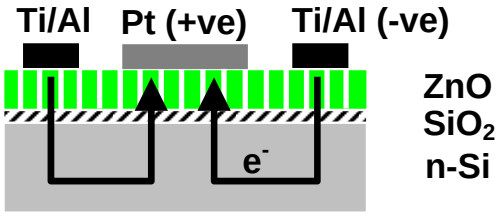

Figure 65: Vertical conduction mechanism trough sputtered ZnO layer. The current shown flows down the grains and through the doped substrate rather than across the grain boundaries.

In case of the vertical conduction mechanism (shown in Figure 65) the Pt electrode is designed as rectifying contact. However, an additional rectifying barrier at the ZnO-Si/SiO_2 interface as well as some photovoltaic effect could occur on illumination with light. Since the current transport from the Pt contact would be down the ZnO columns and then horizontal through the Si, and vertical back up the columns to the ohmic contact, an

additional double barrier would be provided by the Si/SiO_2 interface. This might explain the polarity reversal.

b) ZnO becomes p-type due to diffusion of As dopant from n-Si substrate during annealing, or the barrier occurs at the interface between ZnO and n-Si interface rather than at the interface between metal and ZnO contacts.

Figure 66 shows the results of measurements taken under exposure of four different light sources. Again the UV component of the light sources leads to considerably increased currents.

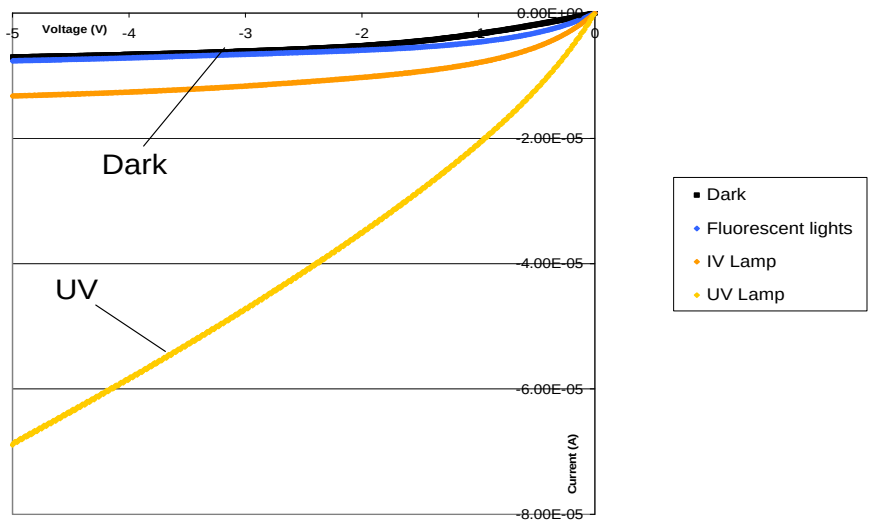

Figure 66: I-V graph (reverse characteristics), the various graphs show increased conductivity due to the sample being exposed to UV light

The black graph shows the response with no ambient light, the blue graph shows the response for fluorescent light and the amber graph shows an increased response for IV light. The yellow graph shows by a factor of 4 increased conductivity, as the sample is exposed to even more UV light.

8.2.2 Measurements using SAW devices

8.2.2.1 SAW devices and their interrogation

The functioning of SAW devices is based on the piezoelectric effect, which is detailed in chapter 2.1.2.

SAW devices work with their own designed resonance frequency, utilising the piezoelectric effect.

λ, the mechanical wavelength, is determined by the phase velocity and the operating frequency as follows: $\lambda = \frac{v_s}{f_{RES}}$

where v_s is the phase velocity of sound and f_{RES} is the center frequency.

The phase velocities of commonly used piezoelectric materials are listed in Appendix D.

Any SAW device is influenced by changing mechanical strain and temperature fluctuations. Therefore, SAW filter and oscillators are isolated from the environment to avoid an adverse effect by strain or vibration. They are either temperature compensated or kept at constant temperature. On the other hand, changing strain can be used to alter the characteristic of the piezoelectric material. A changing strain will affect the mechanical wave and the signal retransmitted will reflect these changes. For example, if a piezoelectric material is placed on a mechanical part which is used as stress receptor, the length of the SAW structure will be influenced by changing strain and therefore the delay time will change.

A basic SAW device looks as follows:

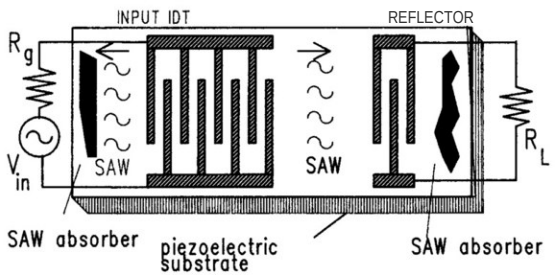

Figure 67: Schematic of Basic SAW device with IDT, reflector and absorbers.

Figure 67 shows a basic SAW device, the Input IDT (=Inter Digital Transducer) is generating a mechanical wave which travels in +/- x direction. The IDT on the right hand side could be used as follows:

- Variable resistance connected to reflector (as shown)
- Variable capacitance connected to reflector
- Variable inductivity connected to reflector

Any of these components will have an effect on the reflected signal.

As mentioned earlier, the reflected signal is also influenced by temperature and mechanical strain.

IDTs were invented in 1965 [122] as very efficient devices to generate and detect SAW waves on piezoelectric substrates.

The surface acoustic or mechanical wave can be imagined as follows:

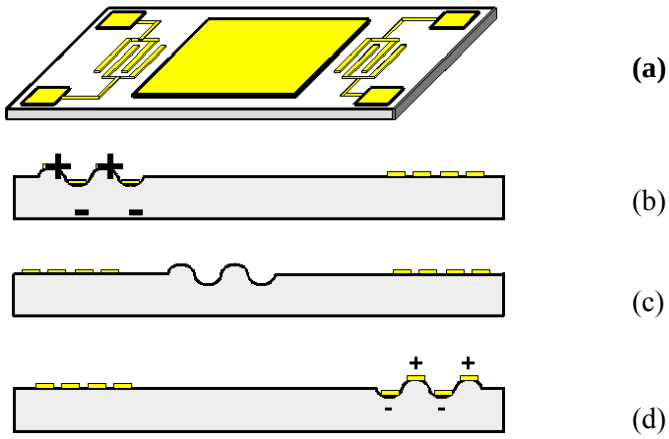

Figure 68: Basic SAW device illustrating distribution of surface acoustic wave.

In Figure 68 the schematic propagation of the surface acoustic wave along the substrate is illustrated. The general arrangement of a SAW device is illustrated in (a) consisting of an Input IDT on the left-hand side, the delay line in the center and the Output IDT on the right-hand side. A short RF voltage pulse applied at the left-hand IDT will generate a mechanical strain and displacement (as of Figure 4) and (b). This displacement forms a wave which travels in +/- x direction as shown in (c) (only + x direction shown). After a short time interval the wave will arrive at the destination (IDT on right hand side) as

shown in (d) but will have lost some of its energy. The IDT on the right hand side will convert the wave back into a voltage pulse.

The phase velocity of the mechanical wave and the piezoelectric coupling effect are dependent on the piezoelectric substrate used. A SAW device designed on substrate X will behave differently if fabricated on substrate Y and considerable re-engineering would be necessary to match the performance. Piezoelectric substrates with a high phase velocity allow higher frequency operation with the same mechanical pitch than substrates with low phase velocity. The design of SAW devices for very high frequencies (10 GHz range) is described in [123-125].

As shown above, SAW devices make use of acoustic (Raleigh) waves, which travel at and close to the surface of a piezoelectric substrate, such as lithium niobate, quartz or ZnO. A metallic structure consisting of an interdigitated transducer (IDT) and reflectors is used to generate and influence a mechanical wave which travels along the piezoelectric substrate. Further information can be found in [82, 126]. Figure 69 shows the general set-up of a SAW device consisting of a piezoelectric substrate, IDT and reflectors. The IDT can be connected to the reader via antenna (as shown) or via directly wired connection. The reader consists generally of a network analyser; in our case, a HP 8753D vector network analyser was used.

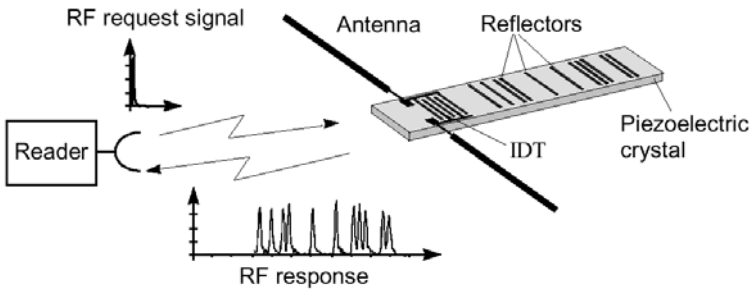

Figure 69: Schematic set-up of interrogation system and SAW device.

8.2.2.2 SAW device fabrication

SAW devices were designed using computer aided design software (L-Edit), using a range of design rules as listed in [82] and fabricated using optical lithography or EBL.

While optical lithography is well suited for relatively "large" structures (in the μm range) and fast mass production, EBL is ideal for prototyping. It allows defining very fine patterns down to the 10 nm range but is hampered by slow write speeds.

During the course of this work, which required the fabrication of different designs, mainly EBL was used. Metal deposition was performed using vacuum thermal evaporation. Its highly directional deposition allow easy lift-off.

For these experiments ZnO was sputtered on Si substrate and post-annealed at various temperatures. The SAW devices were fabricated using EBL, the fabrication sequence is listed in Appendix B.

The samples annealed at 700 °C gave a particularly good response to UV light exposure and the results are presented below.

8.2.2.3 Interrogation experiments

Using the setup as shown in Figure 69 and utilising a wired connection the SAW device was interrogated under different conditions. Figure 70 shows the response with ambient light (fluorescent lightning) which does not contain any energy in the UV spectrum. Two reflections at 820 ns and 1525 ns respectively are clearly visible. The same measurement was repeated with no ambient light, with the same result.

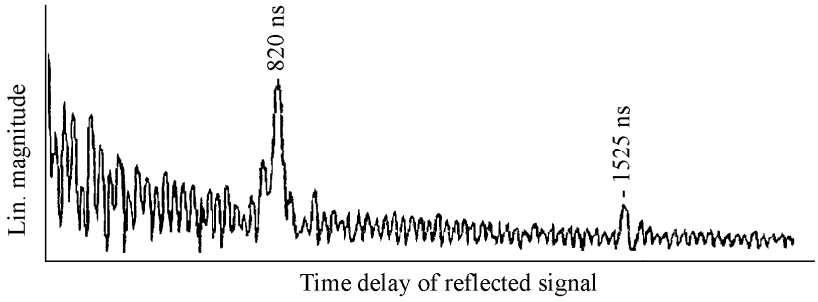

Figure 70: SAW response with ambient light showing two strong reflections at 820 ns and 1525 ns, respectively.

The device was exposed to additional UV light (using a halogen light bulb), first at low intensity, which lead to a slight decrease of the reflections, as shown in Figure 71.

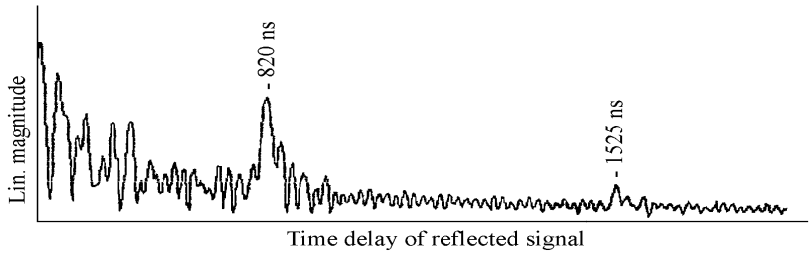

Figure 71: SAW response with ambient light and half bright UV light show two slightly weaker reflections at 820 ns and 1525 ns, respectively.

Then the UV light intensity was increased and the reflections disappeared altogether, as showed in Figure 72.

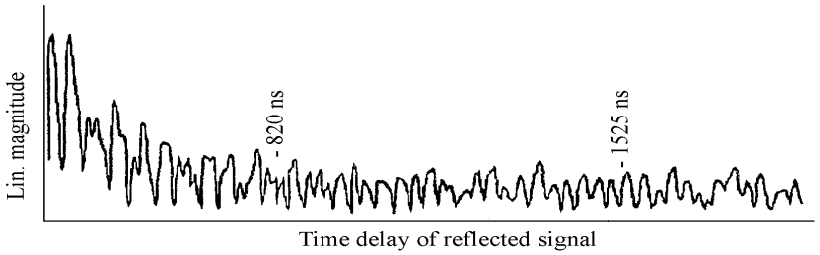

Figure 72: SAW response with ambient light and full bright UV light shows no reflections.

This effect is reversible, with fast response-time, but delayed by the update rate of the network analyser.

Outcome

As shown in the first experiment, ambient light from a fluorescent light tube does not influence the response of the SAW device, in other words, ambient light is not detected. ZnO is "visible blind" as its band edge at 380nm is outside the visible range.

UV light introduces considerable change in the SAW response, as shown in the second and third experiment.

The SAW properties are modified by UV light, since the incident light is absorbed by the semiconducting ZnO, generating electron-hole pairs. These free carriers in the semiconductor layer interact with the electric field accompanying the propagating SAW, resulting in an increased insertion loss and weaker response.

According to previous research [9] two different mechanisms are contributing to photoconductive properties in ZnO, a fast photoconductive process, which is related to bulk properties and a slow component, which is related to desorption and adsorption of oxygen atoms on the surface. The fast process is related to and strongly influenced by the slow one. Due to limits in our setup, we were able to track only the fast photoconductive process, but not trends over a longer time.

8.3 Towards the "super coating": Twin layer ZnO

Previous experiments revealed that generally the PL response of ZnO films increase with annealing temperature, as shown in Figure 53 (page 84). However, as shown in Figure 56 (page 90), the d_{33} values for not dry etched films are the highest for not annealed or at 600 °C annealed ZnO. The requirements for these two properties are therefore contradictory. Ideally, a "super coating" should be fabricated which combines high PL response and useful d_{33} values in one device. High PL response leads to high sensitivity in the UV region while good value d_{33} enables the efficient working of the SAW structure.

Combining the two sputtered layers is not straight forward. Obviously, the first sputtered layer has to be optimised for PL response by post-annealing, before the second layer is deposited on top (the second layer would lose its good piezoelectric properties during annealing). The first, for PL optimised layer is from now on called "PL coat" and the second, for d_{33} optimised layer is from now on called "d_{33} coat".

However, the incident light has to reach the PL coat, which is covered by the d_{33} coat. It was decided, in the first instance, to use an optically transparent substrate. Quartz was chosen, as it is has a wide optical transmission range from 175 to 2400 nm [127] and allows the sputter-deposition of highly oriented/organised films which, after annealing, yield good PL, as shown in Figure 50 (page 81). The PL shows particularly good values for between 900 °C and 1100 °C optimised films.

Therefore, for this experiment, two ZnO coats were deposited on quartz substrates. The PL coat with a thickness of approx. 100 nm was DC sputtered on the substrates, which were subsequently post-annealed at 900 °C and 1100 °C, respectively.

The d_{33} coat was deposited on top, again using DC sputtering, with a thickness of approx. 200 nm. No post-deposition treatment was performed.

Figure 71 shows the arrangement of the super coating. The SAW structure is the last component to be added, after the two ZnO coats have been deposited and optimised. The light to be detected is to enter through the quartz waver.

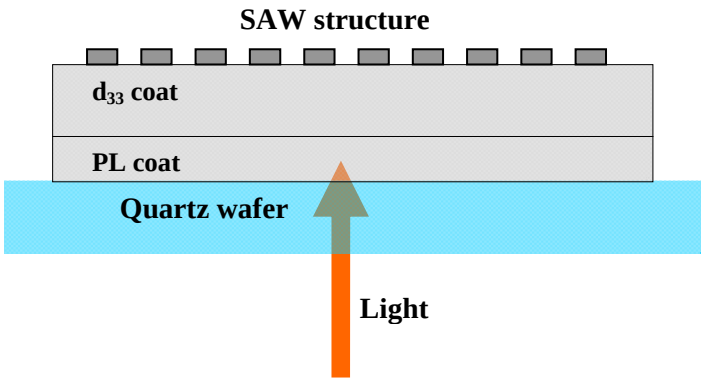

Figure 73: "Super coating" consisting of two DC sputtered ZnO layers on quartz substrate. Light can be directed to the PL coat from the back through the quartz substrate.

Figure 74 shows an SEM micrograph (top view) of the twin layer ZnO film with combined thickness of around 300nm. The cross section is shown in Figure 75. The grains show interruptions around the halfway point, as indicated by the arrows. This was expected, since the deposition was interrupted to allow post-annealing.

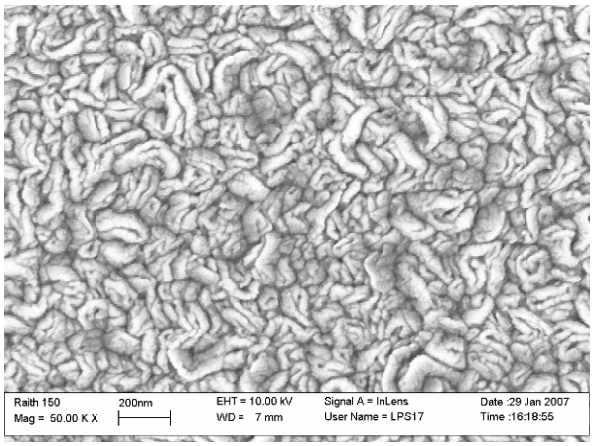

Figure 74: SEM image of twin coat ZnO on quartz substrate (top view). The grains look rather broken up; they are not as regular and symmetric as seen on a single sputtered film.

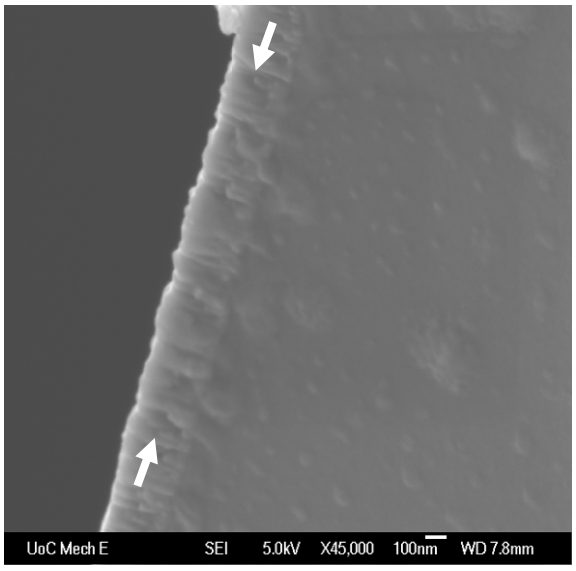

Figure 75: Cross sectional SEM image of twin coat ZnO on quartz substrate. The grains look interrupted at the line between the arrows.

After cleaving the sample cross sectional SEM analysis was performed, which revealed further details. Figure 76 shows clearly the two different films: The PL coat is on the bottom, sitting on the Si substrate, the d_{33} coat is sitting on top of the PL coat. Cleaving lead to the top film to partially break off and reveal two distinct structures. The first sputtered layer has bigger grains due to annealing.

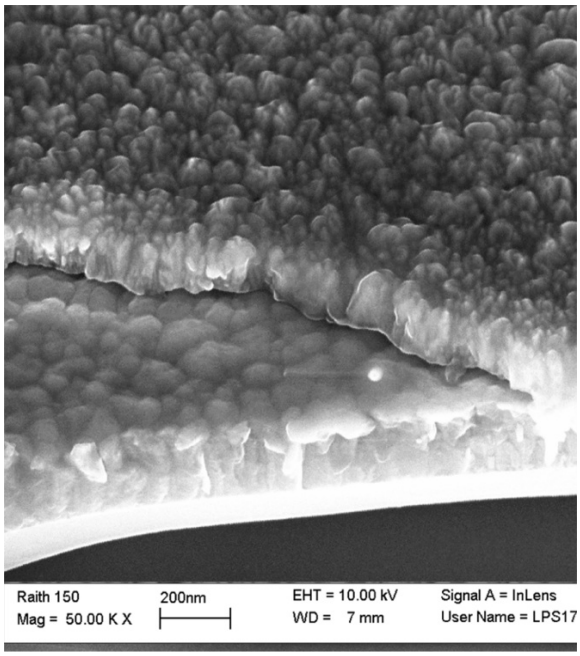

Figure 76: Cross sectional SEM image of twin coat ZnO on cleaved quartz substrate.

The XRD intensity graph is shown in Figure 77. Two strong peaks are visible, one at 34.6 degrees and the other one at 35 degrees. No other peaks were detected. Therefore the twin sputtered film contains two layers that are strongly c-axis oriented.

Generally, the diffraction peaks of unstrained films are at slightly higher angle compared to the diffraction peaks of uniformly strained films. Since the annealed bottom layer contains less residual strain, its diffraction peak is at a slightly higher angle (35 degrees) than the non-annealed layer (34.6 degrees).

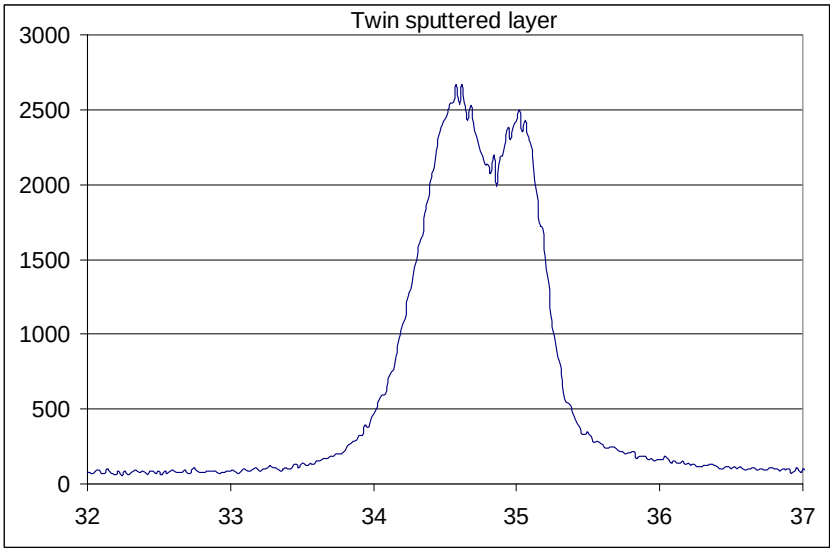

Figure 77: XRD scan of twin sputtered film deposited on quartz shows one peak at 35 deg for the first sputtered and at 900 °C annealed layer and a another peak at 34.6 deg for the second sputtered layer. FWHM = 0.932 degrees

RBS analysis on this structure showed light impurities (such as C) for the top 20 nm of the sputtered ZnO, then a stoichiometric layer of 390 nm thickness (Zn:O ratio 1:1). For detailed RBS results refer to Appendix D (samples analysed 02/2007).

d_{33} measurements or UV sensing experiments were not performed on these films. Suggestions for further experiments are listed in Chapter 9.2.

Summary

Twin layered films were successfully deposited on Quartz substrate. The films adhere well to each other and the substrate. XRD diffraction revealed two characteristic ZnO peaks for both a strained and a relaxed film. Both films have good stoichiometry, however, the top layer shows light impurities, possibly caused by C. With careful choice of thickness of the two coatings and post- annealing both good PL with good d_{33} should be achieved.

8.4 Smallest features on sputtered ZnO

In order to maximise the working frequency of a SAW device the pitch or feature size of the IDTs needs to be fabricated as small as possible. An IDT consisting of 200 nm wide Al tracks on a 400 nm pitch would result in a working frequency of approx 5 GHz (see

Chapter 8.2.2.1). EBL is easily able to write these patterns; however, with our limited means it would have been impossible to test the devices at this high frequency.

IDTs with various feature sizes down to 200 nm were fabricated using EBL, Al deposition and lift-off. (For recipe refer to Appendix B). The proximity effect was noticeable, but was overcome with a slightly lower exposure dosage (100uA/cm^2 rather than the "standard" 120uA/cm^2).

Figure 78 shows the result of these experiments. The Al tracks are well developed but have a rough surface, due to the underlying ZnO substrate. Due to the size of the individual ZnO crystals, the smallest feature size seems to be constrained by the nature of the substrate and the roughness rather the limits of EBL (charging and proximity effects).

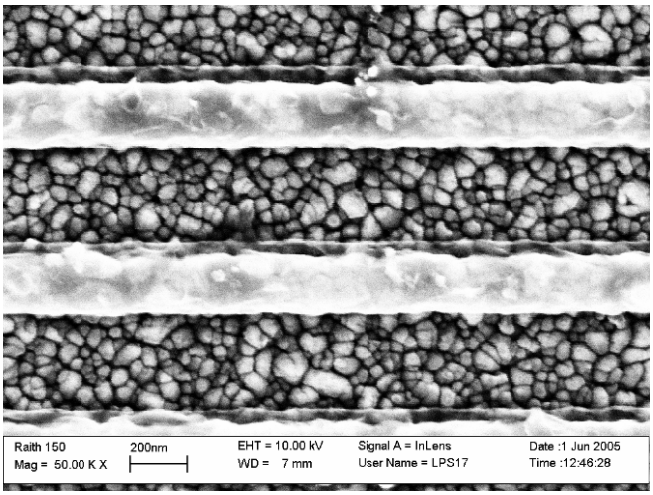

Figure 78: SEM image of Al coated electrodes with a line with of 200 nm (80 nm thick) fabricated on DC sputtered ZnO.

Another IDT section is shown in Figure 79. Some tracks peeled off during lift-off due to insufficient adhesion between the Al and the rough ZnO substrate.

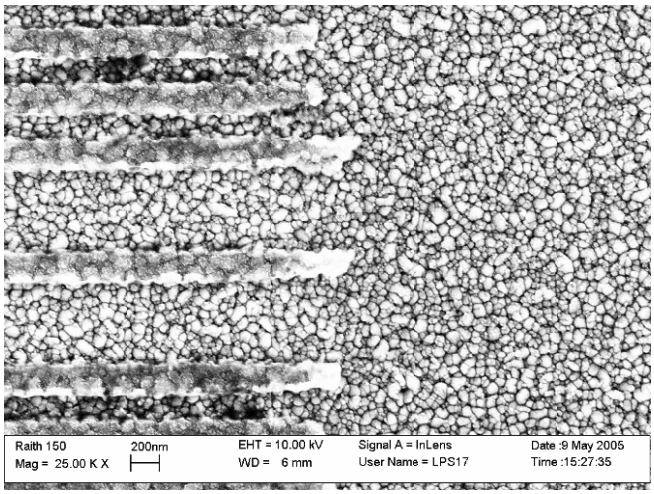

Figure 79: SEM image of Al coated electrodes. The pitch width is 400 nm and the Al electrodes are approx 210 nm wide. Some electrodes are missing due to lack of adhesion on the relatively rough surface.

In Figure 80 an angled SEM micrograph shows the Al coating sitting on the tops of the crystals, rather than forming an intimate bonding with the ZnO.

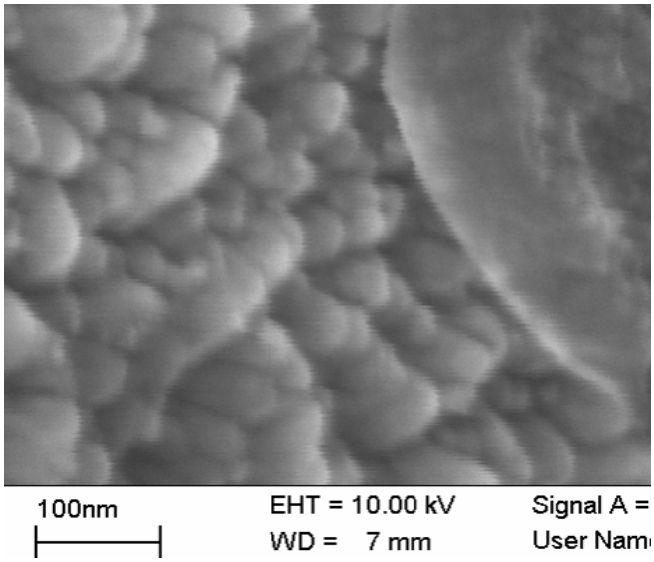

Figure 80: SEM image of Al coated electrode (angled view). The deposited Al coating appears to sit on top of the ZnO grains.

Outcome

IDTs with a pitch of 400 nm and track widths of around 210 nm have been fabricated using EBL, Al deposition and lift-off. The size limit is given by the grain size and film

roughness of the ZnO layer rather than the limits of lithography. For even smaller features, however, films with smaller grains and lower roughness values are needed.

Chapter 9
Conclusion and suggestions for future work

9.1 Conclusion

A range of extensive sputtering conditions were studied and characterisations were performed in order to achieve highly resistive and stoichiometric ZnO films. DC sputtered films have a grain size of around 200 nm and a surface RMS roughness of 75 nm, in contrast the RF sputtered films have a grain size of around 50 nm and a surface roughness of 7 nm, as determined from AFM images. Both the DC and RF sputtered films appear transparent and have 1:1 (Zn:O) stoichiometry, as determined by RBS analysis. DC sputtered films show generally high PL and piezoelectric properties, however, the RF sputtered films show lower PL intensity and no piezoelectric response was traced. The grain boundaries are influenced by impurities and defects, which in turn are different depending on the type of sputtering. It is thought that the bigger grain size of DC sputtered ZnO promotes the formation of highly resistive grain boundaries. This inhibits charge transfer between individual grains, which is also favourable for piezoelectric properties. Therefore the decision was made to focus on DC sputtered films for this study.

During the course of this research it became clear that the quality of sputtered ZnO films is crucially dependent on the sputtering conditions, the choice of substrate and post-sputtering treatments. Investigation into the deposition mechanism of DC sputtered ZnO showed that the ZnO molecules form nucleation islands which are joined up as the deposition progresses.

Post-treatment of the films using annealing in N_2 and dry etching showed significant improvements in regards to PL response, depending on the base substrate used. Sapphire, for example, is a substrate material which has a small lattice mismatch in relation to ZnO and therefore allows for high quality depositions without any post treatment, as determined by PL and XRD analysis. Conversely, ZnO deposited on Si substrates yields quite low PL for as-sputtered samples. However, annealing at higher temperatures leads to relaxation of the films and the highest PL values of all the samples analysed were recorded after annealing at 1100 °C.

The d_{33} values were determined using single and double beam interferometry on ZnO sputtered on Si. Generally, the highest values were obtained for as-sputtered samples or

after annealing at up to 700 °C. Clearly the best PL results were observed at high annealing temperatures while the best d_{33} values were measured on as-sputtered films or after annealing at low temperatures.

SAW devices were fabricated on sputtered and at 700 °C post-annealed samples. These devices were tested under UV light exposure and showed strong UV sensitivity. In order to function, SAW devices rely on the piezoelectric properties of the ZnO layer, which in turn are affected by the resistivity values of the substrate. We conclude that during UV exposure the incident light is absorbed by the semiconducting ZnO, generating electron-hole pairs, which lowers the resistivity value. When interrogating the SAW device the response weakens because the lowered piezoelectric value leads to higher insertion losses.

PFM scans of various samples showed the magnitude distribution and phase information of the d_{33} across the samples, with a resolution in the nm range. It is shown that on a given sample some areas vibrate in phase with the applied signal, which equals to positive d_{33} and some areas vibrate out of phase, which equals to negative d_{33}. This leads to an overall smaller net d_{33} on the films than expected.

In order to combine films with good PL response, which in turn give high UV sensitivity values for use as a sensing device and high d_{33} values, that allow the SAW device to function, a "super coating" was developed to combine coatings with high PL and high d_{33}. Preliminary analysis showed promising results for samples consisting of two ZnO layers.

The highest possible working frequency of SAW devices, which needs the smallest possible features, was investigated. The smallest IDTs or metal features in the range of 200 nm were successfully fabricated using EBL lithography, metal evaporation and lift-off. The limiting factor is not given by lithography, but rather by the grain size of DC sputtered ZnO in the range of 200 nm and therefore prevents the fabrication of smaller features.

9.2 Suggestions for future work

During this research we reported very encouraging results of our UV sensing experiments, notably the sensing of UV light on ZnO thin films, using both Schottky diodes and SAW devices. In a future project, the properties of the "super" coating should be further characterised in order to ascertain the performance as UV sensing device in combination

with good d_{33}. The thickness ratio of the two layers and the annealing conditions should be varied. Further experiments to find the influence of various substrates on the super coating should be initiated. Also, the influence of RIE on the PL and d_{33} coat should be explored in order to understand the effects of surface modification. Finally, SAW devices should be built on these coatings and characterised.

P-type doping is still a hot topic and was briefly touched during this research. It was speculated that some films became p-type during annealing due to diffusion of As dopant from the n-Si substrate into the ZnO. It would be prudent to repeat and expand these experiments using differently doped substrates. Further analysis using Schottky contacts to determine C-V characteristics should be performed.

Other sensing properties, such as gases, volatile organic compounds (VOCs), bacteria, or streptavidin (a tetrameric protein that has various biochemical applications), may also be investigated. In order to fabricate rugged devices further miniaturisation would become necessary and also the protection of the devices, i.e. capping layers and encapsulating.

For mass production it is important that ZnO based SAW devices can be fabricated in a CMOS compatible fashion. One way is to apply a thin passivation layer, such as SiN, which prevents contamination [84]. Other methods are listed in [128, 129]. The most suitable method would need to be confirmed.

At the moment, research in ZnO is hotter than ever and research-wise, I believe interest in ZnO is here to stay.

Appendix A
Publications

Publications in referred journals

Schuler, L. P., Valanoor, N., Miller, P., Guy, I., Reeves, R. J., & Alkaisi, M. M. (2007). The Effect of Substrate Material and Postannealing on the Photoluminescence and Piezo Properties of DC-Sputtered ZnO. Journal of Electronic Materials (2007), 36(4): p. 507-518.

Schuler, L. P., Alkaisi, M. M., Miller, P., & Reeves, R. J. (2006). UV sensing using surface acoustic wave device on DC sputtered ZnO monolayer. Microelectronic Engineering, 83(4-9), 1403-1406.

Schuler, L. P., Alkaisi, M. M., Miller, P., Reeves, R. J., & Markwitz, A. (2005). Comparison of DC and RF sputtered zinc oxide films with post-annealing and dry etching and effect on crystal composition. Japanese Journal of Applied Physics, Part 1: Regular Papers and Short Notes and Review Papers, 44(10), 7555-7560.

ME Thesis

Schuler, L. P. (2003). Wireless Identification and Sensing using Surface Acoustic Wave Devices. University of Canterbury, Christchurch, New Zealand.

Invited talks and seminars

Schuler, L. P. (2006). Fabrication of functional ZnO coatings for improved piezoelectric properties and photoluminescence. Paper presented at the Invited seminars, at Stanford University, Rutgers University, and Ohio State University, USA.

Schuler, L. P., Alkaisi, M. M., Miller, P., Allen, M., Valanoor, N., & Reeves, R. J. (2006). Zinc Oxide: A metallic semiconductor with unique properties. Paper presented at the Invited departmental seminar, The MacDiarmid Institute, University of Canterbury, Christchurch, New Zealand.

Schuler, L. P., Alkaisi, M. M., Miller, P., & Reeves, R. J. (2005). UV sensing using Surface Acoustic Wave device on DC sputtered ZnO monolayer. Invited paper presented at the MacDiarmid Student Symposium 2005, Wellington, New Zealand.

Conference talks

Schuler, L. P., Valanoor, N., Miller, P., Markwitz, A., Reeves, R. J., & Alkaisi, M. M. (2007). Investigation of piezoelectric domain structures using PFM on DC sputtered ZnO films. Paper presented at the AMN-3 Third international conference on advance materials and nanotechnology, Wellington, New Zealand.

Schuler, L. P., Valanoor, N., Miller, P., Guy, I., Reeves, R. J., & Alkaisi, M. M. (2006). The Effect of Substrate Material and Postannealing on the Photoluminescence and Piezo Properties of DC-Sputtered ZnO. Paper presented at the EMC conference, Pennsylvania, USA.

Schuler, L. P., Alkaisi, M. M., Miller, P., & Reeves, R. J. (2005). UV sensing using Surface Acoustic Wave device on DC sputtered ZnO monolayer. Paper presented at the MNE 05, Vienna, Austria.

Ranford, S. L., Schuler, L. P., Ellery, M. W., Walls, R. J., & Piper, C. F. (2001, April 2001). Major advances in textile process control through visible/near infra red analysis. Paper presented at the Textile Institute Conference, Melbourne, Australia.

Conference poster presentations

Miller, P., Schuler, L. P., Alkaisi, M. M., & Reeves, R. J. (2007). Effect of substrate and annealing temperature on the optical and physical properties of DC sputtered ZnO films, AMN-3 Third international conference on advanced materials and nanotechnology, Wellington, New Zealand.

Miller, P., Schuler, L. P., Alkaisi, M. M., & Reeves, R. J. (2006). Effect of substrate and annealing temperature on the optical and physical properties of DC sputtered ZnO films, 4th International Workshop on ZnO and Related Materials, Giessen, Germany.

Schuler, L. P., Alkaisi, M. M., Miller, P., Reeves, R. J., & Markwitz, A. (2005). Comparison of DC and RF sputtered ZnO films, AMN-2 Conference, Queenstown, New Zealand.

Schuler, L. P., & Alkaisi, M. M. (2004). Dry Etching of Sputtered Piezoelectric ZnO, 3rd ZnO conference, Sendai, Japan.

Schuler, L. P., & Alkaisi, M. M. (2003). Wireless Force-Sensing in Bone Implants, 2003 FiRST Scholarship Awards, Christchurch, New Zealand.

Unpublished reports

Schuler, L. P., Alkaisi, M. M., & Meade, W. J. (2003). Wireless Identification based on passive Surface Acoustic Wave devices. Lincoln, New Zealand: Canesis Network Limited.

Schuler, L. P., Alkaisi, M. M., & Meade, W. J. (2003). Wireless Switching based on passive Surface Acoustic Wave devices. Lincoln, New Zealand: Canesis Network Limited.

Schuler, L. P. (2002). Evaluation of RFID scanning technology for livestock applications: LincLab TechNet Report.

Wood, E. J., Marsh, C. M., Schuler, L. P., & Williams, A. (2002). On-farm wool testing options for new technologies: LincLab Australia Client Report CLR02/19.

Wood, E. J., Walls, R. J., & Schuler, L. P. (2000). WRONZ Mark II carpet walking comfort test.

Schuler, L. P. (2000). Order tracking feasibility study.

Appendix B
Recipes

RCA clean for Si wafers

Since there are two classes of contamination two separate cleaning procedures are used to remove each of them. Both chemical cleaning procedures and particulate cleaning techniques must be employed to produce a completely clean surface.

Chemical cleaning is used to remove chemically bonded films from wafer surfaces. Conventional chemical cleaning is performed with a series of acid and rinse baths. Bare silicon or silicon with only thermally grown oxide is chemically cleaned using the RCA method, as described below.

1. Preliminary cleaning
   If photoresist is present on the wafer, it is removed by plasma oxidation stripping and/or immersion in an inorganic resist stripper (e.g. H_2SO_4-H_2O_2). After removing from this solution, the wafer is rinsed in DI water at room temperature

2. Removal of residual organic contaminants and certain metals
   A fresh mixture of H_2O-NH_4OH-H_2O_2 (5:1:1 by volume) is prepared and heated to 80 ºC. The wafer is submerged in the solution for 10-15 min. Afterwards the wafer is rinsed in DI water for one minute.

3. Stripping of the hydrous oxide film formed during step 2
   (not necessary if a thermally grown SiO_2 film completely covers the wafer.)
   The wafer is submerged for 15 seconds into a mixture of 1 volume HF (49%) and 10 volumes H_2O. The exposed silicon (but not SiO_2) should repel H_2O as the wafer is pulled out of this solution. After that the wafer is rinsed for a short time (20-30 sec) in DI water. The short rinse minimises regrowth of the oxide.

4. Desorption of remaining atomic and ionic contaminants
   A fresh mixture of H_2O:HCl:H_2O_2 (6:1:1 by volume) is prepared and heated to 80 ºC. The still wet wafer from step 3 (or step 2) is submerged into the solution for 10-15 minutes. The wafer is next rinsed in DI water.

5. The wafer is dried using N_2.

6. The wafer is ready for immediate processing (storage should be avoided).

Annealing

Annealing was generally performed on sputtered ZnO with a nominal thickness of 500 nm, deposited on various base substrates.

Recipe

- Switch on Furnace tube, set desired temperature (max. temperature = 1200 °C).
- Open N_2 gas valve, set flow to 10 sccm.
- After desired temperature has been reached, open furnace lid, transfer samples into furnace tube.
- Remove sample again after desired time (usually 30 mins).

Note: Some films will crack due to thermal shock at high annealing temperatures during inserting/removal. To avoid this, films should be slowly inserted/removed or left inside while the furnace cools down after annealing.

Dry etching (RIE)

For these experiments ZnO films with nominal thickness of 900 nm were DC and RF sputtered on glass sliders.

NiCr dots with a thickness of 40 nm (as etch barriers) were deposited using optical lithography and lift-off.

Etching was performed as follows: The plasma power was kept at 200 W, which results in a power density of 2.5 W/cm^2, CHF_3 was used as etching gas with a flow of 25 sccm, the etching pressure was kept at 20 mTorr and the electrode temperature was kept at -20 °C. The etching time was 30 min and etch rates of around 5 nm/min were achieved.

Optical lithography (typical parameters)

Using AZ 1500 resist.

- Clean substrate

- Spin AZ 1500 resist @ 4000 RPM → thickness = 1500 nm
- Soft bake on hotplate @ 100 °C for 90 seconds
- Exposure using mask aligner for 12 seconds
- Develop using AZ MIF 300 for 17 seconds
- Metal evaporation to required thickness
- Lift-off in acetone

EBL lithography sequence (typical parameters)

Using twin layer of PMMA.

- Clean substrate
- Spin 4% LMW PMMA @ 2000 RPM→ thickness = 160 nm
- Soft bake in oven @ 185 °C for 20 mins
- Spin 2.5% HMW PMMA @ 3000 RPM → thickness = 50 NM
- Soft bake in oven @ 185 °C for 20 mins
- Exposure using Raith 150 @ nominal dosage of 120uA/cm^2
- Develop using 3 : 1 IPA : MIBK for 30 seconds
- Metal evaporation to required thickness
- Lift-off in acetone

Successful sputtering procedure

The following sputtering procedure was normally used:

1. Load samples on sample holder, locate above sputter target for uniform sputtering (for larger samples rotate sample holder)
2. Pump down to 10^{-5} mbar
3. Introduce O_2 (9 sccm)
4. Introduce Ar (6 sccm), or amount necessary to desired pressure of 1.2×10^{-2} mbar

5. Set up DC plasma source
6. Ignite plasma
7. Presputtering for ten minutes
8. Sputtering to required thickness

Appendix C

Results of sputtering experimental series

Measured resistance values from various DC sputtered samples, from [82].

O_2		Ar		Outcome (colour impression)	Sputtering rate [nm/min]	Resistance (Measured according to method listed in Chapter 4.9.)
Flow (sccm)	Partial pressure (mbar)	Flow (sccm)	Total pressure (mbar)			
5	3.4×10^{-3}	10	1.2×10^{-2}	Looks black. Dektak and AFM show rough surface.	20.0	Low resistance coating. 12.78 kΩ
7	6×10^{-3}	8	1.3×10^{-2}	Looks black. Dektak shows rough surface.	33.0	Bit higher resistance than before. 29.76 kΩ
9	7×10^{-3}	6	1.1×10^{-2}	Almost transparent, rod bluish, hard to scratch	14.3	Insulator, same as glass
9	7.5×10^{-3}	6	1.2×10^{-2}	Greenish	9.0	Insulator, same as glass
9	7×10^{-3}	6	1.2×10^{-2}	Almost transparent	6.75	Insulator, same as glass
11	8.5×10^{-3}	4	1.2×10^{-2}	Almost transparent	2.5	Insulator, same as glass
13	1.0×10^{-2}	2	1.1×10^{-2}	Almost transparent	2.5	Insulator, same as glass
9	7×10^{-3}	6	1.2×10^{-2}	Almost transparent	4.0	Insulator, same as glass
9	6.5×10^{-3}	8	1.2×10^{-2}	Almost transparent	3.88	Insulator, same as glass
9	6.5×10^{-3}	8	1.2×10^{-2}	Almost transparent	6.63	Insulator, same as glass
9	6.5×10^{-3}	8	1.1×10^{-2}	Almost transparent	6.6	Insulator, same as glass
9	6.5×10^{-3}	8	1.3×10^{-2}	Almost transparent	5.68	Insulator, same as glass
9	6×10^{-3}	9	1.2×10^{-2}	Purple	6.3	Insulator, same as glass

Appendix D

Commonly used piezoelectric materials

The most commonly used piezoelectric materials are listed below:

Material	Orientation		vph	k2	TCD	
	Cut	Prop.				
Quartz	ST	X	3158 m/s	0.1%	0	
	37° rotY	90° rotX	5094 m/s	0.1%	0	
$LiNbO_3$	Y	Z	3488 m/s	4.1%	94 ppm/°C	
	41° rotY	X	4750 m/s	15.8%	69 ppm/°C	
	128° rotY	X	3980 m/s	5.5%	75 ppm/°C	
$LiTaO_3$	36° rotY	Z	4220 m/s	6.6%	30 ppm/°C	
ZnO	Sputtered (grains normal to surface)		9180m/s			[130, 131]

Where:

Orientation Cut:	Indicates the crystalline orientation of the substrate surface normal
Orientation Prop:	Indicates the crystalline orientation of the wave propagation direction
vph:	phase velocity
k2:	electro-mechanical coupling coefficient
TCD:	Temperature Coefficient of Delay

Appendix E

RBS results

All RBS analysis work was performed at GNS, Lower Hutt.

RBS & X-ray analysis of ZnO films

Date: 01/2005

Sample # DC15, RF15 (annealed, no RIE)

Summary

- The ZnO layer in the DC series is a 54 nm (450 x 10^{15} atom/cm^2) layer of $Zn_1O_{1.7}$ followed by a uniform layer of Zn_1O_1 with a thickness of 284 nm (2350 x 10^{15} atom/cm^2). A small amount of Zn diffusion into the Si substrate may also be occurring.

- The ZnO layer in the RF series is 36 nm (300 x 10^{15} atom/cm^2) thick composed of $Zn_1O_{1.7}$ followed by a diffusion layer of Zn into the Si substrate. The diffusion layer has a composition of $Zn_{0.1}Si_1$ with a thickness of 47 nm (390 x 10^{15} atom/cm^2) layer.

Density used is 8.28 x 10^{15} atom/cm^3

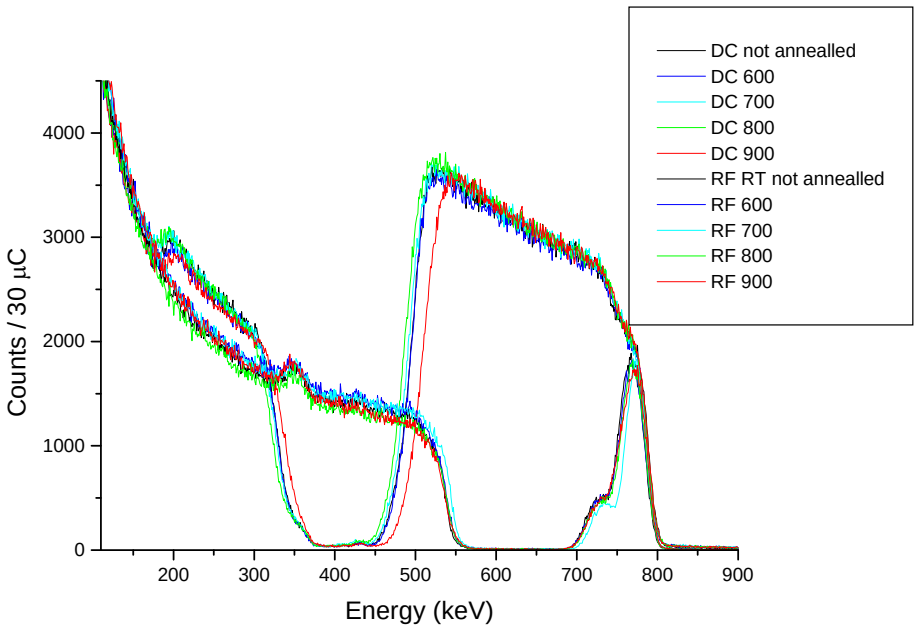

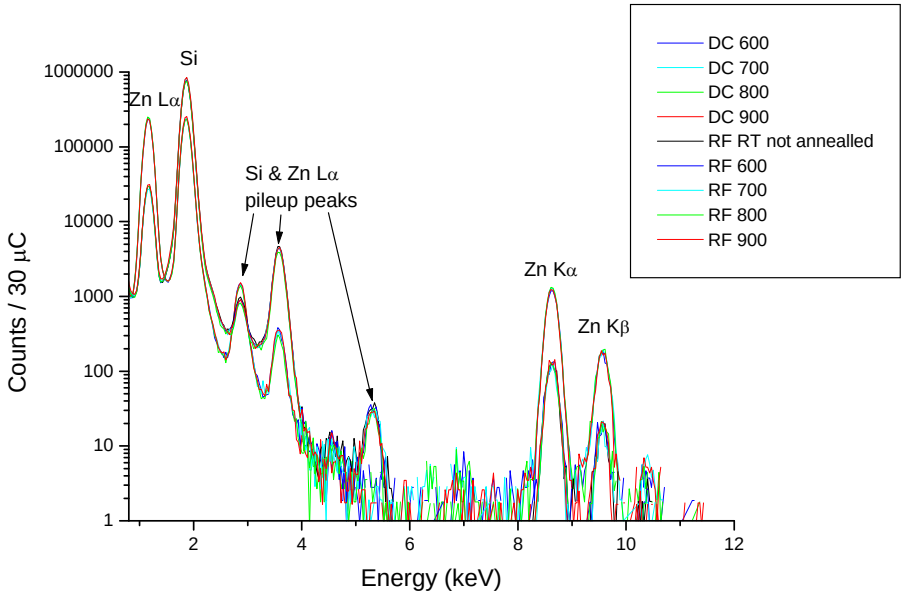
DC 600
DC 700
DC 800
DC 900
RF RT not annealled
RF 600
RF 700
RF 800
RF 900
Si
Zn Lα
Si & Zn Lα
pileup peaks
Zn Kα
Zn Kβ
Counts / 30 µC
Energy (keV)
1000000
100000
10000
1000
100
10
1
2
4
6
8
10
12

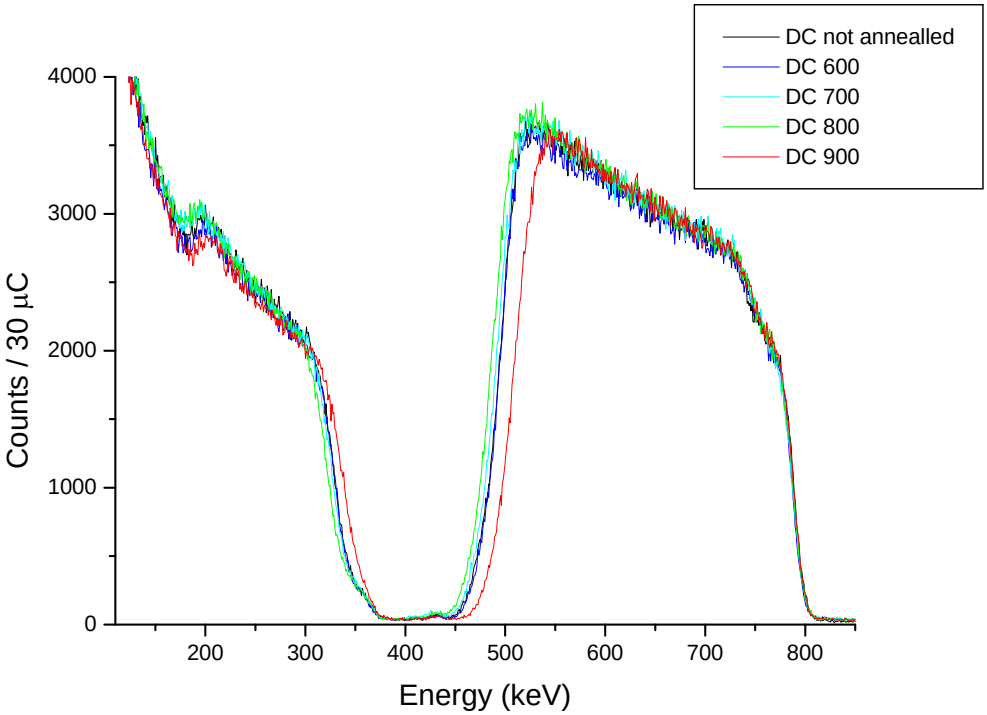
DC not annealled
DC 600
DC 700
DC 800
DC 900
Counts / 30 µC
Energy (keV)
4000
3000
2000
1000
0
200
300
400
500
600
700
800

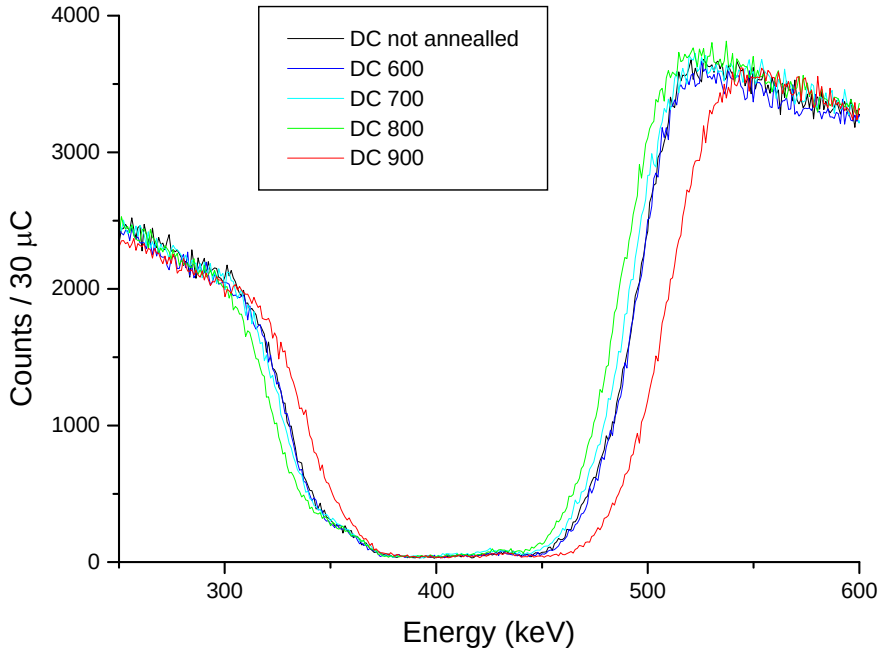
DC not annealled
DC 600
DC 700
DC 800
DC 900
Counts / 30 µC
Energy (keV)
0
1000
2000
3000
4000
300
400
500
600

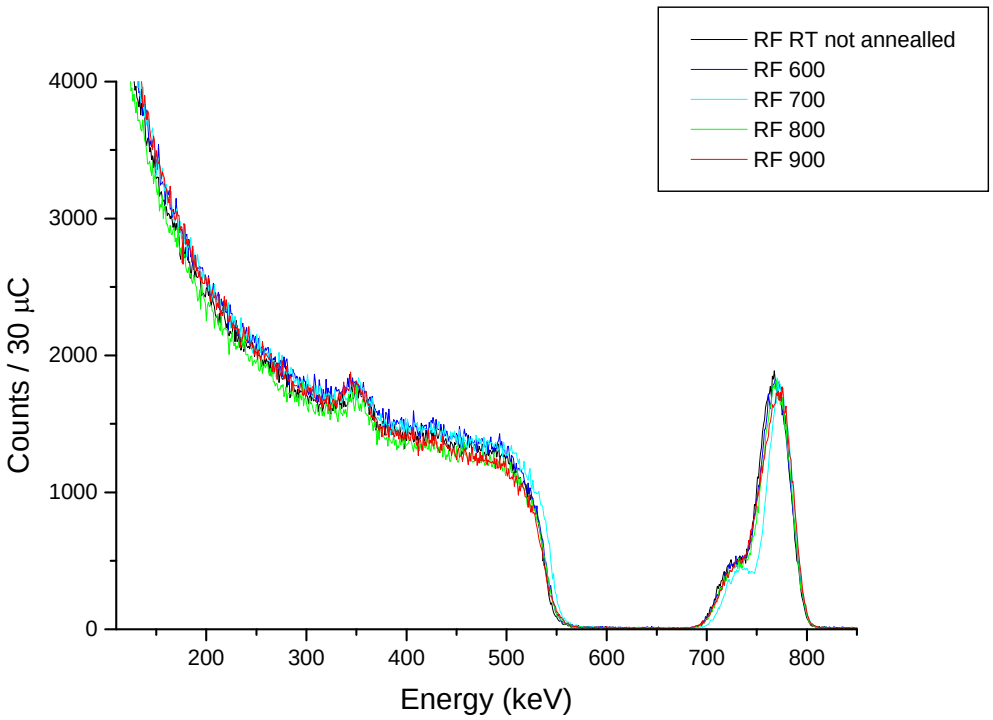
RF RT not annealled
RF 600
RF 700
RF 800
RF 900
Counts / 30 µC
Energy (keV)
0
1000
2000
3000
4000
200
300
400
500
600
700
800

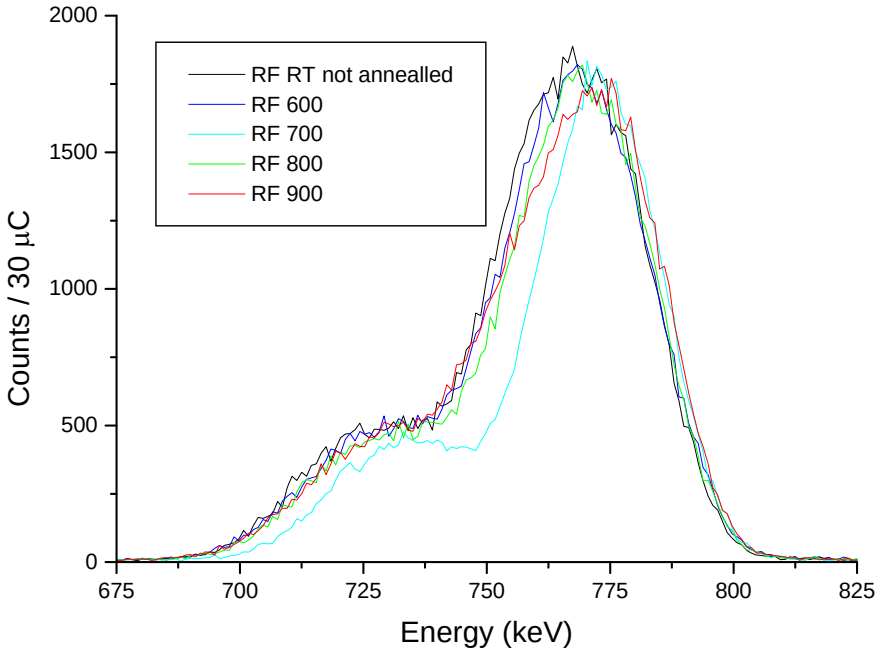
RF RT not annealled
RF 600
RF 700
RF 800
RF 900
Counts / 30 μC
Energy (keV)
2000
1500
1000
500
0
675
700
725
750
775
800
825

RBS File: I:\ibadata\2005\jan05\ja31032.rbs

Identifier:

LTCT Text:

Date:

Beam: 1.000 MeV 4He+ 30.00 uCoul @ 0.00 nA

Geometry: IBM Theta: 0.00 Phi: 15.00 Psi: 0.00

MCA: Econv: 0.990 60.000 First chan: 0.0 NPT: 1024

Detector: FWHM: 20.0 keV Tau: 0.0 Omega: 0.770

Correction: 1.2000

#	Thickness	Sublayers	Composition . . .
1	450.00 /CM2	auto	Zn 1.000 O 1.700
2	2350.00 /CM2	auto	Zn 1.000 O 1.000
3	1000000.00 /CM2	auto	Si 1.000

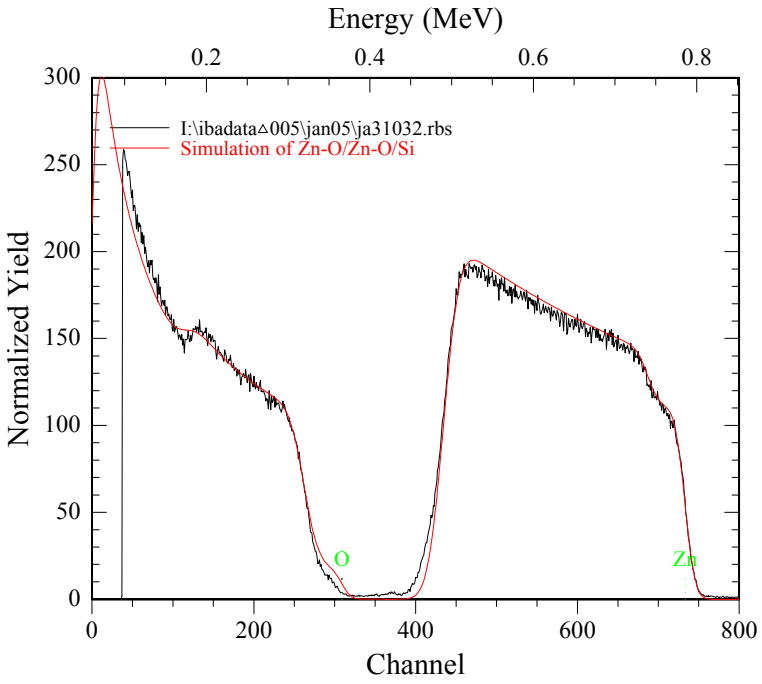

RBS File: I:\ibadata\2005\jan05\ja31242.rbs

Identifier:

LTCT Text:

Date:

Beam: 1.000 MeV 4He+ 30.00 uCoul @ 0.00 nA

Geometry: IBM Theta: 0.00 Phi: 15.00 Psi: 0.00

MCA: Econv: 0.970 80.000 First chan: 0.0 NPT: 1024

Detector: FWHM: 20.0 keV Tau: 0.0 Omega: 0.770

Correction: 1.0500

#	Thickness	Sublayers	Composition . . .
1	300.00 /CM2	auto	Zn 1.000 O 1.700
2	390.00 /CM2	auto	Zn 0.100 Si 1.000
3	1000000.00 /CM2	auto	Si 1.000

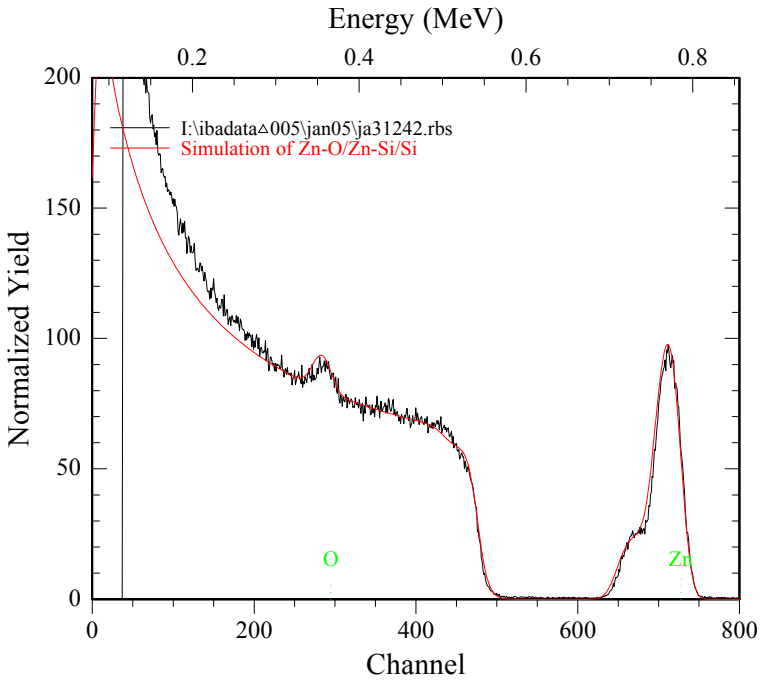

RBS results Feb 07

Date: 02/2007

Sample # DC77 (Twin layer)

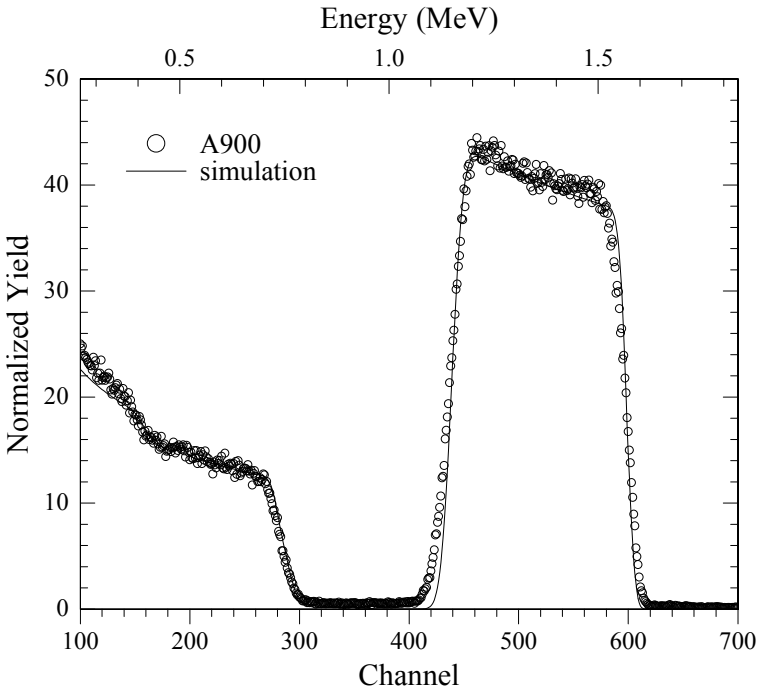

#	Thickness	Composition
1	200.00 /CM2	O 1.000 Zn 1.000 C 1.000
2	3900.00 /CM2	O 1.000 Zn 1.000
3	50000.00 /CM2	O 2.500 Si 1.000 Al 0.300 Ca 0.010

Notes:

- Film exhibits a thin surface layer that does not consist of ZnO. Light impurities must be present, such as carbon.
- The interfaces to the glass substrate are very rough suggesting diffusion
- To calculate the film thickness in nm, the material density of crystalline ZnO must be considered.

Appendix F

d_{33} results

d_{33} results using single beam interferometry (selected data shown)

sample ID	Date	Time	vpp	vinp	vo	phase	kHz	bias	d33
dc_21_rt	16/06/2005	09:34	0.56	1	109	-120	1	0	27.64
dc_21_rt	16/06/2005	09:42	0.6	1	142	-95	1	2	33.61
dc_21_rt	16/06/2005	09:50	0.58	1	118	-104	1	-2	28.89
dc_21_rt	16/06/2005	09:57	0.56	1	74	-120	1	0	18.76
dc_21_rt	16/06/2005	10:05	0.56	0.71	31	-47	1	6	11.07
dc_22_600	14/06/2005	15:52	1.2	1.05	698	-101	1	0	78.66
dc_22_600	14/06/2005	15:55	1.2	1.05	195	-89	1	2	21.98
dc_22_600	14/06/2005	15:59	1.2	1	61	-112	1	-2	7.22
dc_22_600	14/06/2005	16:02	1.2	1.025	781	-102	1	0	90.16
dc_22_600_RIE	15/06/2005	11:34	1	1	11	-89	1	6	1.56
dc_22_600_RIE	15/06/2005	11:41	1	0.34	16	175	1	-6	6.68
dc_22_600_RIE	15/06/2005	11:48	1.02	1	68	-122	1	0	9.47
dc_22_600_RIE	15/06/2005	11:52	1	2	80	-129	1	0	5.68
dc_22_700	16/06/2005	14:34	1.1	1	1	var	1	0	0.13
dc_22_700	16/06/2005	14:37	1.1	1	2	-45	1	6	0.26
dc_22_700_RIE	16/06/2005	14:49	0.8	1	19	-90	1	0	3.37
dc_22_700_RIE	16/06/2005	14:56	0.8	1	123	-100	1	2	21.83
dc_22_800	9/06/2005	12:09	1.1	1.05	14	-86	1	2	1.72
dc_22_800	9/06/2005	12:19	1.1	1.05	9.2	-104	1	0	1.13
dc_22_800	9/06/2005	12:25	1.1	0.9	241	-99	1	6	34.57
dc_22_800	9/06/2005	12:33	1.1	0.95	180	-102	1	6	24.46
dc_22_800_RIE	9/06/2005	17:21	2.5	1.05	17	-103	1	6	0.92
dc_22_800_RIE	9/06/2005	17:24	2.5	1.05	9.8	-101	1	0	0.53
dc_22_800_RIE	9/06/2005	17:28	2.5	1.05	8	-147	1	-6	0.43
dc_22_800_RIE	9/06/2005	17:36	2.5	5	46	-116	1	0	0.52
dc_22_rt	8/06/2005	11:00	0.51	1	109	-92	1	-2	30.35
dc_22_rt	8/06/2005	15:30	1.45	1.025	83	-116	1	0	7.93
dc_22_rt	8/06/2005	15:40	1.4	0.975	52	-77	1	-2	5.41
dc_22_rt	8/06/2005	15:50	1.4	0.1975	78	-160	1	-5	40.06
dc_22_rt_RIE	9/06/2005	15:31	2.8	0.95	291	-87	1	6	15.53
dc_22_rt_RIE	9/06/2005	15:36	2.8	1.05	546	-108	1	0	26.37
dc_22_rt_RIE	9/06/2005	16:25	1.3	0.85	46	-66	1	-6	5.91
dc_22_rt_RIE	9/06/2005	16:32	1.3	1.05	512	-119	1	0	53.26

d_{33} results using double beam interferometry

sample ID	Date	vpp	d33 (Pos1)	d33 (Pos2)	d33 (Pos3)	d33 (Pos4)	d33 (Pos5)
dc_25_rt	29/08/2005	0.5	3.35	3.0	3.5	3.5	4.25
dc_25_rt	29/08/2005	1.5	3.4	3.05	3.5	3.2	4.3
dc_25_rt	29/08/2005	3.0	3.25	N/A	3.5	N/A	4.3
dc_25_rt	29/08/2005	5.0	3.25	N/A	3.45	N/A	4.3

Bibliography

1. Pearton, S.J., et al., *Recent advances in processing of ZnO.* Journal of Vacuum Science & Technology B, 2004. **22**(3): p. 932-948.
2. Song, D., et al., *Investigation of lateral parameter variations of Al-doped zinc oxide films prepared on glass substrates by rf magnetron sputtering.* Solar Energy Materials and Solar Cells, 2002. **73**(1): p. 1-20.
3. Kang, H.S., et al., *Variation of light emitting properties of ZnO thin films depending on post-annealing temperature.* Materials Science and Engineering B-Solid State Materials for Advanced Technology, 2003. **102**(1-3): p. 313-316.
4. Pearton, S.J., et al., *Recent progress in processing and properties of ZnO.* Superlattices and Microstructures, 2003. **34**(1-2): p. 3-32.
5. Collings, A.A.F. and A.F. Caruso, *Biosensors: recent advances.* Reports on Progress in Physics, 1997. **60**(11): p. 1397.
6. Moustaghfir, A., et al., *Sputtered zinc oxide coatings: structural study and application to the photoprotection of the polycarbonate.* Surface & Coatings Technology, 2004. **180-181**: p. 642-645.
7. Lee, V.J. and G. Parravano, *Sintering Reactions of Zinc Oxide.* Journal of Applied Physics, 1959. **30**(11): p. 1735-1740.
8. Valeev, K.S., V.A. Knyazev, and N.O. Drozdov, *Non-linear varistors using oxides of zinc, silicon and tin.* Elektrichestvo, 1964(4): p. 72-76.
9. Fabricius, H., T. Skettrup, and P. Bisgaard, *Ultraviolet detectors in thin sputtered ZnO films.* Applied Optics, 1986. **25**(16): p. 2764-7.
10. Pearton, S.J., et al., *Recent progress in processing and properties of ZnO.* Progress in Materials Science, 2005. **50**(3): p. 293-340.
11. Martin, M., *Life and achievements of Carl Wagner, 100th birthday.* Solid State Ionics, 2002. **152-153**: p. 15-17.
12. Dulub, O., L.A. Boatner, and U. Diebold, *STM study of the geometric and electronic structure of ZnO(0 0 0 1)-Zn, (0 0 0 1 over-bar)-O, (1 0 1 over-bar 0), and (1 1 2 over-bar 0) surfaces.* Surface Science, 2002. **519**(3): p. 201-217.
13. Allen, M.W., S.M. Durbin, and J.B. Metson, *Silver oxide Schottky contacts on n-type ZnO.* Applied Physics Letters, 2007. **91**(5): p. 053512-3.
14. Allen, M.W., M.M. Alkaisi, and S.M. Durbin, *Metal Schottky diodes on Zn-polar and O-polar bulk ZnO.* Applied Physics Letters, 2006. **89**(10): p. 103520-3.
15. Ozgur, U., et al., *A comprehensive review of ZnO materials and devices.* Journal of Applied Physics, 2005. **98**(4): p. 041301-103.
16. Rössler, U., *Energy Bands of Hexagonal II-VI Semiconductors.* Physical Review, 1969. **184**(3): p. 733.
17. Vesely, C.J. and D.W. Langer, *Electronic Core Levels of the IIB-VIA Compounds.* Physical Review B, 1971. **4**(2): p. 451.
18. Powell, R.A., W.E. Spicer, and J.C. McMenamin, *Location of the Zn 3d States in ZnO.* Physical Review Letters, 1971. **27**(2): p. 97.
19. Powell, R.A., W.E. Spicer, and J.C. McMenamin, *Photoemission Studies of Wurtzite Zinc Oxide.* Physical Review B, 1972. **6**(8): p. 3056.
20. Vogel, D., P. Krüger, and J. Pollmann, *Ab initio electronic-structure calculations for II-VI semiconductors using self-interaction-corrected pseudopotentials.* Physical Review B, 1995. **52**(20): p. R14316.
21. Thangavel, R., M. Rajagopalan, and J. Kumar, *Theoretical investigations on ZnCdO2 and ZnMgO2 alloys: A first principle study.* Solid State Communications, 2006. **137**(9): p. 507-511.
22. Brown, H.E., *Zinc Oxide Rediscovered*. 1957 The New Jersey Zinc Company.
23. Neville, R.C. and C.A. Mead, *SURFACE BARRIERS ON ZINC OXIDE.* 1970. **41**(9): p. 3795-3800.
24. Mackrodt, W., et al., *The calculated defect structure of ZnO*. 1980, HAL - CCSD.

25. Gardeniers, J.G.E., Z.M. Rittersma, and G.J. Burger, *Preferred orientation and piezoelectricity in sputtered ZnO films.* Journal of Applied Physics, 1998. **83**(12): p. 7844-7854.
26. Meyer, B.K., et al., *Bound exciton and donor-acceptor pair recombinations in ZnO.* Physica Status Solidi B-Basic Research, 2004. **241**(2): p. 231-260.
27. Klingshirn, C., et al., *ZnO rediscovered -- once again!?* Superlattices and Microstructures, 2005. **38**(4-6): p. 209-222.
28. Jagadish, C. and S. Pearton, *Zinc Oxide Bulk, thin Films and Nanostructures*. 2006.
29. Chapman, B.N., *Glow discharge processes : sputtering and plasma etching*. 1980, New York: Wiley.
30. Ohring, M., *Materials science of thin films deposition and structure*. 2001, San Diego, CA: Academic Press.
31. Smith, D.L., *Thin-film deposition : principles and practice*. 1995, New York: McGraw-Hill.
32. Singh, R., M. Kumar, and S. Chandra, *Growth and characterization of high resistivity c-axis oriented ZnO films on different substrates by RF magnetron sputtering for MEMS applications.* Journal of Materials Science, 2007. **42**(12): p. 4675-4683.
33. Anderson, A.C. and D.E. Oates. *RF magnetron sputtering of ZnO for SAW: effects of magnetic field strength and configuration*. 1982. San Diego, CA, USA: IEEE.
34. Kappertz, O., et al., *Reactive sputter deposition of zinc oxide: Employing resputtering effects to tailor film properties.* Thin Solid Films, 2005. **484**(1-2): p. 64-67.
35. Swann, S., *Magnetron sputtering.* Physics in Technology, 1988. **19**(2): p. 67.
36. Perry, F., A. Billard, and C. Frantz, *Optical emission spectroscopy study of a reactive magnetron sputtering Ar-O₂ discharge modulated at low frequency.* Surface & Coatings Technology, 1997. **94-95**(1-3): p. 681-685.
37. Ahn, H., et al., *BCN coatings at low temperature using PACVD: capacitive vs. inductive plasma coupling.* Surface and Coatings Technology, 2003. **169-170**: p. 251-253.
38. Goodberlet, J.G., J.T. Hastings, and H.I. Smith. *Performance of the Raith 150 electron-beam lithography system*. in *The 45th international conference on electron, ion, and photon beam technology and nanofabrication*. 2001. Washington, DC (USA): AVS.
39. Digital Instruments, *Scanning probe microscopy training notebook.*
40. Alexe, M. and A. Gruverman, *Nanoscale Characterisation of Ferroelectric Materials*. NanoScience and Technology, ed. P.e.a. Avouris. 2004: Springer-Verlag.
41. Gruverman, A. and S.V. Kalinin, *Piezoresponse force microscopy and recent advances in nanoscale studies of ferroelectrics.* Journal of Materials Science, 2006. **41**(1): p. 107-116.
42. Kalinin, S.V., A. Rar, and S. Jesse, *A decade of piezoresponse force microscopy: Progress, challenges, and opportunities.* IEEE Transactions on Ultrasonics, Ferroelectrics, and Frequency Control, 2006. **53**(12): p. 2226-2251.
43. Nagarajan, V., et al., *Nanoscale phenomena in ferroelectric thin films.* Integrated Ferroelectrics, 2002. **42**: p. 173-189.
44. Zhao, M.H., Z.L. Wang, and S.X. Mao, *Piezoelectric Characterization of Individual Zinc Oxide Nanobelt Probed by Piezoresponse Force Microscope.* Nano Lett., 2004. **4**(4): p. 587-590.
45. Calarco, R., et al., *Piezoresponse force microscopy for imaging of GaN surfaces.* Physica Status Solidi (A) Applied Research, 2005. **202**(5): p. 785-789.
46. Rodriguez, B.J., et al., *Piezoresponse force microscopy for polarity imaging of GaN.* Applied Physics Letters, 2002. **80**(22): p. 4166-8.
47. Schuler, L., et al., *The Effect of Substrate Material and Postannealing on the Photoluminescence and Piezo Properties of DC-Sputtered ZnO.* Journal of Electronic Materials, 2007. **36**(4): p. 507-518.
48. Ke-ming, Z., et al., *Piezoelectricity of ZnO Films Prepared by Sol-Gel Method.* Chinese Journal of Chemical Physics, 2007(6): p. 721.
49. Scrymgeour, D.A., et al., *Polarity and piezoelectric response of solution grown zinc oxide nanocrystals on silver.* Journal of Applied Physics, 2007. **101**(1): p. N.PAG.

50. Varatharajan, A., *Nanoscale domain wall dynamics in ferroelectric thin films*, in *School of Materials Science & Engineering*. 2006, The University of New South Wales: Sydney.
51. Muensit, S., D. Wilson, and I.L. Guy. *Study of piezoelectric effect in GaN thin films using a modified Michelson interferometer*. in *Proceedings of the 1996 Conference on Optoelectronic & Microelectronic Materials and Devices, COMMAD, Dec 8-11 1996*. 1996. Canberra, Aust: IEEE, Piscataway, NJ, USA.
52. Kholkin, A.L., et al., *Interferometric measurements of electric field-induced displacements in piezoelectric thin films.* Review of Scientific Instruments, 1996. **67**(5): p. 1935.
53. Polla, D.L. and L.F. Francis, *Processing and characterization of piezoelectric materials and integration into microelectromechanical systems*. 1998, Annual Reviews Inc, Palo Alto, CA, USA. p. 563-597.
54. Look, D.C., et al., *Electrical properties of bulk ZnO.* Solid State Communications, 1998. **105**(6): p. 399-401.
55. Nause, J. and B. Nemeth, *Pressurized melt growth of ZnO boules.* Semiconductor Science and Technology, 2005. **20**(4): p. S45.
56. Katsumi, M., et al., *Growth of 2 inch ZnO bulk single crystal by the hydrothermal method.* Semiconductor Science and Technology, 2005. **20**(4): p. S49.
57. Kaidashev, E.M., et al., *High electron mobility of epitaxial ZnO thin films on c-plane sapphire grown by multistep pulsed-laser deposition.* Applied Physics Letters, 2003. **82**(22): p. 3901-3903.
58. Kato, H., et al., *Effect of O/Zn flux ratio on crystalline quality of ZnO films grown by plasma-assisted molecular beam epitaxy.* Japanese Journal of Applied Physics, Part 1: Regular Papers and Short Notes and Review Papers, 2003. **42**(4 B): p. 2241-2244.
59. Iwata, K., et al., *Improvement of electrical properties in ZnO thin films grown by radical source(RS)-MBE.* Physica Status Solidi (A) Applied Research, 2000. **180**(1): p. 287-292.
60. Kim, Y.J. and H.J. Kim, *Effect of substrate temperature and rf power on the growth rate and the orientation of ZnO thin films prepared by plasma enhanced chemical vapor deposition.* Materials Letters, 1994. **21**(3-4): p. 351-356.
61. Minami, T., S. Ida, and T. Miyata, *High rate deposition of transparent conducting oxide thin films by vacuum arc plasma evaporation.* Thin Solid Films, 2002. **416**(1-2): p. 92-96.
62. Park, W.I. and G.C. Yi, *Photoluminescent properties of ZnO thin films grown on SiO2/Si(100) by metal-organic chemical vapor deposition.* Journal of Electronic Materials, 2001. **30**(10): p. L32-L35.
63. Shukla, P., et al. *Polymer Assisted Deposition (PAD) of thin metal films: A new technique to the preparation of metal oxides and reduced metal films*. 2006. Boston, MA, United States: Materials Research Society, Warrendale, PA 15086, United States.
64. Lin, Y., et al., *Green luminescent zinc oxide films prepared by polymer-assisted deposition with rapid thermal process.* Thin Solid Films, 2005. **492**(1-2): p. 101-104.
65. Gao, W., et al., *Zinc oxide films formed by oxidation of zinc under low partial pressure of oxygen.* Materials Letters, 2003. **57**(8): p. 1435-1440.
66. Li, Z.W. and W. Gao, *Growth of zinc oxide thin films and nanostructures by wet oxidation.* Thin Solid Films, 2007. **515**(7-8): p. 3323-3329.
67. Bin Lee, J., S.H. Kwak, and H.J. Kim, *Effects of surface roughness of substrates on the c-axis preferred orientation of ZnO films deposited by r.f. magnetron sputtering.* Thin Solid Films, 2003. **423**(2): p. 262-266.
68. Chu, S.Y., T.Y. Chen, and W. Water, *The investigation of preferred orientation growth of ZnO films on the PbTiO3-based ceramics and its application for SAW devices.* Journal of Crystal Growth, 2003. **257**(3-4): p. 280-285.
69. Gruber, D., F. Kraus, and J. Muller, *A novel gas sensor design based on CH4/H-2/H2O plasma etched ZnO thin films.* Sensors and Actuators B-Chemical, 2003. **92**(1-2): p. 81-89.
70. Gupta, V. and A. Mansingh. *Effect of post deposition annealing on sputtered zinc oxide film*. 1994. University Park, PA, USA: IEEE, Piscataway, NJ, USA.
71. Holland, A.S., G.K. Reeves, and P.W. Leech. *Effects of non-planar surfaces on the growth of RF magnetron sputtered ZnO*. 2001. San Francisco, CA: Materials Research Society.

72. Jung, M., et al., *Investigation of the annealing effects on the structural and optical properties of sputtered ZnO thin films.* Journal of Crystal Growth, 2005. **283**(3-4): p. 384-389.
73. Kang, D.J., et al., *Structural and electrical characteristics of R.F. magnetron sputtered ZnO films.* Thin Solid Films, 2005. **475**(1-2 SPEC ISS): p. 160-165.
74. Kappertz, O., R. Drese, and M. Wuttig, *Correlation between structure, stress and deposition parameters in direct current sputtered zinc oxide films.* Journal of Vacuum Science and Technology A: Vacuum, Surfaces and Films, 2002. **20**(6): p. 2084-2095.
75. Kumar, S., V. Gupta, and K. Sreenivas, *Synthesis of photoconducting ZnO nano-needles using an unbalanced magnetron sputtered ZnO/Zn/ZnO multilayer structure.* Nanotechnology, 2005. **16**(8): p. 1167-1171.
76. Lad, R.J., P.D. Funkenbusch, and C.R. Aita, *Postdeposition Annealing Behaviour of RF Sputtered ZnO Films.* 1980. **17**(4): p. 808-811.
77. Mitsuyu, T., S. Ono, and K. Wasa, *STRUCTURES AND SAW PROPERTIES OF rf-SPUTTERED SINGLE-CRYSTAL FILMS OF ZnO ON SAPPHIRE.* 1980. **51**(5): p. 2464-2470.
78. Ruthe, K.C., D.J. Cohen, and S.A. Barnett, *Low temperature epitaxy of reactively sputtered ZnO on sapphire.* Journal of Vacuum Science and Technology A: Vacuum, Surfaces and Films, 2004. **22**(6): p. 2446-2452.
79. Schuler, L.P., et al., *Comparison of DC and RF sputtered zinc oxide films with post-annealing and dry etching and effect on crystal composition.* Japanese Journal of Applied Physics, Part 1: Regular Papers and Short Notes and Review Papers, 2005. **44**(10): p. 7555-7560.
80. Wacogne, B., M.P. Roe, and C.N. Pannell, *Deposition, evaluation and application of sputtered zinc oxide thin films.* International Journal of Optoelectronics, 1995. **10**(1): p. 9-18.
81. Water, W. and S.-Y. Chu, *Physical and structural properties of ZnO sputtered films.* Materials Letters, 2002. **55**(1-2): p. 67-72.
82. Schuler, L.P., *Wireless Identification and Sensing using Surface Acoustic Wave Devices*, in *ECE*. 2003, University of Canterbury: Christchurch, New Zealand.
83. Hickernell, F.S. *Measurement techniques for evaluating piezoelectric thin films*. in *Proceedings of the 1996 IEEE Ultrasonics Symposium. Part 1 (of 2), Nov 3-6 1996*. 1996. San Antonio, TX, USA: IEEE, Piscataway, NJ, USA.
84. Chen, J.J., et al., *Effect of sputtering oxygen partial pressures on structure and physical properties of high resistivity ZnO films.* Applied Surface Science, 2004. **223**(4): p. 318-329.
85. Miller, P., et al. *Effect of substrate and annealing temperature on the optical and physical properties of DC sputtered ZnO films [Poster]*. in *The 4th International Workshop on ZnO and Related Materials*. 2006. Giessen, Germany.
86. Thornton, J.A., *The microstructure of sputter-deposited coatings.* J. Vac. Sci. & Technol., 1986. **A 4 (6)**(Nov/Dec 1986): p. 3059-3065.
87. Vellekoop, M.J., et al., *Compatibility of zinc oxide with silicon IC processing.* Sensors and Actuators, A: Physical Transducers '89: Proceedings of the 5th International Conference on Solid-State Sensors and Actuators and Eurosensors III. Part 4, Jun 25-30 1989, 1990. **23**(1-3): p. 1027-1030.
88. Kapustianyk, V., et al., *Influence of size effect and sputtering conditions on the crystallinity and optical properties of ZnO thin films.* Optics Communications, 2007. **269**(2): p. 346-350.
89. Depla, D. and R. De Gryse, *Target poisoning during reactive magnetron sputtering: Part III: the prediction of the critical reactive gas mole fraction.* Surface and Coatings Technology, 2004. **183**(2-3): p. 196-203.
90. Combadiere, L. and J. Machet, *Study and control of both target-poisoning mechanisms and reactive phenomenon in reactive planar magnetron cathodic sputtering of TiN.* Surface & Coatings Technology, 1996. **82**(1-2): p. 145-157.

91. Carter, D.C., W.D. Sproul, and D.J. Christie. *Effective Closed-Loop Control for Reactive Sputtering Using Two Reactive Gases*. 2004.
92. Lee, J., et al., *Structural, electrical and transparent properties of ZnO thin films prepared by magnetron sputtering.* Current Applied Physics, 2004. **4**(2-4): p. 398-401.
93. Lee, J.H., B.W. Yeo, and B.O. Park, *Effects of the annealing treatment on electrical and optical properties of ZnO transparent conduction films by ultrasonic spraying pyrolysis.* Thin Solid Films, 2004. **457**(2): p. 333-337.
94. Nunes, P., E. Fortunato, and R. Martins, *Influence of the post-treatment on the properties of ZnO thin films.* Thin Solid Films, 2001. **383**(1-2): p. 277-280.
95. Zhi, Z.Z., et al., *Effects of thermal annealing on ZnO films grown by plasma enhanced chemical vapour deposition from $Zn(C_2H_5)_2$ and CO_2 gas mixtures.* Journal of Physics D: Applied Physics, 2003. **36**(6): p. 719-722.
96. Kang, H.S., et al., *Annealing effect on the property of ultraviolet and green emissions of ZnO thin films.* Journal of Applied Physics, 2004. **95**(3): p. 1246-1250.
97. Al Asmar, R., et al., *Effect of annealing on the electrical and optical properties of electron beam evaporated ZnO thin films.* Thin Solid Films, 2005. **473**(1): p. 49-53.
98. Lee, J., et al., *Microstructure and properties of annealed ZnO thin films deposited by magnetron sputtering.* Acta Metallurgica Sinica (English Letters), 2005. **18**(3): p. 177-183.
99. Zhang, Y., et al., *Effect of annealing on ZnO thin films grown on (001) silicon substrate by low-pressure metalorganic chemical vapour deposition.* Semiconductor Science and Technology, 2004. **19**(6): p. 755-758.
100. Lad, R.J., P.D. Funkenbusch, and C.R. Aita, *Postdeposition annealing behavior of RF sputtered ZnO films.* Journal of Vacuum Science and Technology, 1980. **17**(4): p. 808-11.
101. Craciun, V., et al., *Oxygen trapping during pulsed laser deposition of oxide films.* Applied Surface Science, 2003. **208-209**: p. 507-511.
102. Hong Seong Kang, J.S.K.J.W.K.S.Y.L., *Investigation on visible emission control of ZnO thin film.* physica status solidi (c), 2004. **1**(10): p. 2550-2553.
103. Ellmer, K., *Magnetron sputtering of transparent conductive zinc oxide: Relation between the sputtering parameters and the electronic properties.* Journal of Physics D: Applied Physics, 2000. **33**(4): p. 17-32.
104. Van de Krol, R. and H.L. Tuller, *Electroceramics - The role of interfaces.* Solid State Ionics, 2002. **150**(1-2): p. 167-179.
105. Wang, Z.G., et al., *Blue luminescence from carbon modified ZnO nanoparticles.* Journal of Materials Science, 2006. **41**(12): p. 3729-3733.
106. Mendelsberg, R.J., et al., *Carbon enhanced blue-violet luminescence in ZnO films grown by pulsed laser deposition.* Current Applied Physics, 2008. **8**(3-4): p. 283-286.
107. Xu, X., et al., *Formation mechanism of Zn_2SiO_4 crystal and amorphous SiO_2 in ZnO/Si system.* Journal of Physics Condensed Matter, 2003. **15**(40): p. 607-613.
108. Schuler, L.P., et al. *Investigation of piezoelectric domain structures using PFM on DC sputtered ZnO films*. in *AMN-3 Third international conference on advance materials and nanotechnology*. 2007. Wellington, New Zealand.
109. Alexander, T.P., et al. *Dielectric properties of sol-gel derived ZnO thin films*. in *Proceedings of the 1996 10th IEEE International Symposium on Applications of Ferroelectrics, ISAF'96. Part 2 (of 2), Aug 18-21 1996*. 1996. East Brunswick, NJ, USA: IEEE, Piscataway, NJ, USA.
110. Guy, I., *Personal communication*. 2005.
111. Kholkin, A.L., et al. *Piezoelectric characterization of Pb(Zr, Ti)O_3 thin films by interferometric technique*. in *Proceedings of the 1996 10th IEEE International Symposium on Applications of Ferroelectrics, ISAF. Part 1 (of 2), Aug 18-21 1996*. 1996. East Brunswick, NJ, USA: IEEE, Piscataway, NJ, USA.
112. Zuniga-Perez, J., et al., *Facets evolution and surface electrical properties of nonpolar m-plane ZnO thin films.* Applied Physics Letters, 2006. **88**(26): p. 261912.
113. Zuniga-Perez, J., et al., *Polarity effects on ZnO films grown along the nonpolar [112 over-bar 0] direction.* Physical Review Letters, 2005. **95**(22): p. 226105.

114. Ni, H.Q., et al., *Investigation of Li-doped ferroelectric and piezoelectric ZnO films by electric force microscopy and Raman spectroscopy.* Applied Physics Letters, 2001. **79**(6): p. 812-14.
115. Gruverman, A., O. Auciello, and H. Tokumoto, *Imaging and control of domain structures in ferroelectric thin films via scanning force microscopy*. 1998, Annual Reviews Inc, Palo Alto, CA, USA. p. 101-123.
116. Jagadish, C., *Personal communication*.
117. Ding, Y., X.Y. Kong, and Z.L. Wang, *Doping and planar defects in the formation of single-crystal ZnO nanorings.* Physical Review B (Condensed Matter and Materials Physics), 2004. **70**(23): p. 235408-7.
118. Liu, M. and H.K. Kim, *Ultraviolet detection with ultrathin ZnO epitaxial films treated with oxygen plasma.* Applied Physics Letters, 2004. **84**(2): p. 173-175.
119. Liang, S., et al. *ZnO Schottky ultraviolet photodetectors*. 2001: Elsevier Science B.V.
120. Koike, K., et al. *Molecular beam epitaxial growth of wide bandgap ZnMgO alloy films on (1 1 1)-oriented Si substrate toward UV-detector applications*. 2005: Elsevier, Amsterdam, 1000 AE, Netherlands.
121. Endo, H., et al., *Fabrication and characterization of a Schottky barrier diode-type ultraviolet sensor using a ZnO single crystal.* IEEJ Transactions on Sensors and Micromachines, 2007. **127**(3): p. 131-135.
122. White, R.M. and F.W. Voltmer, *Direct Piezoelectric Coupling to Surface Elastic Waves.* Appl. Phys. Lett., 7, pp. 314-316, 1965.
123. Yamanouchi, K. *GHz-range saw device using nano-meter electrode fabrication technology*. in *Proceedings of the 1994 IEEE Ultrasonics Symposium. Part 1 (of 3), Nov 1-4 1994*. 1994. Cannes, Fr: IEEE, Piscataway, NJ, USA.
124. Yamanouchi, K., et al., *10 GHz surface acoustic wave filters with narrow-gap interdigital transducer structure.* Japanese Journal of Applied Physics, Part 1: Regular Papers & Short Notes & Review Papers. Proceedings of the 1995 16th Symposium on Ultrasonic Electronics, USE95, Nov 27-29 1995, 1996. **35**(5B): p. 2994-2996.
125. Hachigo, A., et al. *10GHz narrow band SAW filters using diamond*. in *1999 IEEE Ultrasonics Symposium, Oct 17-Oct 20 1999*. 1999. Caesars Tahoe, NV, USA: Institute of Electrical and Electronics Engineers Inc., Piscataway, NJ, USA.
126. Yamazaki, O., K. Wasa, and S. Hayakawa. *Highly reliable ZnO thin film SAW Nyquist filters for TV*. 1980. Boston, MA, USA: IEEE.
127. Quartzunlimited.com. *Properties of Quartz & Silica (Optical)*. [web site] 2007 [cited; Optical properties of natural quartz and synthetic fused silica]. Available from: http://www.quartzunlimited.com/Pages/Properties/optical.html.
128. Polla, D.L., et al. *Integration of surface-micromachined zinc oxide sensors in n-well CMOS technology*. in *Electron Devices Meeting, 1989. IEDM '89. Technical Digest., International*. 1989.
129. Tigli, O. and M.E. Zaghloul, *A novel saw device in CMOS: design, modeling, and fabrication.* IEEE Sensors Journal, 2007. **7**(2): p. 219-27.
130. Choi, K.H., et al. *Effect of dielectric layer in ZnO/dielectric/Si layered structure on GSAW and HVPSAW propagation properties*. in *2000 IEEE Ultasonics Symposium, Oct 22-25 2000*. 2000. San Juan: Institute of Electrical and Electronics Engineers Inc.
131. Didenko, I.S., F.S. Hickernell, and N.F. Naumenko, *Experimental and theoretical characterization of the SAW propagation properties for zinc oxide films on silicon carbide.* IEEE Transactions on Ultrasonics, Ferroelectrics, and Frequency Control, 2000. **47**(1): p. 179-187.